

STATUS OF THESIS

Title of thesis Pore-scale Investigation of Wettability and Spreading Coefficient Effects in Low Salinity Waterflood-WAG EOR

I MUSFIKA RAHMAN

hereby allow my thesis to be placed at the Information Resource Center (IRC) of Universiti Teknologi PETRONAS (UTP) with the following conditions:

1. The thesis becomes the property of UTP
2. The IRC of UTP may make copies of the thesis for academic purposes only.
3. This thesis is classified as

<input type="checkbox"/>	Confidential
<input checked="" type="checkbox"/>	Non-confidential

If this thesis is confidential, please state the reason:

The contents of the thesis will remain confidential for _____ years.

Remarks on disclosure:

Musfika Rahman

Signature of Author

Permanent address: 4-5, Batali road,
Ideal Niloy Tower, Flat-A8, Enayet
Bazar, Chittagong, 4000, Bangladesh

Date : 11/08/2022

Endorsed by



Signature of Supervisor

Name of Supervisor
Dr. Iskandar B Dzulkarnain

Date : 18/08/2022

UNIVERSITI TEKNOLOGI PETRONAS

PORE-SCALE INVESTIGATION OF WETTABILITY AND SPREADING COEFFICIENT
EFFECTS IN LOW SALINITY WATERFLOOD-WAG EOR

by

MUSFIKA RAHMAN

The undersigned certify that they have read and recommended to the Postgraduate Studies Programme for acceptance of this thesis for the fulfillment of the requirements for the degree stated.

Signature:

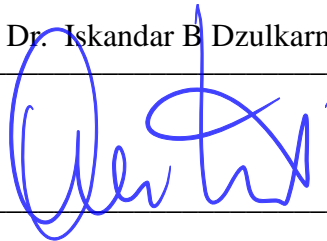


18/08/2022

Main Supervisor:

Dr. Iskandar B Dzulkarnain

Signature:



20/08/2022

Co-Supervisor:

Dr. Berihun Mamo Negash

Signature:



23/08/2022

Assoc Prof Dr Khaled Abdalla Elraies
Chair
Petroleum Engineering Department

Head of Department:

Assoc. Prof. Dr. Khaled Abdalla Elraies

PORE-SCALE INVESTIGATION OF WETTABILITY AND SPREADING
COEFFICIENT EFFECTS IN LOW SALINITY WATERFLOOD-WAG EOR

by

MUSFIKA RAHMAN

A Thesis

Submitted to the Postgraduate Studies Programme

as a Requirement for the Degree of

MASTER OF SCIENCE

DEPARTMENT OF PETROLEUM ENGINEERING

UNIVERSITI TEKNOLOGI PETRONAS

BANDAR SERI ISKANDAR,

PERAK

AUGUST 2022

DECLARATION OF THESIS

Title of thesis

Pore-scale Investigation of Wettability and Spreading Coefficient Effects
in Low Salinity Waterflood-WAG EOR

MUSFIKA RAHMAN

I _____

hereby declare that the thesis is based on my original work except for quotations and citations which have been duly acknowledged. I also declare that it has not been previously or concurrently submitted for any other degree at UTP or other institutions.

Witnessed by

Musfika Rahman



Signature of Author

Signature of Supervisor

Permanent address: 4-5, Batali Road,
Ideal Niloy Tower, Flat-A8, Enayet Bazar,
Chittagong, 4000, Bangladesh

Name of Supervisor
Dr. Iskandar B Dzulkarnain

Date : 11/08/2022

Date : 18/08/2022

DEDICATION

To my beloved parents Md Mostafizur Rahman and Roshan Ara and my most supportive husband Muhammed Rashik Mojid.

ACKNOWLEDGEMENTS

I would like to say ALHAMDULILLAH for all those blessings I have been bestowed upon. The Almighty ALLAH has been very kind throughout my M.Sc. journey.

I would like to express my profound gratitude to my supervisor Dr. Iskandar B Dzulkarnain for his tremendous support, noteworthy guidance, and valuable suggestions for the accomplishment of my research. I am indebted to Universiti Teknologi PETRONAS (UTP) for providing me with financial support through Graduate Assistantship (GA) and research facilities to continue the research journey smoothly. I like to thank the Centralized Analytical Laboratory (CAL) for assisting me in the characterization experiments of my research.

I am also grateful to my co-supervisor Dr. Berihun Mamo Negash who spent a significant amount of time guiding my work. I am eternally thankful to my friend Amni Haslinda Alpandi, Research officer Nurul Nadia Izwani Reepei, Lead technologist Mior Rosgiazhar B Mior Sofli for their constant encouragement and support over the last two years. I would also like to felicitate my parents, husband, teachers, and friends for their inspiration and support.

ABSTRACT

Low-salinity water (LSW) flooding is an emerging EOR technique due to its oil recovery performance and lower environmental impact compared to the conventional EOR approach. LSW combined with water alternating CO₂ gas (WAG) is a recent addition to the EOR process which has not yet been properly explored. From the recent literature, the effect of wettability and spreading coefficient (SC), in a three-phase flow system such as the combination of LSW flood with CO₂ WAG requires further investigation as it play important role in the recovery of residual oil by controlling the fluids distribution and mobilization at the pore scale. The main aim of the study is to investigate the effect of wettability and SC on the low salinity water alternating CO₂ (LSWACO₂) process on a pore scale. In this study, Dulang, Decane, and Decane+Dulang mixture has been used as the oil phase whereas seven different salinity brine and CO₂ have been used as the water phase and gas phase. Reservoir temperature (96°C) and pressure (200 - 2000 psi) have been maintained in the interfacial tension and contact angle experiments. For the wettability study, the contact angle of Berea sandstone has been measured under different wettability conditions (water-wet, oil-wet), whereas for the SC study, IFT700 has been used to measure the interfacial tension of oil-water, gas-oil, and gas-water, all using different salinity brine with and without CO₂ gas. Furthermore, for pore-scale visualization of the interactions of wettability and SC, glass micromodel experiments have been conducted in different wettability conditions. A significant outcome has been observed from interfacial tension and contact angle experiments which indicate the presence of CO₂ gas has shifted the SC from negative to positive values and wettability alteration more like wetting to the system. From the micromodel experiments, it has been found that regardless of the value of the SC and wettability conditions of the rock, LSW resulted in more recovery compared to moderately high salinity water (HSW) and high salinity sea water

(HSSW). Moreover, with a positive SC and water-wet condition, the recovery is 8% more than the negative SC and oil-wet condition. During the pore-scale investigation of LSW, the wettability condition and brine salinity influenced the oil bank formation regardless of the value of the SC. The results of this study have significant implications for the understanding of pore level interactions during LSWACO₂ flooding.

ABSTRAK

Banjiran air dengan kemasinan rendah (LSW) ialah teknik EOR yang baru muncul kerana prestasi perolehan minyaknya dan kesan yang lebih rendah terhadap alam sekitar berbanding pendekatan EOR konvensional. LSW digabungkan dengan gas CO₂ berselang-seli air (WAG) merupakan tambahan terbaru kepada proses EOR yang masih belum dikaji. Daripada kajian literatur terkini, kesan kebolehasahan dan pekali perebakan (SC), dalam sistem aliran tiga fasa seperti gabungan banjiran LSW dengan CO₂ WAG memerlukan penyiasatan lanjut kerana ia memainkan peranan penting dalam perolehan minyak sisa dengan mengawal pengedaran dan mobilisasi bendalir pada skala pori. Matlamat utama kajian ini adalah untuk menyiasat kesan kebolehasahan dan SC terhadap proses air dengan kemasinan rendah berselang-seli gas CO₂ (LSWACO₂) pada skala pori. Dalam kajian ini, minyak daripada medan minyak Dulang, Decane, dan campuran Decane+Dulang telah digunakan manakala tujuh air garam dengan kemasinan dan CO₂ yang berbeza telah digunakan sebagai fasa cecair dan fasa gas. Suhu reservoir (96°C) dan tekanan (200 - 2000 psi) telah digunakan dalam eksperimen tegangan antara muka dan eksperimen sudut sentuh. Untuk kajian kebolehasahan, sudut sentuh batu pasir Berea telah diukur di bawah keadaan kebolehasahan yang berbeza (basah air, basah minyak), manakala untuk kajian SC, IFT700 telah digunakan untuk mengukur tegangan antara muka untuk kombinasi air-minyak, gas-minyak, dan gas-air. Pengukuran ini semuanya menggunakan air garam dengan kemasinan yang berbeza dengan dan tanpa kehadiran gas CO₂. Tambahan pula, visualisasi skala pori untuk mengkaji interaksi kebolehasahan dan SC, telah dijalankan dengan menggunakan eksperimen mikromodel kaca dalam keadaan kebolehasahan yang berbeza. Hasil yang ketara telah diperhatikan daripada tegangan antara muka dan eksperimen sudut sentuh yang menunjukkan kehadiran gas CO₂ telah mengubah SC daripada nilai negatif kepada positif dan perubahan kebolehasahan ke arah basah air.

Daripada eksperimen mikromodel, didapati bahawa tanpa mengira nilai SC dan keadaan kebolehasan batuan, LSW menghasilkan lebih banyak perolehan minyak berbanding air dengan kemasinan tinggi (HSW) dan air laut dengan kemasinan tinggi (HSSW). Selain itu, dengan keadaan SC positif dan basah air, pemulihan adalah 8% lebih tinggi daripada keadaan SC negatif dan basah minyak. Semasa penyiasatan skala pori LSW, keadaan kebolehasan dan kemasinan air garam mempengaruhi pembentukan tebing minyak tanpa mengira nilai SC. Hasil kajian ini mempunyai implikasi yang signifikan terhadap pemahaman interaksi skala pori semasa banjir LSWACO₂.

In compliance with the terms of the Copyright Act 1987 and the IP Policy of the university, the copyright of this thesis has been reassigned by the author to the legal entity of the university,

Institute of Technology PETRONAS Sdn Bhd.

Due acknowledgment shall always be made of the use of any material contained in, or derived from, this thesis.

© Musfika Rahman, 2022

Institute of Technology PETRONAS Sdn Bhd

All rights reserved.

TABLE OF CONTENT

ABSTRACT	vii
ABSTRAK	ix
LIST OF FIGURES	xvii
LIST OF TABLES	xxi
NOMENCLATURE	xxiii
CHAPTER 1 INTRODUCTION	1
1.1 Background.....	1
1.2 Problem Statement.....	3
1.3 Research Objectives.....	4
1.4 Scope of the Study	4
1.5 Research Significance.....	5
1.6 Outline of the Thesis.....	6
CHAPTER 2 LITERATURE REVIEW	7
2.1 Introduction.....	7
2.2 Low Salinity Water Flooding	7
2.3 Pore Scale Experiments in Low Salinity Water Flooding	8
2.4 Water Alternating Gas	10
2.4.1 Miscible displacement.....	12

2.4.2 Immiscible displacement	12
2.4.3 CO ₂ Gas as EOR Solvent	14
2.4.4 Carbon Dioxide WAG Flooding	15
2.5 Low Salinity Water Alternating Carbon Dioxide Gas.....	16
2.6 Fluid-Rock and Fluid-Fluid Mechanisms in Three-Phase Flow- EOR	19
2.7 Application of Micromodel for Pore-Scale Study	22
2.7.1 Micromodel Geometry	22
2.7.2 Micromodel Materials	25
2.7.3 Micromodel Visualization Methods	28
2.7.4 Recent micromodel application.....	31
2.7.4.1 Phase Saturation Calculation	31
2.7.4.2 Relative Permeability.....	33
2.7.4.3 Fluid-Solid Interaction	34
2.7.4.4 Enhanced Oil Recovery	35
2.8 Summary.....	38
CHAPTER 3 RESEARCH METHODOLOGY	39
3.1 Introduction.....	39
3.2 Samples and Reagents	42
3.2.1 Crude sample.....	42

3.2.2 Brine sample preparation	43
3.2.3 Core sample preparation.....	44
3.3 Micromodel Design and Wetting Properties Alteration	46
3.4 Interfacial Tension Measurement	48
3.5 Spreading Coefficient Measurement	49
3.6 Contact Angle Measurement	50
3.7 Experimental Design and ANOVA Analysis	51
3.8 HPHT Micromodel for Pore Scale Visualization	53
3.9 Recovery Calculation.....	55
3.10 Summary.....	58
CHAPTER 4 RESULTS AND DISCUSSIONS.....	59
4.1 Introduction.....	59
4.2 Interfacial Tension Measurement	59
4.2.1 Total Samples to Measure IFT	59
4.2.2 RSM Model for Brine/Dulang IFT with CO ₂	60
4.2.3 Model Analysis	62
4.2.4 RSM Model for Brine/Dulang IFT without CO ₂	67
4.2.5 Model Analysis	68
4.2.6 Optimization Using RSM.....	72

4.2.7 Brine/Decane IFT with and without CO ₂	73
4.2.8 Brine/ Dulang+Decane IFT with and without CO ₂	78
4.2.9 Discussions from Interfacial Tension Measurement	83
4.3 Spreading Coefficient Measurement	84
4.3.1 Spreading Coefficient of Dulang with CO ₂	84
4.3.2 Spreading Coefficient of Dulang Without CO ₂	87
4.3.3 Spreading Coefficient of Decane with and without CO ₂	90
4.3.4 Spreading Coefficient of Dulang+Decane with and without CO ₂	92
4.3.5 Discussion from Spreading Coefficient Measurement.....	93
4.4 Contact Angle Measurement	94
4.4.1 RSM Model for Contact Angle of Dulang with CO ₂ and without CO ₂ (Water Wet)	94
4.4.2 Visual observation of Contact angle	104
4.4.3 Contact Angle vs Concentration at Reservoir Condition (Water Wet)	110
4.4.4 Contact angle vs Concentration at Reservoir Condition (Oil Wet)...	111
4.4.5 Discussion from Contact Angle Measurement.....	113
4.5 HPHT micromodel for pore-scale visualization of LSWACO ₂	114
4.5.1 Enhanced Oil Recovery for Decane Water Wet Condition.....	114
4.5.2 Enhanced Oil Recovery for Decane Oil-Wet Condition.....	116

4.5.3 Enhanced Oil Recovery for Decane+Dulang Water Wet Condition.	120
4.5.4 Enhanced oil Recovery for Decane+Dulang Oil Wet Condition	122
4.5.5 Discussion from Enhanced Oil Recovery Calculation	124
4.5.5.1 Effect of wettability	127
4.5.5.2 Effect of Spreading Coefficient	129
4.6 Fluid Mobilization and Distribution in Pore-scale	131
4.6.1 Fluid Mobility and Distribution Analysis for water-wet condition...	131
4.6.2 Fluid Mobility and Distribution analysis for Oil-wet condition	133
4.6.3 Active Displacement Mechanism During Three-Phase Flooding.....	135
4.7 Summary.....	138
CHAPTER 5 CONCLUSIONS AND RECOMMENDATION	139
5.1 Conclusion	139
5.2 Recommendations.....	140

LIST OF FIGURES

Figure 2.1: Advantages of CO ₂ gas as EOR solvent.....	14
Figure 3.1: Overall flowchart of experimental methodology	41
Figure 3.2: Cleaned core placed in the oven to be dried.....	45
Figure 3.3: General steps to design a micromodel.....	46
Figure 3.4: Final design with size specification.....	46
Figure 3.5: Zoom view of micromodel pore size and distance between pores.....	47
Figure 3.6: Experimental sequence for pore-scale investigation and evaluation...54	
Figure 3.7: Scale setting (oil- red color, brine- blue color)	56
Figure 3.8: Area Calculation and fill	57
Figure 4.1: Model diagrams for IFT with CO ₂ gas: (a) Normal probability vs. residuals (b) Predicted vs. Actual (c) Residuals vs. predicted (d) Residuals vs. Run .65	
Figure 4.2: IFT vs concentration and pressure (with CO ₂) (a) IFT vs. Concentration (at 2000psi) (b) IFT vs. Pressure (at 18040 ppm).....	66
Figure 4.3: Synergistic effects of factors on IFT (with CO ₂)	67
Figure 4.4: Model diagrams for IFT without CO ₂ gas. (a) Normal probability vs. residuals (b) Predicted vs. Actual (c) Residuals vs. predicted (d) Residuals vs. Run .71	
Figure 4.5: Optimization ramp for IFT with CO ₂	72
Figure 4.6: Optimization ramp for IFT without CO ₂	73

Figure 4.7: Brine/decane IFT vs pressure graph (a) for 722ppm, (b) for 36080 ppm	74
Figure 4.8: Brine/decane IFT vs Concentration graph (a) at 200 psi (b) at 2000 psi	76
Figure 4.9: Brine/ Decane+Dulang IFT vs pressure (a) for 722 ppm (b) for 36080 ppm	79
Figure 4.10: Brine/Decane+Dulang IFT vs concentration (a) at 200 psi (b) at 2000 psi.....	81
Figure 4.11: Spreading coefficient vs pressure graph for Dulang with CO ₂	86
Figure 4.12: Spreading coefficient vs pressure graph for Dulang without CO ₂ ...	89
Figure 4.13: Spreading coefficient vs pressure graph for decane with CO ₂	90
Figure 4.14: Spreading coefficient vs pressure graph for decane without CO ₂	91
Figure 4.15: Spreading coefficient vs pressure graph for Decane+Dulang with CO ₂	92
Figure 4.16: Spreading coefficient vs pressure graph for Decane+Dulang without CO ₂	92
Figure 4.17: Dulang with CO ₂ model graphs (a) Normal % probability vs residuals, (b) Residuals vs predicted, (c) Predicted vs Actual, (d) 3D graph	100
Figure 4.18: Dulang without CO ₂ model graphs (a) Normal % probability vs residuals, (b) Residuals vs predicted, (c) Predicted vs Actual, (d) 3D graph	103
Figure 4.19: Contact angle vs concentration at reservoir condition in water-wet rock	110

Figure 4.20: Contact angle vs concentration at reservoir condition in oil-wet rock	112
Figure 4.21: Graphical analysis of Enhanced oil recovery for decane water wet (a) Residual oil saturation after low sal (b) Residual oil saturation after CO ₂ WAG (c) Final Recovery for decane water-wet	115
Figure 4.22: Graphical analysis of Enhanced oil recovery for decane oil-wet (a) Residual oil saturation after low sal (b) Residual oil saturation after CO ₂ WAG (c) Final Recovery of decane oil-wet	118
Figure 4.23: Graphical analysis of Enhanced oil recovery for Dulang+Decane water-wet (a) Residual oil saturation after low sal (b) Residual oil saturation after CO ₂ WAG (c) Final Recovery of Decane+Dulang water-wet.....	121
Figure 4.24: Graphical analysis of Enhanced oil recovery for Dulang+Decane oil-wet (a) Residual oil saturation after low salinity (b) Residual oil saturation after CO ₂ WAG (c) Final Recovery of Decane+Dulang oil-wet	123
Figure 4.25: Final recovery for high salinity and low salinity water during water-wet condition (@500psi).....	127
Figure 4.26: Final recovery for high salinity and low salinity water during the oil-wet condition (@500psi).....	128
Figure 4.27: Final recovery vs brine salinity for different SC and wettability at 500 psi a) for Low salinity water, b) for High salinity water	129
Figure 4.28: Representation of fluid mobilization and distribution for low salinity and high salinity water under water-wet conditions a) Oil bank formation during low salinity water flooding b) Trapped and unswept oil during high salinity water flooding	132

Figure 4.29: Representation of fluid mobilization and distribution for low salinity and high salinity water under oil-wet conditions a) Oil bank formation during low salinity water flooding b) Trapped and unswept oil during high salinity water flooding134

Figure 4.30: Representation of displacement of fluid during low salinity water flooding using timelapse136

Figure 4.31: Representation of displacement of fluid during CO₂WAG flooding using timelapse.....137

LIST OF TABLES

Table 2.1: Geometry of micromodel.....	24
Table 2.2: Advantages and disadvantages of different micromodel.....	26
Table 2.3: Comparative analysis between different micromodels.....	27
Table 2.4: Different types of micromodel visualization methods.....	29
Table 3.1: Dulang Field Reservoir and Fluid Properties (Abd Shukor, 2014)	42
Table 3.2: Decane Fluid Properties (Linstrom and Mallard, 2001).....	43
Table 3.3: Salinity of the brine samples.....	43
Table 3.4: Brine compositions	44
Table 3.5: Determination of total pore and porosity	47
Table 3.6: General experimental design for IFT experiment.....	49
Table 3.7: General experimental setup of contact angle experiment.....	50
Table 3.8: Actual DOE for IFT (Decane/water)	52
Table 3.9: Actual DOE for contact angle.....	53
Table 4.1: Total RSM models of IFT.....	60
Table 4.2: Actual design matrix for Brine/Dulang IFT	61
Table 4.3: Model summary statistics for IFT between brine/Dulang interface with CO ₂	61
Table 4.4: ANOVA for Cubic model with CO ₂	63

Table 4.5: Actual design matrix for Dulang/ Brine IFT without CO ₂	68
Table 4.6: Model Summary statistics for IFT between oil/water interface without CO ₂	68
Table 4.7: ANOVA for Quadratic model without CO ₂	69
Table 4.8: Spreading coefficient for Dulang with CO ₂	85
Table 4.9: Spreading coefficient for Dulang without CO ₂	88
Table 4.10: Actual design matrix for Contact angle measurement (Dulang with and without CO ₂).....	95
Table 4.11: Sequential model sum of squares	96
Table 4.12: ANOVA for Quadratic model	97
Table 4.13: Fit Statistics	98
Table 4.14: Contact angle calculation with IFT700 and ImageJ for Decane and Dulang with and without CO ₂ oil wet	106
Table 4.15: Contact angle calculation with IFT700 and ImageJ for Decane and Dulang with and without CO ₂ water wet	108
Table 4.16: Factors affecting enhanced oil recovery	126

NOMENCLATURE

Abbreviations

3D	Three Dimensional
Al ₂ O ₃	Alumina
ANOVA	Analysis of Variance
API	American Petroleum Institute
CaO	Calcium Oxide
CBR	Crude Oil, Brine, Rock
CCD	Charged-Coupled Device
CO ₂	Carbon Dioxide
COREOR	Centre of Research in Enhanced Oil Recovery
DOE	Design of Experiment
EDL	Electrical Double Layer
EOR	Enhanced Oil Recovery
FB	Formation Brine
FCCD	Face-Centred Composite Design
Fe ₂ O ₃	Ferric Oxide
HPHT	High Pressure High Temperature
HSSW	High Salinity Sea Water
HSW	High Salinity Water
IFT	Interfacial Tension
IWAG	Immiscible Water Alternating Gas

LSE	Low Salinity Effect
LSW	Low Salinity Water
LSWACO ₂	Low Salinity Water Alternating Carbon Dioxide
LSWAG	Low Salinity Water Alternating Gas
LSWF	Low Salinity Waterflood
LSWI	Low Salinity Water Injection
MgO	Magnesium Oxide
MMP	Minimal Miscibility Pressure
OOIP	Original Oil in Place
PDMS	Polydimethyl Siloxane
PMMA	Polymethyl Methacrylate
pH	Potential of Hydrogen
RSM	Response Surface Methodology
SC	Spreading Coefficient
SiO ₂	Silica
TCMS	Trichloromethyl Silane
UV	Ultra-Violate
WAG	Water Alternating Gas

Expressions

A	Concentration
B	Pressure
P	Pressure/Constant Pressure
T	Temperature/Constant Temperature
V	Volume/Constant Volume

γ	Interfacial tension
γ_{gw}	Interfacial tension of water against gas
γ_{go}	Interfacial tension of oil against gas
γ_{ow}	Interfacial tension of water against oil
Θ	Theta

Units

>	Greater than
<	Less than
%	Percent
μm	Micrometer
Bbl	Barrel
$^{\circ}\text{C}$	Degree Celsius
cm	Centimetre
cm^2	Centimetre Square
cm^3	Cubic Centimetre
cP	Centi Poise
ft	Feet
ft^2	Square Feet
g	Gram
g/cc	Gram per Cubic Centimetre
GPA	Giga Pascal
in	Inches
kPa	Kilo Pascal
m^3	Cubic Meter

mD	Milli Darcy
min	Minute
mL	Milli Litre
mm	Millimeter
MMcf	Million Cubic Feet
MPa	Mega Pascal
mN-m	Milnewton meter
ppm	Parts per million
psi	Pound per Square Inch
rb/stb	Reservoir barrel/ Stock tank barrel
s	Second
scf	Standard Cubic Feet
Scf/stb	Standard Cubic Feet/ Stock tank barrel

CHAPTER 1

INTRODUCTION

1.1 Background

Global demand for crude oil has increased significantly over the last two decades, and as a result, conventional oil supply also decreased day by day. To overcome this problem, advancement and innovation in this field have employed where low salinity waterflooding has lately gained attention as a tertiary injection enhanced oil recovery process. Injection of low salinity water to enhance oil recovery was first reported by Tang and Morrow in 1997. This technique has potential for application in oil recovery because of the lower cost of chemicals, impact on the environment, and easy field implementation (Dang et al., 2013). Moreover, numerous studies have shown that oil recovery from injecting low salinity water was due to alteration of rock wettability by the modification of ionic content in water (Teklu et al., 2014). Among the reasons for wettability alteration are, such as pH elevation, ion exchange, and double-layer effects that occur between the rocks on account of low salinity water injection (Emadi and Sohrabi, 2013). It is widely agreed that a shift in wettability towards a more water-wet environment will result in a decrease in residual oil saturation, hence an increase in oil recovery. This has been shown in experimental works also (Emadi and Sohrabi, 2013; Grattoni et al., 1997; Teklu et al., 2014).

However, in Malaysia, since the fields are already in the mature stage, for further recovery of residual oil requires a tertiary recovery process. In recent literature, it has been suggested that immiscible WAG is the feasible tertiary process (Kulkarni and Rao, 2005). Immiscible WAG that was proposed CO₂ gas to be injected alternately with water. However, the effect of injected water salinity was not addressed in most of the studies. Therefore, there is potential to combine low-salinity water flooding with WAG.

Recent research on the combination of low salinity water flooding with CO₂ WAG has focused more on the core scale investigation (Al-Abri et al., 2019; AlQuraishi et al., 2019; Teklu et al., 2016a). However, to date investigation of the pore scale, has received little attention. Existing study at the pore scale for WAG shows the importance of fluid-fluid and rock-fluid interaction to mobilize the residual oil (Khorshidian et al., 2018). In some circumstances, both rock/fluid and fluid/fluid processes contribute to the low salinity water effect sequentially or simultaneously (Siadatifar et al., 2021). The fluid-fluid interaction involves a combination of gas/oil, gas/water, and oil/water interfacial tension which will assist to determine the spreading coefficient, whereas rock-fluid interaction involves wettability.

According to a study by Keller et al. and Maeda et al., when the fluids have a positive spreading coefficient and wettability is water-wet, spontaneous thin oil film flow occurs, which acts to reconnect residual oil globs to form a bigger oil bank. This oil bank was observed in the micromodel experiment to be mobilized under suitable wettability and spreading conditions. However, from Keller's work, when the fluids have a negative spreading coefficient and wettability is oil-wet, immovable oil globs have been observed between the water and gas phase. These stable oil globs are situated in the pore throat which declines the additional oil recovery during water alternating gas flooding (Keller et al., 1997). The pore-scale studies on WAG mentioned above do not include the effect of salinity. This is because, during low salinity water flooding-WAG, the CO₂ will dissolve in the brine when salinity is decreasing. CO₂ saturated brine will further reduce the brine/oil IFT, and this will affect the spreading coefficient. In rocks, with different wettability conditions, this will also affect residual oil recovery (Maeda and Okatsu, 2008).

Hence in this study, we want to observe how the fluid distributions and mobilization at the pore scale change due to low salinity water injection combined with CO₂ WAG. In this work, fluid-fluid interaction has been observed by measuring interfacial tension involving spreading coefficient at reservoir conditions (pressure and temperature) using Dulang crude oil, and n-Decane and Dulang-Decane mixture. Moreover, in the same reservoir condition, rock-fluid interaction will be observed by contact angle

measurement. Pore-scale investigation using micromodel to visualize the effect of suitable spreading coefficient and wettability (water-wet, oil-wet) condition for low salinity water alternating CO₂ gas. Furthermore, image analysis from the micromodel visualization has been used to evaluate the recovery and fluids distribution and mobilization as a function of wettability and spreading coefficient, under specific operating conditions, different brine concentrations, and different types of oil.

1.2 Problem Statement

Rock wettability and fluids spreading coefficients have been reported as an important parameter which affect fluid distribution and mobilization at the pore scale when the recovery process is under three-phase flow. A previous study on pore-scale for WAG has identified spreading coefficient and wettability under three-phase conditions also affects oil recovery. However, investigation of the pore-scale effect during the combination of low salinity water flooding with CO₂ WAG focusing on the effect of wettability and spreading coefficient has not been reported clearly to date. Moreover, changes in spreading coefficient and wettability when CO₂ is dissolved in low salinity brine has yet to be investigated. Additionally, how the fluids distribute and mobilize at pore scale when spreading coefficient and wettability change due to injection of low salinity water CO₂ WAG is also not sufficiently investigated. Therefore, in this study, we propose to investigate the fluid displacement and mobilization due to the effect of spreading coefficient and wettability when subjected to low salinity water flooding CO₂ WAG.

1.3 Research Objectives

The objectives of this work are as follows.

1. To investigate the fluid-fluid interaction from IFT measurement of oil/water, gas/oil, gas/water IFT with and without the presence of CO₂. These measurements are used to calculate the spreading coefficient as a function of salinity and pressure.
2. To evaluate the rock-fluid interaction from contact angle measurement for oil/water phase with and without the presence of CO₂ to determine the wettability as a function of pressure and salinity.
3. To investigate pore-scale effects of spreading coefficient and wettability on oil recovery during low salinity water alternating CO₂ WAG using micromodel.

1.4 Scope of the Study

This study focuses on the pore-scale investigation of the effect of wettability and spreading coefficient on low salinity water alternating CO₂ gas injection. In order to evaluate the effect of wettability and spreading coefficient, interfacial tension and contact angle are measured by IFT 700, and IFT V4.1.0 software is used for image analysis. In this experiment, brine with a salinity range of 722, 1804, 3607, 7214, 18040, 21400 and 36080 ppm, different types of oils such as Dulang crude oil (Malaysian basin), n-Decane, Dulang-Decane mixture, and carbon dioxide gas are used to investigate the brine-CO₂, oil-CO₂, and oil-brine interactions. Here, the brine salinity has been considered as follows, (722-18040) ppm as low salinity water, 21400 ppm as formation water and 36080 ppm as high salinity water. Pressure is varied from the range of 200 - 2000 psi and the temperature is constant at 96°C for the entire experimental operations. Rising drop and pendant drop methods are used to determine the IFT between different phases, whereas the captive oil bubble contact angle measurement method was applied during the contact angle measurements. In addition, ImageJ software with the Drop Snake plugin has been used to determine the contact angle to

validate the results of the IFT700 software. Ten sets of 3D glass micromodels have been used to visualize pore-scale fluid movements and fluid interactions during low salinity water alternating CO₂ gas experiments under high pressure. The first five sets of micromodels have been utilized for the water-wet system and the remaining five sets for the oil-wet system. This high-pressure condition with transparent micromodel helps to simulate the real reservoir scenario for visualizing the recovery due to change in spreading coefficient and wettability. Eventually, quantitative analysis of oil recovery and phase saturation using ImageJ image analysis is used to calculate the overall recovery for different oil and wetting conditions. This analysis facilitates the way to determine the favorable wetting condition, pressure, and brine concentration for increasing residual oil recovery during low salinity water alternating CO₂ gas flooding.

1.5 Research Significance

At the pore scale, understanding fluid distribution and mobilization in a three-phase fluid flow system will give greater insights for improved recovery. The recovery of residual oil saturation is expected to be increased by applying low salinity water alternating with CO₂ gas. It has been shown that this recovery depends on two major factors, wettability, and spreading coefficient. Change in wettability and spreading coefficient, accelerate the movement of trapped oil inside the pore throat which improves the oil hydraulic connectivity to make an oil bank for additional oil recovery. With different brine salinity, operating condition, and oil phase, wettability and spreading coefficient also change. In this work, a pore-scale investigation using glass micromodel has been conducted to visualize the effect of wettability and spreading coefficient during LSWAG. The results of this study will help to gain more insight into the pore-scale for oil recovery using the combination of low salinity WAG as a function of salinity and pressure.

1.6 Outline of the Thesis

This work has been divided into five chapters. In Chapter 1, the problem background and problem statement are briefly elaborated. Chapter 2 presents the literature review of previous works which is related to spreading coefficient, wettability, and low salinity water alternating gas flooding. The methodology used for the experimental study is described in Chapter 3. The results and discussions are well documented in Chapter 4. Finally, conclusions along with the recommendation for the future study are summarized in Chapter 5.

CHAPTER 2

LITERATURE REVIEW

2.1 Introduction

This chapter reviews the literature related to low salinity water flooding combined with the CO₂ WAG process following a considerable discussion on low salinity water flooding, pore-scale experiments in low salinity water flooding, and water alternating gas. To understand the effect of wettability and spreading coefficient, a section has been presented here titled fluid-rock and fluid-fluid interaction on three-phase flow- EOR. Moreover, an extensive discussion has been presented on a micromodel application in a pore-scale study where micromodel geometry, micromodel materials, micromodel visualization methods, and recent micromodel applications are also presented. As a result, such a detailed review of low salinity water alternating gas EOR along with the effect of wettability and spreading coefficient in pore-scale ease the way to select the convenient technique to run the experiment as well calculate and analyze the result for this project.

2.2 Low Salinity Water Flooding

Low salinity water has been used as a useful approach for oil recovery in recent years where low salinity water flooding received ample attention in the oil industry as an important EOR technique. From recent studies, it has been stated that modification in ionic content of water can play an important role to alter the wettability as well as spreading coefficient (Siadatifar et al., 2021; Teklu et al., 2016a). These two factors act a vital role at the time of increasing residual oil recovery. The oil recovery factor of traditional water flooding can be improved by up to 38% by changing the composition of injected brine, leading to a new definition of optimum water flood brine injection composition (Lager et al., 2008; Liu et al., 2021). It also recovers around 6.1% more of the original oil in place (OOIP) than the high salinity water floods. Extensive laboratory experiments confirmed that there is some advantage of low salinity water injection rather than high salinity water injection during secondary and tertiary recovery (Fredriksen et al., 2016; Zhang and Morrow, 2006). Due to its oil recovery performance and relatively simple, environmentally friendly implementation, low Salinity waterflooding

(LSWF) is an emerging attractive EOR method when compared to conventional high salinity water flooding and EOR approaches (Emadi and Sohrabi, 2013). More importantly, LSW has an additional advantage in that it can be integrated with other EOR methods (in hybrid LSW processes).

Different processes are suggested in the literature to characterize the efficiency of LSWF, including the influence of water salinity on oil recovery (Morrow and Buckley, 2011; Sheng, 2014). However, the interaction between the Crude Oil, Brine, and Rock (CBR) system under consideration determines the efficiency of each or some of these processes during LSWF such as fines migration and rock dissolution (Chequer et al., 2019; Yu et al., 2019), p^H increase (Austad et al., 2010), multi-component ion exchange (Austad et al., 2010) and a double layer expansion (Dang et al., 2013; Pu et al., 2010). Mechanisms for LSWF will be discussed elaborately in the following subsections.

2.3 Pore Scale Experiments in Low Salinity Water Flooding

In the recent decade, pore-scale studies are being conducted in a wide range to visualize fluid distribution and mobilization. Usually, the pore-scale investigation takes place by micromodel. Sohrabi et al. (Emadi and Sohrabi, 2013) used high-pressure transparent micromodels to examine the mechanisms and interactions involved in low salinity water flooding. In his initial micromodel experiment, he used high salinity brine as both connate and injection water in this water flooding method and observed no significant improvement in recovery due to the low salinity contrast between connate and injection water. In his experiment, he saturated the micromodel with high salinity water and then flooded it with oil to establish the initial distribution of oil and water. When oil is exposed to water with low salinity, specific interactions occur, according to the results of these experiments. Connate water with low salinity can lead to the development of black particles as a result of these interactions. Low salinity water or the injection of oil into low salinity brine can cause an immediate color change, which indicates that black particles (or water micro-dispersions) are forming spontaneously. Interestingly, when the same oil was flooded with high-salinity brine, no color change was noticed.

Amirian et al. utilized a two-dimensional clean glass micromodel which was coated with clay to analyze the dynamics of displacement throughout LSWF, with the wettability status

specified at both water-wet and oil-wet situations. As a result, pore-scale displacement processes in the presence and absence of clay, as well as in two-phase flows dominated by drainage and imbibition, were investigated. LSW inhibited "snap-off" in water-wet systems in the absence and presence of clays, perhaps due to the formation of a viscoelastic water-oil interface. For oil-wet systems, the wettability shifted toward greater water wetness. The observations are explored in terms of the Electrical Double Layer's effect (EDL) (Amirian et al., 2017).

Low salinity water flooding with micromodels was utilized by Mahzari et al. in 2018 and observed the formation of micro-dispersion of water in oil when LSW and crude oil were in contact. Using numerous crude oils facilitates the way to discovering how micro-dispersion generation depends on low salinity water injection (LSWI) and surface wettability. According to the result of the study, it can be stated that after a long period, mixed-wet conditions were found to release the trapped oil and produce micro-dispersions after tertiary low salinity water injection. Oil recovery and wettability changes were not noticed when a crude oil with a low or non-existent tendency to form micro-dispersions was used. Moreover, LSWI in waxy crude oil using other methods is more challenging or impossible. Testing with a range of crude oils revealed that LSWI's ability to improve oil recovery depends significantly on the crude oil's surface wettability and micro-dispersibility (Mahzari et al., 2018).

According to Fattahi Mehraban et al., the first-time fluid interactions at reservoir conditions (50°C and 2000psi) has been studied using a micromodel in 2020. The micro dispersion and surface charge of numerous crude oil samples were analyzed in this study. Researchers found that micro dispersions have a key influence on oil swelling and wettability change in porous media, which increases microscopic sweeping efficiency and, thus, a higher oil recovery. Before waterflooding operations, water micro dispersion can be a considerable approach for oil reservoirs.(Fattahi Mehraban et al., 2020).

Mohammadi et al. (Mohammadi and Mahani, 2020) conducted numerous displacement tests by flooding an oil-saturated micromodel with high salinity water and then injecting low salinity water to replace the high salinity water and examine any potential changes in the configuration and saturation of the residual oil. Moreover, to account for the spatial effects of the low salinity process, the studies were tracked for many days to a month. The data demonstrate clearly that decreasing brine salinity improves microscopic sweep efficiency,

giving direct in-situ evidence for wettability change toward a more water-wetting state. Finally, it has been observed that the amount of oil remaining under low salinity was significantly smaller than at the end of the high salinity injection.

To better understand how low salinity impacts an oil field with distinct layers of limestone and sandstone, Siadatifar et al. conducted a study. To get a clear understanding of the fluid-rock interaction, contact angles and Interfacial Tension (IFT) measurement took place, and effects of low salinity were observed with visual investigation using micromodels. In this work, for secondary and tertiary injection scenarios, different salinity levels were used, and it has been observed that the low salinity effect (LSE) can occur when high and low-salinity water are introduced simultaneously. During high salinity water flooding with an oil-wet condition, the oil trapping mechanism was commonly snap off, fingering, and bypassing for both limestone and sandstone. Whereas high salinity water flooding has a minimal effect on the redistribution of saturation in water-wet micromodels. For LSWF, it has been observed that it is highly successful in oil-wetting situations. presence of a continuous oil film that is beneficial for LSE's performance. Due to the lack of a snap-off trapping mechanism, visual examinations imply that the visco-elastic interface may be the dominant mechanism for LSE in the examined fluid-rock interactions. Finally, from the overall observation, it can be stated that the measured IFT and contact angles can't account for the observed LSE (Siadatifar et al., 2021).

After overall discussion, pore-scale investigation of low salinity water flooding broadens the way to understand the effect of low salinity on overall recovery. Undoubtedly, it is a better technique than high salinity water flooding. During low salinity water flooding, suitable wettability alteration is happening as well as micro dispersion is visible actively. The double-layer effect, multi-component ion exchange, and p^H elevation also played an important role to improve the recovery during low salinity water flooding.

2.4 Water Alternating Gas

A significant amount of remaining oil can still be recovered by WAG injection in reservoirs that have been flooded with water or injected with gas. In a three-phase regime, the WAG injection process integrates the imbibition and drainage mechanisms during successive injections of gas and water cycles. WAG injection is a technique that involves injecting alternate slugs of gas and water into the reservoir to recover additional oil left behind by water

injection. The microscopic movement of the gas flooding by WAG injection combines improved microscopic efficiency and a better macroscopic injection. WAG injection was proposed initially to improve the sweep efficiency of gas injection, mainly by using water to control the mobility of the displacing gas and to stabilize the front (Christensen et al., 2001). WAG injection has the potential to recover oil by contacting unswept zones, as gas segregates to the top and water accumulates at the bottom. WAG injection results in a lower residual oil saturation than for waterflood or gas floods alone (Skauge et al., 2007). Distribution and fluid flow in pore level was examined, and fluid saturations were calculated at various stages of the experiments. The results showed that the recovery of oil under any of the wetting conditions was higher for WAG injection than for water or gas injection alone. WAG recovery was also found to be higher for strongly oil-wet or mixed-wet models than for strongly water-wet ones (Sohrabi et al., 2001).

Initially Land (Land, 1968) offers an optimal gas saturation following an imbibition operation, such as waterflooding, that results in the lowest possible residual oil saturation in 1968. The author accepts that residual saturation takes up the same amount of space in a three-phase system as it does in a two-phase system, i.e., trapped gas takes up pore space that would otherwise be filled by trapped oil. Reduced relative permeability to oil results in an unfavorable mobility ratio, which decreases displacement efficiency.

In glass micro-models, Sohrabi et al. performed a series of capillary dominating WAG injection tests. Regardless of wettability, they found that the WAG injection technique yielded greater oil recovery than either water flooding or gas injection alone. Oil-wet and mixed-wet systems' WAG injections are more efficient than water injections, according to a report. Additional injection cycles result in a progressive increase in oil recovery in mixed-wet models, however, there is no substantial oil production in oil-wet or water-wet systems after two cycles (Sohrabi et al., 2004). Sohrabi and Jamiolahmady used a strongly water-wet glass micro-model to conduct a high-pressure pore-scale visualization investigation to better understand the WAG injection mechanisms under various wettability settings. The investigations demonstrated that gas entrapment results in a decrease in relative permeability and injectivity. Indeed, subsequent injection of the water and gas cycles fragments and traps the gas in pores, restricts the available area for water to flow, and so diminishes relative permeabilities (Sohrabi et al., 2009).

2.4.1 Miscible displacement

When gas is injected at a pressure higher than the reservoir oil's minimal miscibility pressure (MMP), miscible displacement occurs. The MMP is related to reservoir temperature and the quantity of C5-C30 components in the hydrocarbon mix. The MMP is the pressure at which the injected solvent and the in-situ oil can achieve first- or multiple-contact miscibility (dynamic miscibility) at a constant temperature. Furthermore, the interfacial tension should be zero at the minimal miscibility pressure, and there should be no interface between the fluids (Nijjer et al., 2019).

According to studies, a miscible technique recovers more oil than an immiscible one (Kulkarni and Rao, 2005). Displacement in a miscible process is often accomplished using a condensing or vaporizing mechanism. In condensing gas drives, in-situ miscibility is generated by gradually enriching reservoir fluids in intermediate components of a solvent until the injected solvent and enriched oil become miscible.

The in-situ creation of miscibility happens in the vaporizing drive due to the solvent's extraction of intermediate components of the reservoir fluid and its steady enrichment with these intermediates as it flows in the reservoir. Moreover, this is primarily accomplished under high pressure by injecting natural (hydrocarbon) gas, flue gas, or nitrogen. When high-pressure nitrogen is injected, it can form a miscible slug that aids in the release of oil from reservoir rock (Alagorni et al., 2015).

2.4.2 Immiscible displacement

In an immiscible water alternating gas (IWAG) process, gas and water are injected alternately at a pressure less than the minimum miscibility pressure. This is done until a specific volume of gas is injected, and then continuous water injection happens. This type of WAG method has been used to reduce viscosity and improve frontal stability for contacting unswept zones (Spivak et al., 1990). IWAG has been used in reservoirs where gravity-stable gas injection cannot be used due to gas resource constraints, as well as in low dip reservoirs with high heterogeneity. In addition to sweeping, the efficiency of tiny displacement is increased.

During an immiscible gas flood, swelling is a significant compositional consequence that occurs (Skauge et al., 2007). The volume of gas dissolved in the oil will increase until the oil

is saturated at the reservoir pressure if the oil is under saturated at that pressure or if gas injection increases the reservoir pressure. The oil formation volume factor (FVF) increases as the volume of gas in the oil increases. Swelling causes oil to take up more space for a given mass or mole, which is known to improve the efficiency of the gas-oil displacement process. When it comes to enhancing the mobility of in-situ oil, oil swelling and viscosity reduction happen together.

In a matured Malaysian basin (Dulang field), 101.667 Celcius and 2875 psig is the minimum pressure for CO₂ miscibility in Dulang oil, which is higher than its initial reservoir pressure (1800 psig) (Nadeson et al., 2001). Therefore, according to this work, it has been observed that immiscible WAG injection is more advantageous in the Dulang field than miscible WAG injection. In his study, a waterflood has been conducted with a water-wet core and 56.8% of the original oil in the well was successfully recovered and three consecutive gas/water injection cycles led to an extra 6.2% of the original oil in place being recovered. Additionally, there was evidence that additional oil may have been extracted from the core via vaporization. While flooding occurred, there was evidence of permeability loss in the composite core. This may be happened due to the movement of fines and the blockage or clearing of pore throats. The presence of kaolinite and illite in the core material was also detected in the experimental analysis.

The produced CO₂-rich gas and the vaporization of Dulang crude by pure CO₂ were investigated by Kechut et al. in 2001. Using pure CO₂ in a laboratory trial, 15% of the stock tank oil was vaporized. From the experimental analysis it has been stated that, at operational reservoir pressure of 1400 – 1800 psig, the vaporization varies from 2–5 percent. According to the analysis, it can be said that the cost-effective recovery method is an immiscible one that utilizes generated gas with high CO₂ concentrations. WAG technology also has the potential to enhance mobility control and sweep performance (Kechut et al., 2001).

Immiscible CO₂ flooding, compared to CO₂ miscible flooding, reveals the huge potential under varied reservoir/fluid conditions. With an average injection efficiency, CO₂ immiscible flooding can recover an additional 4.7 to 12.5 percent of the oil. This technology can be used in light, medium, or heavy oil reservoirs. In immiscible WAG flooding, the composition and source of CO₂ play an important role. Most of the CO₂ gas came from the near gas field or plant emission which contains numerous impurities. Furthermore, other field applications are

employed with 70% CO₂ gas whereas Dulang is the field that contains the lowest CO₂ gas due to limited sources (Zhang et al., 2018).

2.4.3 CO₂ Gas as EOR Solvent

With cost-effective extraction technology, CO₂ became a desirable EOR solvent. CO₂ has three characteristics that make it an effective EOR solvent and in Figure 2.1 the advantage of CO₂ as a solvent has been presented. Firstly, it reduces the viscosity of the solution (Li et al., 2013), secondly, it can be sequestered in the subsurface (Esene et al., 2019), and finally, it is readily available in the environment at a cheaper cost. However, employing CO₂ to reduce heavy oil viscosity has certain technological and economic problems. Formation damage, wettability alteration, reservoir flow disruption, and surface facilities may cause due to CO₂ injection. Corrosion issues are also connected with the use of CO₂ in salty brine environments particularly in the presence of dissolved oxygen. In terms of economics, the operating costs are greatly increased by the unavailability of CO₂ in some parts of the world.

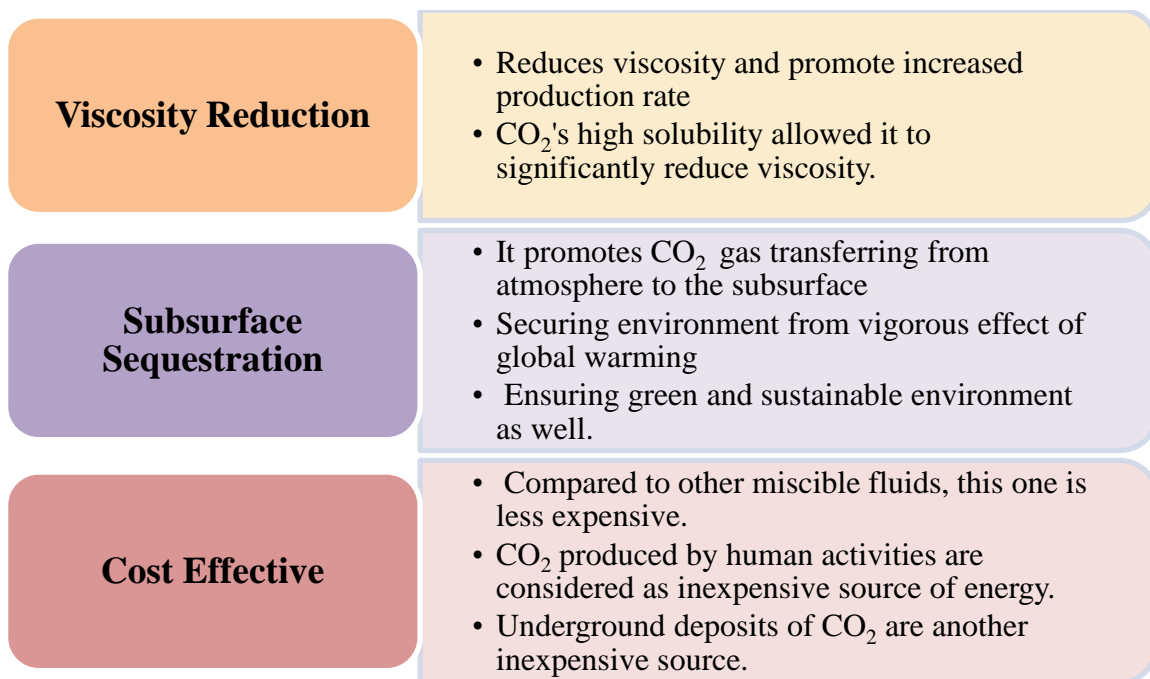


Figure 2.1: Advantages of CO₂ gas as EOR solvent

2.4.4 Carbon Dioxide WAG Flooding

It has been investigated that continuous CO₂ flooding is giving less recovery than water alternating gas flooding. It has been observed in one work that recovery increases with the solubility of CO₂ in brine. When CO₂ gas is more soluble in brine the recovery is not significant but when it is less soluble in brine then the recovery is higher (Jiang et al., 2010). However, in other work, they observed continuous CO₂ flooding is giving better results than WAG flooding. Also, more CO₂ solubility in brine facilitates the shift in wettability as well as spreading coefficient which accelerates the increase in oil recovery (Kulkarni and Rao, 2005).

The injection of CO₂ gas alternating with water reduces the mobility contrast (gas and reservoir fluid) and the degree of viscous fingering in a gas miscible flooding reservoir. In the WAG process, water and CO₂ gas can be injected alternatively or simultaneously. To achieve higher sweep efficiency water is used to control the mobility of the gas. In miscible gas injection, the efficiency of microscopic displacement is higher. The WAG performance is significantly affected by rock wettability reservoir heterogeneity, fluid properties, miscibility condition, injection techniques, and well operational parameters (Chen et al., 2010).

In a water-wet micro-model, Dong et al. studied the displacement process during IWAG injection where a stable oil layer has been noticed. In particular pores, oil/water blobs were absent as gas bubbles already occupied them all. Due to the high-water saturation and lack of oil discontinuities, a considerable decrease in oil recovery was observed. Additionally, unfavorable gas mobility extends a noticeable amount of fingering in the oil channel (Dong et al., 2005).

Injection of miscible CO₂-WAG in water- and oil-wet glass beads porous systems was done by Jackson et al. A WAG ratio of 1:1 was utilized with 30% porosity. Noticeable recovery has been observed with secondary and tertiary WAG injections in water-wet and oil-wet systems. Interestingly, the secondary WAG process in the water-wet system gave higher oil recovery than the tertiary WAG process. Furthermore, in oil-wet conditions, during tertiary WAG flooding the recovery was higher than secondary WAG process (Afzali et al., 2018).

2.5 Low Salinity Water Alternating Carbon Dioxide Gas

Low salinity water alternating CO₂ gas is a new technique to improve the recovery of irreducible oil saturation in the reservoir. Individually low salinity water and CO₂ flooding are two successful recovery processes. So, the combination of these two techniques will be the greatest invention of this era (Teklu et al., 2016b). While LSW represents an emerging EOR technique, WAG is a proven method for improving gas flood performance by controlling gas based on wettability modification mobility. The unfavorable mobility of pure gas flooding results in viscous fingering which reduces the effectiveness of volumetric sweeping. WAG helps to overcome this problem by reducing the large amount of gas needed for EOR projects, which is especially important in offshore oil fields (Dang et al., 2016).

CO₂ LSWAG is a promising EOR technique as it not only combines the advantages of CO₂ injection with low salinity water floods but also facilitates synergy between these processes through interactions between geochemical reactions associated with CO₂ injection, ion exchange processes, and wettability alterations (Barnaji et al., 2016). Teklu and Alameri proposed a new EOR method that requires low salinity water mixing with CO₂ WAG injection. They used three core floods and several contact angles and IFT measurements in their work. The core flood includes seawater flood followed by low salinity water, followed by CO₂ injection and they observed that the recovery increased gradually with this injection process. They calculated the contact angle on several types of permeability using different salinity. From their experiment, it has been found that the solubility of CO₂ in brine increases with a decreasing water salinity. At high reservoir pressure and temperature, they compared the solubility of CO₂ in water with zero salinity and brine of 100000 ppm total dissolved solute. After this experiment, they observed that CO₂ solubility increment with low salinity can lead to improving oil recovery through CO₂ brine IFT reduction. Favorable IFT alteration depends on the temperature, pressure, and salinity of the water. They have found that this process is economically profitable too (Teklu et al., 2014).

Keller et al. conducted an experiment in 1997 where low capillary numbers were used to detect the presence of pore-scale displacement processes, and stable oil layers were found between the wetting and non-wetting phases. There was no significant movement of oil in molecular films, hence flow rates through these films are insignificant. When decane was present, there were no direct gas/water displacements observed. For the air-decane-water

approach with a negative spreading coefficient, stable oil layers have been found in a porous media. After decane imbibition, the remaining air linked to the output port either displaced most of the air or is retained in air bubbles. Most of the decane has also been transferred to other parts of the micromodel, as the water flows through the pores and replaces the decane. When it comes to pore-space configurations, the majority of displacements seen include only two phases in motion, with the third phase being held in place by capillary forces. Water and oil layers play an important role in the drainage cycle under three-phase circumstances, allowing oil and water to move with low saturation levels (Keller et al., 1997).

A new experiment has been carried out by Grattoni et al. to provide more evidence that rock wettability has a major effect on the output of gas production from residual oil. The evolution of gas saturation in three-phase systems has been studied under a broad range of conditions, in particular, critical gas saturation (Al-Aulaqi et al., 2011). The magnitude of the critical gas saturation was approximately the same for the water-wet system, regardless of whether the oil was spreading or not, but was much lower in the oil-wet case. Maximum or final gas saturation has equal values for all water-wet cases and a higher value for oil-wet systems. The gas saturation reached at the end of the experiments has a limited variability range (30%–33%). These findings indicate that there might be little effect on final gas saturation of the wettability and distribution characteristics of gasoline. The ratio of oil to water is lower for non-spreading oil than oil dispersed under water-wet conditions, indicating the negative impact of discontinuous oil on the flow (Grattoni et al., 1997).

The recovery of oil was substantially higher with the positive spread system has been stated from Oren et al.'s work. The higher displacement efficiency was the product of the flow-through thin but continuous oil films, which had always separated the oil and water phases in the positive distribution system and reconnects much of the original residual oil. The shortage of oil films and the likelihood of direct gas/water displacement limited the recovery of oil for the negative distribution system. Therefore, oil recovery is significantly higher for positive spread systems than for negative spread systems (Oren and Pinczewski, 1994). Oil is displaced by a double-draining mechanism for both positive and negative spread systems. Double drainage events (gas / oil-and oil / water-interface movements) occur in the immediate vicinity, which means that mobile gas will always be present in the vicinity of mobile oil. There is a close correspondence between oil and water recovery for positive dispersion systems because the movement of the gas/oil interface always results in the movement of the oil/water interface.

The correspondence between oil and water recovery for a negative spread system is much weaker than for a positive system. Gas/water displacement is possible for a negative spread system; therefore, not all gas displacements result in oil/water displacement (Oren et al., 1992).

Oren's study provides a detailed explanation of the fluid distribution and pore-scale displacement mechanisms for the three-phase flow under strongly wet conditions when the displacement fluid is in a non-wetting phase. When one of the phases strongly wets the solid, the pore-scale distribution of the three phases in the porous medium is entirely determined by the wettability, capillary pressure, and the distribution behavior of the fluids. The three-phase displacement mechanism may be described by the simple generalization of the previously described two-phase flow mechanisms in which the role of wetting in the two-phase flow is replaced by three-phase displacement. Low salinity water alternate CO₂ gas injection improves oil recovery of conventional water alternate gas flooding by forming in situ carbonated water of higher CO₂ saturation in the brine phase. Higher CO₂ saturation in the brine phase would mean slightly lower CO₂ concentration in the oil phase, which would seem an overall reduction in oil recovery. On the other hand, a higher CO₂ injection during the brine injection would increase the alteration of wettability and reduction of IFT, followed by increased recovery of oil. The unfavorable mobility of pure gas flooding results in viscous fingering, which reduces the efficiency of the volumetric sweep.

A series of experiments has revealed that the salinity of the injected water can have a significant effect on the enhancement of oil recovery (Moradpour et al., 2021). The best results were obtained with low salinity brine, which increased the contact angle significantly. The presence of gas phases enhanced the wettability modification over their absence. Emulsion formation investigations confirmed the brine's superior performance after dilution. In this scenario, the number of waters in oil emulsion droplets generated was around two times more than in SW. Stable emulsions aid in the displacement of oil by modifying the wettability of low-salinity water due to their osmotic activity. Finally, the synergistic impacts of this strategy on oil recovery were demonstrated by an improvement in incremental oil recovery using low salinity water alternating gas flooding.

A positive or a negative influence on oil recovery might be caused by the solubility of the injected gas in the alternatively injected water during LSWAG was observed by Ramanathan et al. in 2015. The study has shown that brine solubility can be increased by lowering the ion

content. Due to the reduction in free gas, oil swelling, mobility ratio and recovery factor would be improved (Ramanathan et al., 2015).

Therefore, CO₂ LSWAG is expected to promote the synergy of two separate process mechanisms, thus overcoming the frequently encountered late production problem at conventional WAG (Jones Jr, 1964). For a successful recovery from Low salinity water alternating CO₂ gas, numerous factors should have under consideration. Wilson et al. has described the explanations from different literature and tried to detect the factors affecting enhanced oil recovery. Wettability change toward higher water-wetness during LSW is commonly acknowledged as the source of the enhanced oil recovery. Low-salinity brine has been shown experimentally to have a significant effect on the shape and relative permeability curves (Wilson, 2015).

2.6 Fluid-Rock and Fluid-Fluid Mechanisms in Three-Phase Flow- EOR

Understanding the fluid-fluid and rock-fluid interaction mechanisms in three-phase flow is an important feature to predict the performance of the reservoir. These are considered key properties to enhance recovery. fluid/fluid interactions (which occur at the oil/water interface) are considered interfacial tension and fluid/rock interactions (which occur at the water/rock contact) are as contact angle. From fluid-fluid interactions change in spreading coefficient happens as well as from rock-fluid interactions wettability change takes place in the three-phase flow. From experimental studies, it has been established that the spreading coefficient increases the residual oil recovery associated with porous medium wettability (Fjelde et al., 2012; Øren and Pinczewski, 1995; Teklu, 2015). The solid-fluid system controls the fluid configuration in the pore space and indicates the fluid's affinity to being in contact with the solid surface controlling the balance between adhesive type (fluid to the surface) and cohesive type (liquid to liquid) intermolecular interactions. In other words, wettability indicates rock surface affinity for the oleic or aqueous phase (Y C Araujo et al., 2001) and attempts to occupy the maximum area. Wettability varies from full water-wet to fully oil-wet. For a fully water-wet reservoir, small pores are filled with water and most of the rock surface is in contact with water. If the rock has no strong preference for oil or water, it is an intermediate or neutrally wet reservoir. In a fully oil-wet reservoir, oil covers most of the rock surface and small pores. Furthermore, the spreading coefficient is a measure of the liquid phase's tendency to spread

(complete wetting) over a second liquid or solid phase. Specially, spreading of oil does play an important role in order to increase the recovery (Mani and Mohanty, 1997).

After consecutive experimental data analysis, it has been observed that negative spreading has a lower recovery in comparison to positive spreading (Oren and Pinczewski, 1994). A positive oil spreading is where it has a continuous film of oil which will cause the production of oil to be more effective and leave no blob of oil in the reservoir. Moreover, residual oil saturation is observed lower with positive spreading compared to negative spreading. Immovable stable oil in the pore throat without forming any thin film of oil facilitates higher residual oil saturation and this situation represents a negative spreading coefficient. The spreading coefficient has multiple types of configurations. According to Grattoni et al, the pore space which is occupied by three-phase tends to take a particular arrangement and configuration which is controlled by interfacial tension and wettability. These arrangements are usually used to explain the fluid flow and how it is distributed with the pore structure. The configuration will eventually affect the flow and trapping mechanisms (Grattoni et al., 1997).

Oren described three-phase fluid distribution for pore-level fluid delivery of oil, water, and gas in a micromodel with a positive or negative spreading system under intensely oil-wet conditions and observed continuous oil films in the network and ideally occupies pore throats when oil is in the wetting phase (Oren et al., 1992). Also in 1994, from his experiment, he obtained the highest recovery for oil-wet displacement for both positive and negative spreading systems and a significant amount of oil film was present. Surprisingly, the recovery was lowest for the negative spreading water-wet system where there was no oil film detected (Oren and Pinczewski, 1994).

Although it was initially considered that only spreading oils could form oil layers in a porous medium, Dong et al. (1995) have theoretically predicted and experimentally verified that non-spreading oils can form thick layers in the crevices of the pore space, depending not only on the spreading coefficient and capillary pressures but also on the geometry of the crevice. Thick oil layers may provide additional channels for oil flow at low oil saturations, resulting in very low residual oil saturations. The role of oil layers is important in modeling the flow of three phases in the subsurface.

A rapid oil (iso-octane) layer flow has been observed in the corners using capillary tubes with a square cross-section, in an environmentally significant timeframe. In micromodel

studies, oil layers have been observed for Soltrol, which is spreading (Oren and Pinczewski, 1995). For non-spreading oils, Oren and Pinczewski (1995) and Oren et al. (1992) did not observe oil layers.

It has been observed that very low oil residues can be achieved through the injection process, particularly for systems with a positive spreading coefficient (Mani and Mohanty, 1997). The spreading coefficient affects not only the residual oil saturation but also the capillary pressure curve. Furthermore, microscopic flow mechanisms (meniscus displacement) are affected by the wettability and spreading coefficient. This motivates the assessment of the wettability and spreading coefficient's effects on relative recovery also (Kalaydjian et al., 1997).

Vizika et al. aimed to find out the effect of wettability and spreading coefficient in a three-phase fluid system, and from his work, he got more recovery for water wet and positive spreading coefficient system whereas for oil-wet system and negative spreading coefficient the recovery was not significant as previous one. For the fractional wettability also with a positive spreading coefficient, the overall recovery was satisfactory. From this work, the effect of these two parameters on fluid mobilization and distribution has been observed and described extensively (Vizika et al., 1998).

Moreover, according to Araujo et al.'s findings, there is a noticeable relationship between relative permeability and oil recovery. Oil recovery and relative permeability are higher for spreading conditions. Depending on the nature of the rock surface and the liquids present in the system, spreading coefficients can have positive or negative values. In the case of a water-oil-gas system, in the presence of gas, the oil phase can spread on the water. This method encourages the oil's hydraulic consistency, leading to very low residual saturation of oil. Whereas, for a negative spreading coefficient, the value of relative permeability is small, and it happens because of path blockage (where most of the fluid gets blocked and residual oil saturation increases) (Y. C. Araujo et al., 2001).

Khorshidian et al. observed from their work, that in water-wet micromodels most of the water occupied the area around smaller throats and solid grains which prevented active oil film from forming and subsequent drainage. On the other hand, micro-capillaries and smaller pores around grains in oil-wet micromodels contained residual oil, which appeared as oil rings. From the overall finding, he observed that capillary continuity of the oil phase has been reported to

be stronger in the oil-wet micromodel and the possibility of enhanced oil recovery was predicted from the oil-wet condition (Khorshidian et al., 2016).

From all the descriptions of the study, we can say that the spreading coefficient and wettability has been considered to be an influential factor during oil recovery in the tertiary stage. Various studies have been reported on this hybrid process under ambient pressure and obtained positive results regarding enhanced oil recovery. Although work has been reported in core scale and pore-scale visualization. This discussion on fluid/fluid and rock/fluid interaction and its influence on enhanced oil recovery have enriched the idea about these two parameters. Moreover, it has been observed that an enriched idea on these parameters would help to overcome lower oil recovery problems, and therefore these parameters need further investigation. Though it has not been investigated widely yet and this is a gap addressed regarding fluid/fluid and rock/fluid interactions in the current study. However, proper and extensive investigation can facilitate the way to overcome this gap.

2.7 Application of Micromodel for Pore-Scale Study

In this section, the application of micromodel for pore-scale study has been discussed along with micromodel geometry, material, a visualization tool, and the recent application of micromodel. A detailed discussion has provided a clear idea about micromodel geometry and material which helped to select the material, configuration, and design during this project. After that, a brief discussion on visualization and the recent application of micromodel facilitates the idea behind three-phase fluid/fluid and rock/fluid interaction in pore-scale investigation with micromodel for this project.

2.7.1 Micromodel Geometry

To investigate the pore-scale phenomena, the micromodel needs to be designed with the pore geometry resembling the actual rock as much as possible. Initially, with the limitation of technology, in the 1950's the pore geometry was simple regular shapes repeated in a pattern. Over time, the design evolves as the technology matures and the pore-scale investigation requires a more realistic representation of the pore structure. The pore geometry typically used in micromodel construction can be classified into four patterns based on their geometry and

topology. These are the ideally structured micromodel, the moderately structured, fractal patterns, and non-uniform or irregular micromodel.

Also, micromodel porosity depends on packing arrangement and particle shapes. It has shown that particles of irregular shape are more prone to having higher porosity values than those of uniform shape because their angularity could allow them to be packed more tightly together in the same amount of space as larger, flat objects. Particles of irregular shapes tend to have a more surface area and higher permeability. Sand packing density decreases with decreasing grain size. This means more space (pore volume) for particles to pass through. Also, when all grain sizes are perfect spheres, porosity is independent of absolute grain size, and sphericity is defined as the ratio of length to the diameter of grains. From above idea represents, an irregular pattern facilitates more porosity than other patterns. Further explanation of the pore geometry in the micromodel design is presented in Table 2.1.

Table 2.1: Geometry of micromodel

Types	Description
Ideally structured model	The geometry is properly maintained all over the network and the geometry will be the same throughout the micromodel (Corapcioglu et al., 1997). In this type of micromodel, factors like the depth of the pore, the interval between each pore, and the width of the pore are constant for the complete micromodel (Kennedy and Lennox, 1997)(Lu et al., 1994). Fluid migration (Conrad et al., 1992), visualization (Wilson, 1994), viscous fingering (Chen and Wilkinson, 1985), hydraulic conductivity (Corapcioglu et al., 1997) measurement experiments have been examined through this model.
Moderately structured model	This model has little similarity with the previous one but there are some distinct differences between them. The cross-sectional shape is similar to an ideally structured model but pore width, depth, and the interval between each pore are not the same for it (Tsakiroglou and Avraam, 2002). Additionally, pore size distribution affects the entire micromodels permeability (Sbragaglia et al., 2007).
Fractal patterns	The representation of the porous medium in some micromodels formed in the last few decades is focused on rock fractures. Although this two-dimensional structure of micromodel tends to be more representative of fractured rock, when it is isotropic, the fractional framework acts like porous media, and the fracturing density is high (Corapcioglu et al., 1997). For this pattern, correlation network porosity has to be at least 50% if less than that there is a high chance of not having any interconnection across the micromodel (Cheng and Giordano, 2002).
Non-uniform or irregular patterns	In this pattern, the entire geometry is uneven, and the pores are distributed randomly without any significant height, width, and the interval between each pore. Based on Single statistical distribution the pore size for entire systems has been selected. It has no well-defined geometry (Sandnes et al., 2007).

2.7.2 Micromodel Materials

To get meaningful insight from micromodel experiments, the porous media of the model should be transparent under visible light for direct visualization of fluid flow. Glass and silicon micromodel are the most used micromodels due to material availability and a high degree of transparency leading to more accurate visualization. Recently, polymer-based micromodel such as polydimethyl siloxane (PDMS) and polymethyl methacrylate (PMMA), calcite micromodel especially for carbonate reservoirs are also used for visualization (Schneider et al., 2011). In this section, the discussion will cover the types of micromodel fabrication material, their advantages, and disadvantages. The materials that will be discussed are glass-based micromodel, silicon-based, polymer-based, and micromodels fabricated from other materials.

In Table 2.2, the advantages, and disadvantages of the abovementioned micromodels according to the material difference have been described. Moreover, a comparative analysis will help to choose the proper micromodel according to anyone's operating condition as well as the experimental state. In Table 2.3, the comparative analysis takes place within the abovementioned micromodels as well as their flexibility, effectivity, expense, and economical aspect.

Table 2.2: Advantages and disadvantages of different micromodel

Micromodel type	Advantages	Disadvantages	References
Glass micromodel	<ul style="list-style-type: none"> Any network design can be reproduced from an image or developed by a computer. Easy to shape up and polish with a high degree of precision. Can withstand huge loads due to its rigid and stiff quality. Does not with the samples. Recyclable. 	<ul style="list-style-type: none"> Being fragile must be handled with care. A sharp edge may cause an accident. 	(Mahmoodi et al., 2018b)(Javadpour and Fisher, 2008)(Karadimitriou et al., 2012)(Silverio and de Freitas, 2018)
Silicon micromodel	<ul style="list-style-type: none"> Rigid than glass and can operate at high pressure, high temperature, and high flow rates. Can withstand extremely high temperatures up to 1400°C. Difficult to shape up. Recyclable. Wettability can be easily modified by the silanization method. 	<ul style="list-style-type: none"> Visible light cannot pass through silicon material which hinders clear visualization. Containing different materials with different wettability makes it typically undesirable in two-phase flow experiments. 	(Silverio and de Freitas, 2018)(Anbari et al., 2018)(Gerami et al., 2019)
Polymer micromodel	<ul style="list-style-type: none"> Low production costs due to the availability of polymer and it can be made in a typical laboratory Wettability can be easily treated using treatments such as plasma treatment, UV ozone, polyelectrolyte multilayer coating. 	<ul style="list-style-type: none"> Deformation can occur under low pressure (<100kpa). Poor chemical resistance. Cannot sustain high pressure, high temperature, and high flow rate. 	(Javadpour and Fisher, 2008) (Anbari et al., 2018) (Zarikos et al., 2018) (Silverio and de Freitas, 2018) (Kim and Meng, 2015) (Gerami et al., 2019)

Table 2.3: Comparative analysis between different micromodels

Parameters	Glass Micromodel	Silicon micromodel	Polymer micromodel
1. Degree of precision	Simple polishing with a high degree of precision.	Not as precise as glass micromodel. The presence of two types of material arises some issues.	The degree of precision of polymer micromodel is good.
2. Manufactural Flexibility	Less difficult to give it a shape.	Being more rigid than glass micromodel it is difficult to give a shape.	Easy to treat for not being harder and stiff.
3. Cost effectivity	Due to its availability, it is a cost-effective micromodel.	Highly expensive due to its mechanical, thermal, and chemical properties.	An inexpensive micromodel can be prepared from this material.
4. Withstand high load	Effortlessly can maintain its original shape and handle high load.	It can sustain under high load.	Cannot handle high load.
5. React with the sample	Never interact with the sample.	Good chemical resistance.	PMMA has better chemical resistance than PDMS
6. Recyclable	Can be reused after proper cleaning.	Reusable	Can be reused after cleaning.
7. Fragile	Highly fragile.	A silicon wafer breaks easily when not handled with care.	Fragile at moderate load
8. Wettability treatment	Wettability can easily be altered.	Silicon surface possesses easy wettability alteration.	Easy to treat the wettability.
9. Withstand pressure high	High pressure resistant.	Extremely high pressure may cause a breakdown.	Not stable under high pressure.
10. Withstand temperature high	After 540°C it will start melting.	Most convenient under high temperatures (up to 1400°C).	Cannot handle high temperatures.
11. Specific operational conditioned laboratory	Can be made in a conventional laboratory.	Require proper laboratory setup.	PDMS micromodels are very cheap because they can be made in a conventional laboratory.

2.7.3 Micromodel Visualization Methods

Visualization of the pore displacement behaviour is the primary reason why a micromodel experiment is conducted. During the visualization process, one of the challenges has been the difficulty to monitor fluid movement such as the paths followed by each fluid phase, as well as other elements contained in the micromodel (Gaol et al., 2020). The visualization method can change the outcomes significantly because the pore-level understanding of a displacement process is as good as the images produced. An experiment needs to have a good visualization strategy, which is the precursor for both qualitative measures and quantitative analysis of the images captured. From image analysis of the micromodel experiment, the rate of fluids mobilization with respect to time, the phase saturations, and interactions between the fluids and the grain particles or the micromodel surface can be performed. The following section discussed available visualization methods. These methods are the camera-mounted microscope, WIFI microscope, confocal microscopy, fluorescent microscope, and camera-based visualization.

In Table 2.4 different kind of micromodel visualization method has been described with their limitations and suitable features. These are approaches that employ a microscope mounted with a camera, as well as photoluminescent volumetric microscopy, confocal microscopy, and direct camera visualization. The following Table will represent all the parts of the equipment, suitable features, and limitations.

Table 2.4: Different types of micromodel visualization methods

Types of visualization methods	Parts of visualization equipment	Suitable features	Limitations
Camera mounted microscope	One camera, mounting element, one microscope	<ul style="list-style-type: none"> -Very simple setup. -Suitable for visualizing the smallest size of the pore (1-2μm) (Cheng and Giordano, 2002) - This approach is highly recommended for quasistatic (near to static) circumstances (Corapcioglu et al., 2009) - high-resolution visualization at the time of focusing on any particular area (Chen et al., 2007). 	<ul style="list-style-type: none"> - not applicable for prolonged micromodel -Dynamic studies are not possible (Corapcioglu et al., 2009). -the optical window is limited in size. So, no way to record what is going on in a location that is outside the optical window (Cheng and Giordano, 2002). - Dynamic movement of fluid gives low-resolution photos, a lack of time to focus on the movement (Chen et al., 2007).
Camera-based visualization	One camera only, extra objective lens, charge-coupled device sensor, complementary metal-oxide-semiconductor sensor	<ul style="list-style-type: none"> -Simpler setup than a camera mounted microscope setup (Karadimitriou et al., 2012) It is More flexible because can move according to the setup of the micromodel. -can monitor the micromodel from a different angle with multiple cameras at a time which is not possible with the camera-mounted microscope (Chang et al., 2009b). 	<ul style="list-style-type: none"> -less resolution -specific magnification is not possible (Hematpour et al., 2011)
Confocal microscopy	Filters, dichroic mirror, monochromatic light source.	<ul style="list-style-type: none"> -Very precise imaging process - gives better resolution photos than any conventional microscope (Lifton, 2016). 	<ul style="list-style-type: none"> - expensive (Kawelah et al., n.d.) - not efficient for dynamic visualization

		<ul style="list-style-type: none"> - can give a three-dimensional (3D) image(Bazazi et al., 2019) - quasistatic or static conditions required 	<ul style="list-style-type: none"> -has depth limitation. Not effective when depth is more than 250μm (Patel and McGhee, 2013).
Fluorescent microscopy	One Microscope	<ul style="list-style-type: none"> -capable of visualizing microscopic fluidic movement (Fernandez Rivas et al., 2008) -can measure the instantaneous velocity of the experimental fluid (Gaol et al., 2020) -capable of generating two-dimensional images. - allows for the separation of fluid phases during flow (Kim et al., 2011) - practical as it's simple and low on the detection threshold (Kim et al., 2011) - not sensitive to light scattering - timesaving 	<ul style="list-style-type: none"> - sensitive to autofluorescence (Lichtman and Conchello, 2005) - three-dimensional imaging is not possible (Chapman et al., 2013). -expensive -has technical complexity - affected by the variations in P_H and oxygen level - the fluorophore is only viable for a brief period (Chapman et al., 2013).

2.7.4 Recent micromodel application

Fluid flow and solid-solid interactions on both macro and pore scales are typically depicted in geological porous media micromodels. Fundamental factors such as wettability, mobility ratios, and the dynamic contact angle can be assessed using a micromodel. In the presence of fluids, the micromodel can explain the rock's preferences and consequently its transmission capacity. Fluid surface, fluid-solid interaction, and fluid channeling can all be visualized using a micromodel, which can be used in both static and dynamic circumstances. Many geosystems engineering events, such as enhanced oil recovery, can get benefit from these applications.

2.7.4.1 Phase Saturation Calculation

A significant difficulty in progress in this field is the ability to quantify the particular interfacial area. However, now it's possible due to the advancement in the micromodel field. A micromodel can facilitate the visualization of a two-phase fluid flow network during the quasi-static drainage and imbibition process. In situ visualization using high-speed cameras is a very effective and reliable technology for determining and confirming glass micromodel saturation and gradients (Cheng and Giordano, 2002; Cheng et al., 2004). The ability to view and understand the flow process in the porous material is also available (Crandall et al., 2010).

In the recent decade, digital image processing has become increasingly important in a variety of scientific and industrial domains. Digital images are created by directly converting the visual information perceived by a camera (sensor) to a computer-readable data file that can then be analyzed using existing computational tools. Recent breakthroughs in digital imaging technology that enable the collection of higher resolution images, together with continued advancements in image-based computer languages, have broadened the applicability of digital image processing to diverse study areas. To measure capillary pressure and interfacial area, image processing has been used previously. As well, the link between capillary pressure, interfacial area, and phase saturation can be determined from it. One value exists for the particular interfacial area, for each set of capillary pressure and saturation data points (Crandall et al., 2010). Unlike qualitative measurements, capillary pressure within the network is no

longer equivalent to the externally applied pressure under specific conditions. As a result, the capillary pressure at each interface was determined using the curvature of the interface (Gutiérrez et al., 2008). Without the use of optical techniques, it was impossible to detect the curvature of the interface in the third direction. The change in the grey colour of the interface can be used to measure the curvature of the interface (Liu et al., 2011).

N. K. Karadimitriou et al. (Karadimitriou et al., 2014) has done the first experimental investigation that gives a clear visualization of the importance of the interfacial area as a separate state variable when flow is conducted under transient settings. From which phase saturation can be calculated easily using image processing (i.e., MATLAB). In addition, the following additional variables were also established: interfacial velocity, material coefficients, and interfacial production rate. The model was constructed utilizing elongated PDMS micromodel as the theory of drainage and imbibition under quasi-static and transient flow circumstances stated previously was examined.

Mahmoodi et al. (Mahmoodi et al., 2018a) described how micromodel devices examine fluid flow and give a way to monitor fluid transport mechanisms to study what factors affect it. The experimental design yields a picture or series of images (as part of a visualization process) that were used for quantitative image processing to calculate, for example, fluid saturation and other morphological properties. The use of several programming languages' automated image-based computational techniques permits the measurement of micromodel experiments' outcomes more precisely (Karadimitriou and Hassanizadeh, 2012).

The primary concern with such measurements is the precision at the time of determining phase pressures or phase saturation. The determination of phase saturation is generally quantifiable and is dependent on the resolution of the viewing setup. However, measuring phase pressure is very difficult. It is almost difficult to quantify local pressure inside a micromodel, much more so in complicated flow networks with very narrow dimensions. It is essential to do post-processing to extract and compute the average value for a certain geographical region.

2.7.4.2 *Relative Permeability*

A balance between the microscale flow dynamics and the macroscale behaviour of porous media flow is found using the effective two-phase flow coefficients of porous media, such as the capillary pressure and relative permeability functions. Under different experimental conditions, it is necessary to study the relative permeability of each phase as a function of saturation.

Tsakiroglou et al. (Tsakiroglou et al., 2007) used a glass-etched micromodel (filled with the wetting phase) for their measurements (distilled water with methylene blue). Paraffin oil was then pumped into the network using a syringe pump at a pre-set flow rate. Previous photos of the network displacement were obtained using a charged-coupled device (CCD) camera, which took several shots sequentially from a central location. In this center part of the network, differential pressure transducers were used to measure the pressure drop over time. Using this method, the saturation and relative permeability of each phase were determined as a function of time.

With the pressure head difference between the wetting and non-wetting phases, 2009 Chang et al. computed relative permeability. To test drainage, a micromodel with the non-wetting phase added was filled with the wetting phase and the flow rate was monitored. This was until the state of constant flow was achieved. Micromodel images were shot with a CCD camera (Chang et al., 2009a).

Khajepour et al. (Khajepour et al., 2014) worked to verify wettability modification, so a microbial-treated model was tested under identical conditions to see whether the permeability changed or not. Steady-state or unsteady-state measurements were used to measure the relative permeability data concerning fluid saturation. The steady-state technique was shown to be appropriate for assessing relative permeability in the micromodel system when using unsteady-state methods. Brine and oil ratios were concurrently introduced into the model to create a steady-state condition of pressure and saturation. Water saturation was measured using image processing techniques to detect a decrease in water pressure through the porous medium. relative permeabilities were determined by using Darcy's law, which applies to multiphase extensions.

Mejia et al. (Mejia et al., 2020) injected deionized water into the model, and flow was measured as a function of flow rate. Once the injection rate was stabilized, it remained stable for nearly 100 seconds. Flow rates achieved steady-state spontaneously, and at larger flow rates. For a linear permeability calculation, time-averaged pressure decreases of 300 – 400 s were utilized to plot steady-state pressures vs flow rate, and linear regression was used using Darcy's law. Moreover, a permeability of 10-12 D is required to reach an etching depth of 15 μm . The permeability of this reservoir sandstone is greater than most reservoir sandstones. Reducing the permeability to a lesser degree can be done by etching deeper.

2.7.4.3 Fluid-Solid Interaction

There is an essential microscopic characteristic that may be assessed at the pore size, known as the "wetting state" of a porous material. Wettability is the ability of one fluid to spread over or stick to, a solid surface in the presence of other immiscible fluids. Wettability describes the fluid and solid phases' interaction. When reservoirs are treated with fluid, the "fluid" phase may be water, oil, or gas, while the "solid" phase is the minerals of the rocks. Wettability is characterized by the angle of the fluid when it comes into contact with the solid phase (Bear, 2013).

Despite numerous and recent advances in the measurement of contact angles in reservoir rocks using pore-scale imaging, these measurements are not routine and frequently require a detailed level of characterization such as pore geometry, flow direction, and mineralogy on a pore-by-pore (or even sub-pore) basis (Crain, 2002). As a result, macroscopic measures of capillary pressures are increasingly often used to determine the wettability of reservoir rock. Since capillary pressure is not always linked to contact angle (wettability), measuring wettability through capillary pressures is a bit uncertain (Jarrahian et al., 2012). The Amott and USBM indices are two commonly used volume-averaged methods for measuring wettability through capillary pressure measurements. These techniques describe wettability using displacement processes associated with imbibition and drainage (water flooding and oil re-injection cycles) in reservoir rocks or micro models (Blunt, 2017); (Chiquet et al., 2007).

Micromodel has become more popular since its effectivity for detailed viewing of rock/fluid interactions. Additional modelling capabilities include micromodels, which are also useful for generating permeability curves, residual oil saturation, flow characteristics such as flow mobility and wetting behaviour, and permeability-related efficiency. Wettability is the state in which a solid want to contact a fluid (liquid or gas). While permeability, electrical characteristics, nuclear magnetic resonance relaxation durations, and saturation profiles in a reservoir all vary according to a reservoir's parameters, this factor is particularly significant for determining permeability. For accurately monitoring fluid wettability changes, a micromodel with a matching material must be selected. The contact angle, which is the angle between the fluid-fluid interface and the solid surface, is often used to quantify the wettability (Cao et al., 2019).

2.7.4.4 Enhanced Oil Recovery

EOR is a variety of techniques used to increase the amount of oil that can be recovered. Moreover, chemical species in porous media are either carried via the EOR process or remain at the location of production. The technology is used to measure how well various pore-scale chemical or thermal recovery procedures are working. One of the most frequent methods is the injection of gases and chemicals, such as polymers and foams, into the reservoir. The effectiveness of these methods is dependent on the physical characteristics of each phase, viscosity ratios, capillary number, temperature, reservoir conditions, and the flow dynamics of the fluids being used.

Cheraghian et al. (Cheraghian, 2015) discussed that one-third of the original oil remains unrecoverable when using conventional production methods. Adding surfactants and polymers, however, enables another third of the original oil to be recovered. The rise in oil prices, in addition to increased oil output, has driven a resurgence of interest in chemical flooding. This study aimed to find out whether using nano-clay would increase the effectiveness of a certain surfactant polymer flooding technique in five-spot glass micro-models. Using horizontal glass micromodels, the effect of different injection amounts of different solvents on the dissolution of glaze-bonded glasses was investigated. The recovery curve slope rose in the presence of nanoparticles, leading to an increase in ultimate oil recovery. The results of the tests revealed

that increasing heavy oil recovery in the nano-model with nano-clay produced an increase in the efficiency of extraction (60.6 percent).

Li et al. (Li and Torsæter, 2014) used a micromodel to examine the effect of combining silica nano-structured particles and colloidal silica nanoparticles on oil recovery, researchers used both in this experiment. The micromodel was transparent and made out of glass. Nanoparticles were dispersed in synthetic brine to make a solution. To find out how nanoparticles affect EOR, the various types of nanoparticles and concentrations, as well as how nanoparticles affect the characteristics of oil and water, were examined. According to the findings, nanoparticles can decrease the interfacial tension between oil and water, and contact angle, making solid surfaces moister. Increasing the nanoparticle concentration further results in trapped oil production through emulsification and IFT decrease. When adsorbed nanoparticles block pores, injection pressure increases, which causes trapped oil to be forced out of the model through the pore channels. The glass micromodel study's findings demonstrate that nanoparticle fluid extraction capability is considerable.

Amirian et al. (Amirian et al., 2017) studied the low salinity water flooding (LSWF) dynamics, two-dimensional glass micromodels covered with either clean or clay were employed. A wettability setting of both water-wet and oil-wet conditions was also established. When considering the movement of pore-scale elements (i.e., particles no larger than a pore), displacement processes were investigated using either clay-dominated two-phase flow or drainage-dominated flow. To understand LSW inhibited “snap-off” in water-wet systems, it is important to recognize the role played by water-oil interfaces in these systems. The tendency for oil-wet systems to have higher wettability was found. a comprehensive discussion of the electrical double layer (EDL) expansion is given. These observations had shown that fines migration had a significant impact on enhanced oil recovery.

Mahmoodi et al. (Mahmoodi et al., 2018a) observed fluid transport processes and characterized affecting variables at the microfluidic level that may lead to a better understanding of multi-phase fluid flow mechanics. In addition to image processing, the variable of interest was quantified in a micromodel experiment by analyzing fluid saturation and other morphological characteristics. Using several programming languages, they were able to use automated image-based computational techniques to improve the outcomes of

micromodel tests. Image processing code was used to illustrate the feasibility of automating image processing capabilities available in LabVIEW. This proprietary method is checked against carbonated water injection micromodel experiment data using estimates of absolute values from the volumetric material balance as reference. By searching the possible settings for functions in LabVIEW, optimal settings for those functions that match true values are discovered. This last part compares the results of the algorithm in LabVIEW with the results of another popular commercial program to illustrate the benefits and drawbacks.

Also, Khalafi et al. (Khalafi et al., 2018) emphasize pore size research in this work, which seeks to better understand nanoparticle-surfactant flooding as an improved oil recovery method. To investigate the oil recovery processes while using hydrophilic silica nanoparticles, five tests using five-spot glass micromodels were performed with the addition of different quantities of silica nanoparticles. During the injection procedure, macroscopic oil recovery and pore fluid distributions were studied by continuous imaging of the micro model while the fluid was being injected. Oil recovery increases significantly when nanoparticles are included in the injected fluid. Nanoparticles may greatly enhance the oil recovery that is achieved by flooding the oil field with water and using surfactants. While the surfactant solution marginally thinned the oil layer on the pore walls, nanoparticles eliminated it and made the oil wet.

A microfluidic sand pack model was utilized by Liu et al. (Liu et al., 2019) at their research, to examine emulsion propagation in both the pore and macro sizes, as well as plugging processes at both the pore and macro scales. A microfluidic chip was constructed to replicate a heterogeneous area, comprising regions with differing permeability. To study the impact of pore structure on residual oil displacement following surfactant/polymer (SP) flooding, two different emulsion-based displacement tests were carried out using identical emulsion slug samples. These findings indicate that in-situ emulsion formation may be critical to enhancing oil recovery in reservoirs with convoluted pore structures, but that this is unlikely to be the case in reservoirs with wide pore throat channels.

Micromodel applications ease the way to determine the parameters with a degree of accuracy. Fluid saturation, permeability, area, fluid-fluid interaction, fluid-solid interaction, and recovery measurement has been practiced for so many years.

2.8 Summary

In low salinity water alternating CO₂ gas flooding fluid-fluid interaction and fluid-rock interaction, measurement facilitates the proper visualization of wettability alteration and spreading coefficient measurement. It has been shown that the increase in fluid movement inside the system helps to enhance recovery. This residual oil recovery depends on wettability and spreading coefficient. Based on this literature, it can be said that this part of the investigation has not been investigated deeply to date which will provide the proper idea behind it and this thesis will focus on this gap. According to the literature reviews, a system with water wet and a positive spreading coefficient creates a continuous thin oil film flow that accelerates the amount of oil flow as well as recovery. Whereas a little amount of work has been conducted under reservoir conditions which is another gap in this field and an elaborated work has been conducted to overcome this gap in this project.

CHAPTER 3

RESEARCH METHODOLOGY

3.1 Introduction

The main objective of this study is to investigate the effect of wettability and spreading coefficient in LSWAG CO₂. Figure 3.1 illustrates the step-by-step procedure of the experimental methodology. Firstly, in this study, crude oil collection, LSW (brine) preparation and micromodel design has been counted as the most important of all to accelerate this work. Measure the contact angle and interfacial tension have been conducted by an instrument named IFT700. IFT V4.1.0 software has been employed in this experiment to take all photos during the experiment. We conducted wettability measurement by using the value of the contact angle and the spreading coefficient also measured from interfacial tension values. Brine, CO₂, and crude oil have been injected into the manufactured micromodel with HPHT micromodel rig equipment and software has captured all the photos during the experiment. Following this, fluid flow distribution, a fluid movement for a different condition has been visualized and the effect of wettability alteration, spreading coefficient in low salinity water alternating CO₂ gas has been investigated. All the experiments were conducted at high temperatures and pressure to visualize the entire effect in reservoir conditions. Temperature, density, and composition are some of the most fundamental principles of fluid properties. Extensive properties are mass and volume that depends on the amount of material. Along with that, intensive properties are density, temperature, and pressure. Interfacial tension and contact angle are the two most important properties of the fluid.

From Figure 3.1, the overall flowchart is representing the steps to obtaining three individual objectives of this thesis. To obtain the first objective, interfacial tension measurement experiments in various conditions have been carried out to calculate the spreading coefficient for different fluids and its effect on LSWAG-EOR. Contact angle experiments have been conducted to obtain proper observation regarding wettability alteration and the effect of wettability during LSWAG- EOR as well as the second objective. Finally, the third objective

has been accomplished by micromodel experiments to understand the pore-scale effect of wettability and spreading coefficient on fluid movement and distribution as well as recovery.

In this chapter, sample, and reagents, micromodel design and wetting properties alteration procedure, wettability measurement, spreading coefficient measurement, interfacial tension experimental design, RSM and ANOVA analysis has been presented according to the experimental requirement.

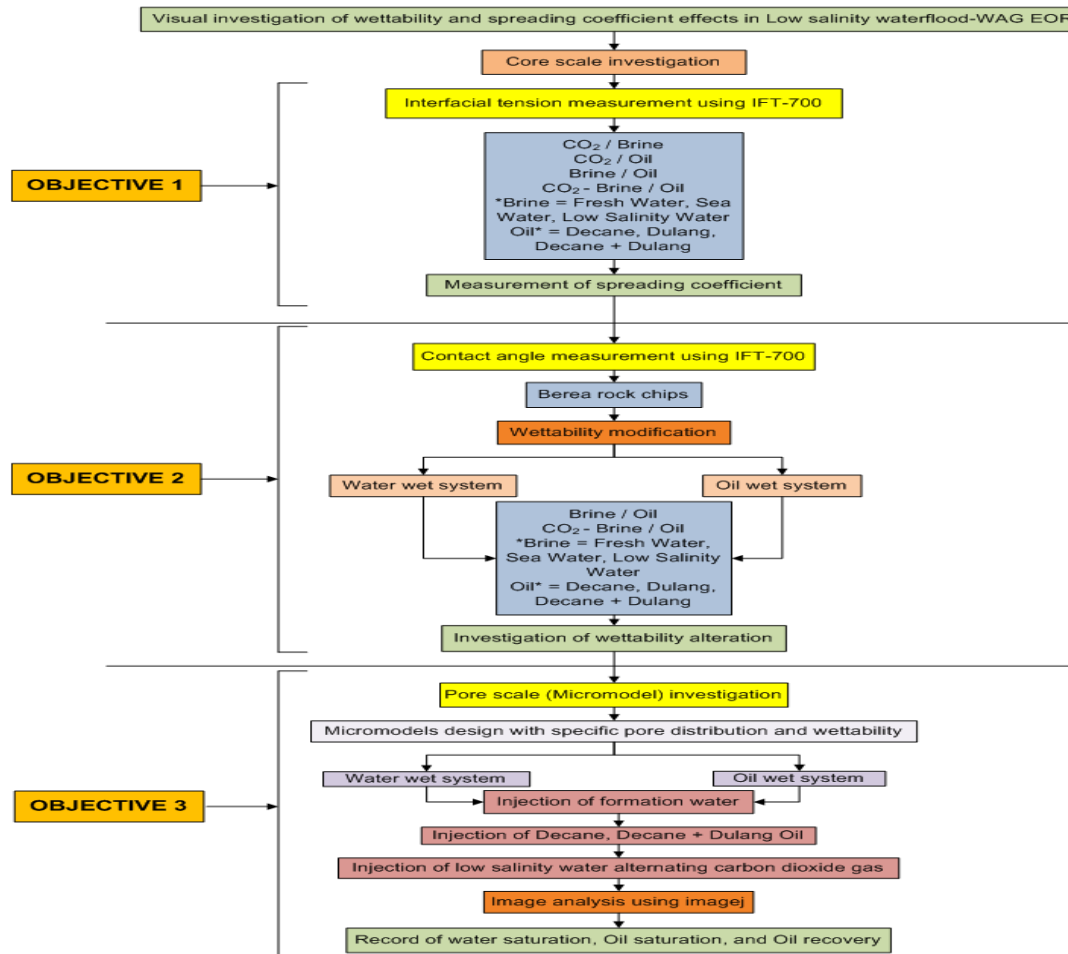


Figure 3.1: Overall flowchart of experimental methodology

3.2 Samples and Reagents

In this section, all the samples and reagents used for each experiment have been discussed in detail. Crude sample analysis, brine sample preparation process, core sample preparation, and micromodel design procedures have been discussed thoroughly. Moreover, HPHT micromodel experimental sequence has been presented with a flow diagram.

3.2.1 Crude sample

The crude oil used in this work was Dulang from a matured Malaysian basin with a Viscosity of (at 96°C) 0.625 cp, Pour Point 40°C and it is a waxy crude oil. Dulang Field Reservoir and Fluid Properties are presented below in Table 3.1 and in table 3.2 the fluid properties of Decane oil have been presented. Also, from the experimental data, the density of 20% Dulang and 80% Decane mixture is 0.715972 gm/cc at 2000 psi pressure and 96°C temperatures.

Table 3.1: Dulang Field Reservoir and Fluid Properties (Abd Shukor, 2014)

Reservoir and Fluid properties	Value
Average Water Saturation	39%
Average Permeability	200 Md
Average Porosity	30%
Initial Reservoir Pressure	1800 psig
Reservoir Temperature	96°C
Bubble Point Pressure	1,600 psig
Oil Viscosity (at 96°C)	0.625 cp
Oil Pour Point	40°C
Gas Viscosity	0.016 cp
Oil Stock Tank Density	0.8347 gm/cc
API	37.4°API
Solution Gas-Oil Ratio	400 scf/stb
Oil Formation Volume Factor	1.279 rb/stb

Table 3.2: Decane Fluid Properties (Linstrom and Mallard, 2001)

Reservoir and Fluid properties	Value
Critical temperature (T_c)	344.6 °C
Critical pressure (P_c)	305.01 psia
Critical density (D_c)	0.233 g/cc
Normal boiling point	174.12 °C
Density @ 2000psi	0.68629 gm/cc
Viscosity	0.359 cp @100°C

3.2.2 Brine sample preparation

In this work, Formation brine (FB), High salinity seawater (HSS), 2 times diluted seawater (LS1), 5 times diluted seawater (LS2), 10 times diluted seawater (LS3), 20 times diluted seawater (LS4), 50 times diluted seawater (LS5) were prepared with an estimated amount of salt (using electronic balance) based on composition on Table 3.4 and mixed with distilled water using a magnetic stirrer for 30 minutes each. As per the selected concentration, the concentrations ranged from 722-36080 ppm. This is shown in Table 3.3 below.

Table 3.3: Salinity of the brine samples

NO.	Brine Sample	Salinity (ppm)	
1	Formation Brine	FB	21400
2	High Salinity Seawater	HS	36080
3	0.5HS (x2)	LS1	18040
4	0.2HS (x5)	LS2	7214
5	0.1HS (x10)	LS3	3607
6	0.05HS (x20)	LS4	1804
7	0.02HS (x50)	LS5	722

Note: x2, x5...refers to the dilution factor

Brine sample which includes formation and seawater brine taken from the field. A total of 7 samples with varying salinities have been prepared and used to achieve the objectives of this study. In the following Table, 3.4 compositions of different salinity brine have been presented.

Table 3.4: Brine compositions

Salt	Weight (g)				
	LS1	LS2	LS3	LS4	LS5
CaCl ₂ .2H ₂ O	0.416	0.166	0.083	0.042	0.017
MgCl ₂ .6H ₂ O	5.136	2.055	1.027	0.514	0.205
SrCl ₂ .6H ₂ O	0.005	0.002	0.001	0.001	0.000
NaCl	11.85	4.744	2.372	1.186	0.474
Na ₂ SO ₄	0.192	0.077	0.038	0.019	0.008
KCl	0.312	0.125	0.062	0.031	0.012
NaHCO ₃	0.110	0.044	0.022	0.011	0.004

3.2.3 Core sample preparation

In the last 30 years, the petroleum industry has generally recognized the performance of Berea sandstone in testing chemical surfactants. Berea Sandstone is a primarily sand-sized sedimentary rock. It consists primarily of silica-linked quartz powder. The core of the samples typically has a high porosity and permeability, which makes them good reservoir rock. To conduct the contact angle experiment, we used Berea rock chips with 11% porosity. To cut the core sample into thin slices, the core slices trimming apparatus was employed. Seventy-two Berea core slices were prepared to determine the contact angle between the fluid/solid phase using sessile drop orientation. Several steps of polishing was employed to obtain the smooth surface for each core slice. Formation water, seawater, five types of low salinity water, and decane, Dulang, and Dulang+Decane oil has been used at the time of contact angle measurement.



Figure 3.2: Cleaned core placed in the oven to be dried

Moreover, to visualize the wettability alteration of each experiment under different wetting conditions, the wettability of core slices has been changed with a systematic procedure. The procedure has been described below-

The core plug has been washed and dried under ambient conditions for a specific number of days after they have been cut. After cutting the slices, proper polishing is required as it enhances the possibility of measuring the contact angle correctly. After polishing core slices, it has been washed using toluene, acetone, and distilled water. Then undergone oven-dried at a specific temperature for several days as Figure 3.2. For oil-wet rock samples, the samples have been aged sufficiently in crude oil for thirty (30) days but low permeable rocks (below 100 mD) with high clay content will require about sixty (60) days of aging at ambient temperature to note its effect on contact angle measurements. For water wet, samples have been saturated for several days within the prepared brine at a stable temperature.

3.3 Micromodel Design and Wetting Properties Alteration

Micromodel pattern design and etching have been considered very important steps during manufacturing a micromodel. In this work, we used the following pattern for the micromodel. Figures 3.3, 3.4, and 3.5 are representing the steps to design the micromodel pattern as well as manufacturing it.

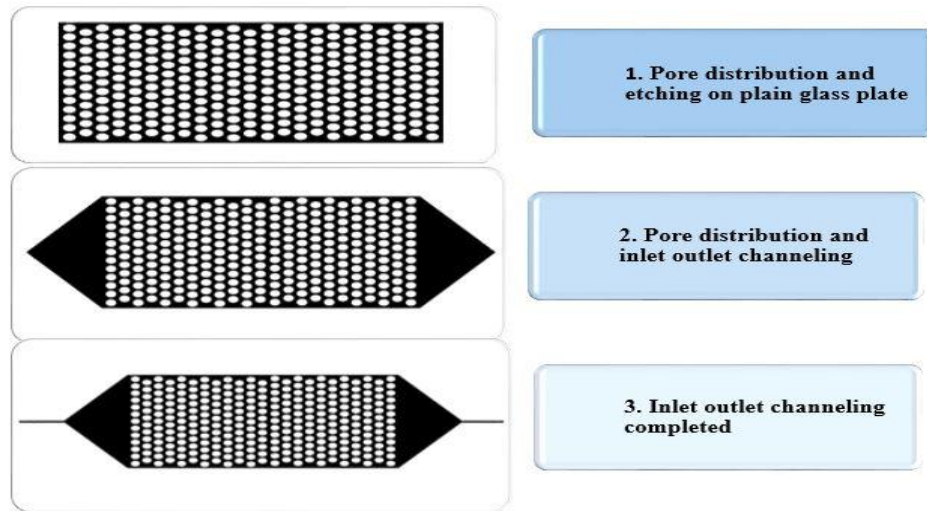


Figure 3.3: General steps to design a micromodel

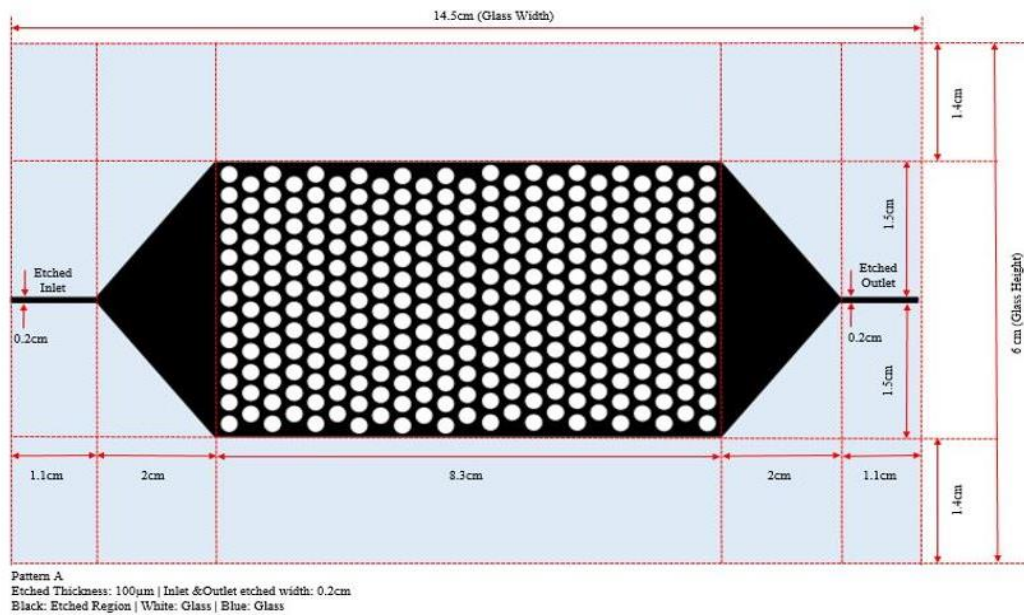


Figure 3.4: Final design with size specification

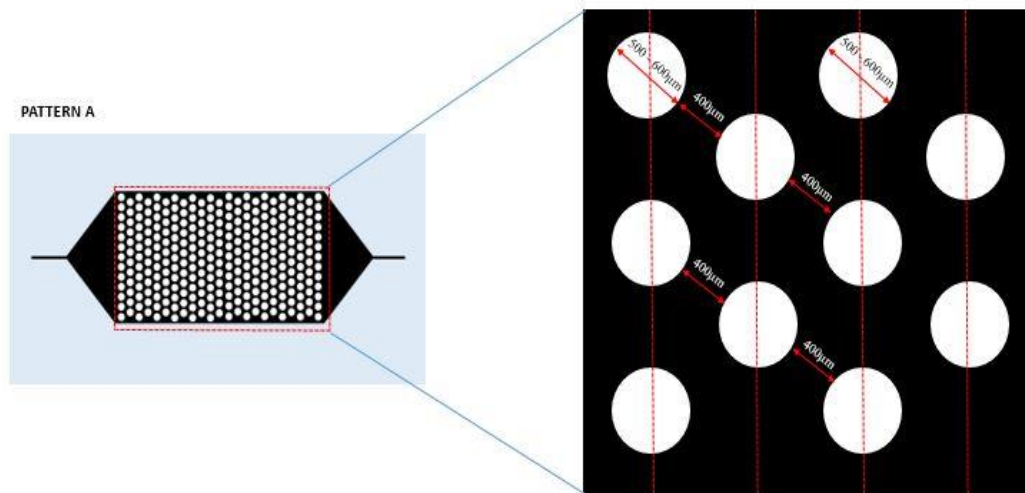


Figure 3.5: Zoom view of micromodel pore size and distance between pores

Micromodel height, width, and length are 0.01 cm, 3.2 cm, and 8.3 cm accordingly. Height of the micromodel is considered the height of a pore. Table 3.5 shows a calculation of the total pore volume and porosity of this glass micromodel.

Table 3.5: Determination of total pore and porosity

Total volume of the micromodel	Total grain volume	Total pore volume	Porosity
Length * Width * Height = (8.3*3.2*.01) = 0.2656 cm³	Total grain = 3410 Grain area = πr^2 = 3.1416*(.03) ² = 0.002826 cm ² Total grain area = (0.002826*3410) = 9.63666 cm ² Total grain volume = (9.63666*0.01) = 0.0963666 cm³	Total volume- Total grain volume = (0.2656-0.096366) = 0.169234 cm³	(Total pore volume / total volume) * 100% = (0.169234/0.2656) * 100% = 0.6371 * 100% = 63.71%

To alter the wetting properties of glass micromodel several steps have been conducted. Water wet and oil-wet wetting properties can be achieved in many ways (Gogoi and Gogoi, 2019; Meybodi et al., 2011). In this work, the following steps are followed to alter the wettability of glass micromodel to water-wet and oil-wet state.

Water wet- initially cleaned it with toluene and left it like this to soak it in the glass micromodel surface. After 15 minutes, cleaned it with acetone and vacuumed it to make sure that the micromodel is cleaned and there is no solution left inside it. In the next step, distilled water and hydrochloric acid have been injected. After this step, placed those micromodels inside the oven at 100°C temperatures for 2hours to set them on the glass surface. Thus, water wet micromodel has been prepared already.

Oil wet- Sodium hydroxide has been injected into the micromodel and after 15 minutes 0.5% of Di chloromethyl silane (DCMS) has been injected. Again after 20 minutes, when all the silane is already soaked by the glass micromodel surface then dehydrated toluene and methanol have been employed. To set all these chemicals on the micromodel surface to alter it to oil-wet, the micromodel has been placed inside the oven at 100°C for 6hours. Finally, the micromodel has been prepared as an oil-wet micromodel.

3.4 Interfacial Tension Measurement

At a constant temperature of 96°C, the interfacial tension (IFT) between the oil and water phases was estimated and observed. In all IFT measurements, the low salinity water was previously prepared, and the oil phase was Dulang, decane, and Dulang+Decane. IFT 700 has been used for interfacial tension measurement. This equipment can measure the interfacial tension between liquid-liquid and gas-liquid under high pressure and high-temperature condition using either the pendant drop or rising drop method (Lun et al., 2012). In the case of this experiment, the IFT was measured at reservoir temperature and pressure (ranging from 200 psi to 2000 psi). Table 3.6 presents the general experimental design of the IFT experiment.

Table 3.6: General experimental design for IFT experiment

Oil phase	Gas-phase	Water phase	Salinity (ppm)	Pressure (psi)	IFT responses
Decane-Dulang/ n-decane/Dulang	CO ₂ /with out CO ₂	Brine	722	200 -2000	
			1804	200- 2000	
			3607	200- 2000	
			7216	200- 2000	
			18040	200- 2000	
			21400	200- 2000	
			36080	200- 2000	

3.5 Spreading Coefficient Measurement

IFT values of Oil/water, gas/water, and oil/gas have been used to determine the spreading coefficient of each phase. The phase spreading ability is simply termed the spreading coefficient S .

$$S = \gamma_{gw} + \gamma_{go} + \gamma_{ow} \quad (3.1)$$

In equation 3.1, γ_{gw} is the gas-water surface tension, γ_{go} is the gas-oil surface tension, and γ_{ow} is the oil-water interfacial tension. If the value of S is positive the oil can disperse in the presence of the gas phase on the water substrate as a thin film, this oil film supports the hydraulic conductivity of the oleic phase contributing to higher oil recovery and therefore low residual oil saturation. On the other side, if S is negative, an immobile oil lens (snap-off) will be formed in the water-developed phase; this ensures that the water will flow and bypass the oil and result in a higher residual oil saturation at the end (Oren and Pinczewski, 1994).

3.6 Contact Angle Measurement

At a constant temperature of 96°C, the contact angle between the fluid-solid phases was estimated and observed. Berea rock slices have been used here as the solid phase. In all contact angle measurements, the low salinity water was previously prepared. The heavy phase was Dulang, Decane+Dulang, and decane which defines the oil phase in the reservoir. IFT 700 was used for this section of the experiment. This equipment can measure the contact angle between liquid-solid surface high-temperature conditions using the pendant drop and rising drop method (Lun et al., 2012). In the case of this experiment, the contact angle was measured at reservoir temperature conditions 96°C and high pressure (ranging from 200 psi to 2000 psi). Table 3.8 presents the general experimental design of the contact angle experiment. Moreover, Wettability alteration can be observed by the results from contact angle (Dong et al., 2007)(Liu and Wang, 2020).

In three ways wettability can be determined: firstly, from the product of the contact angle and the interfacial tension. Secondly, determination of the contact angle (the last term in Young's equation) under the same condition. Thirdly, determination of the relative amount of displaced oil and water. The second method is the most common one while the first one is the most difficult to determine. The third process and findings are most varied. This experiment will use the first method to determine wettability. For this, the value of contact angle and interfacial tension is needed to determine wettability if anyone uses the first method.

Table 3.7: General experimental setup of contact angle experiment

Oil phase	Gas-phase	Water phase	Salinity (ppm)	Pressure (psi) *(with 200 psi interval)	Contact angle responses (R1, R2, R3)
Dulang+	CO ₂ /with out CO ₂	Brine	722	200 -2000	
Decane/			1804	200- 2000	
n-			3607	200- 2000	
decane/D			7216	200- 2000	
ulang			18040	200- 2000	
			21400	200- 2000	
	36080	200- 2000			

3.7 Experimental Design and ANOVA Analysis

Response surface methodology (RSM) can optimize the response and predict future responses reliably by statistically calculating a regression model based on enough experimental data (Sahu et al., 2009). The RSM reduces the number of tests, which saves time and money in the experimental design process (Khodaii et al., 2016). The response surface model is approximately represented by the experimenter with a model equation, while the behaviour of response variables is modelled as a function of a set of regression variables. When the model is expected satisfactory, it can be used to predict within the experimental region and to determine the operating conditions on the explanatory variables that provide the peak response but if the model is not satisfactory, more tests must be done to enhance the fit or an adjustment must be made in the mathematical form of the model (Shelton et al., 1983). The effect of salinity, pressure, and CO₂ on IFT has been determined from this model. When the model is properly developed, the accuracy of predicted IFT values was identified using ANOVA. The optimized value for oil/water interfacial tension with and without CO₂ was obtained by simultaneously minimizing and maximizing the validated model for IFT. Face-centered composite design (FCCD) is a three-level practical, experimental design in which the axial points are focused on the cubic surface rather than the sphere, and α is equal to 1. The IFT between oil/water has been optimized with the FCCD and the operational correlation between independent factors and the response has been developed (Mtarfi et al., 2017).

In this work design expert version, 11.1.0 has been used to get the experimental design and to generate the model. RSM modelling has many designs and styles. In this work central composite design was used for the design of the experiment (DOE) with CO₂ and without CO₂ gas. Concentration and pressures are the input data and IFT and contact angle are the output of this work. High and low levels were determined for the range of individual variables. The highest and lowest concentration was reported at 36080 ppm and 722 ppm, with the pressure range between 200-2000 psi. The only response was assigned as interfacial tension between the oil/water phase. The experimental design matrix suggested 13 experimental runs for the experiment with CO₂ and 13 runs for the experiment without CO₂ based on the high and low levels for mentioned factors in RSM. To analyze, develop, and enhance the model parameters, the responses from the experiments were inserted into the corresponding response slots.

The statistical parameters and synergistic effects of every factor were evaluated using ANOVA. For the regression model, various suitability tests for ANOVA (lack-of-fit assessment, F-value, p-value) are recommended. Based on the agreement between the expected and observed responses, a statistical analysis using ANOVA was used to determine the degree of relevance for the chosen model Design Expert also provided 3D model graphs focused on the correlation of design variables, following the fitting of a suitable model.

After using Design expert software, a Design of experiment (DOE) for Interfacial tension between oil/water, gas/water, and gas/oil interface with CO₂ and without CO₂ has been proposed by the software. Table 3.9 and Table 3.10 is representing the actual DOE for interfacial tension and contact angle prepared by the software which we used as the design of our experimental procedure.

Table 3.8: Actual DOE for IFT (Decane/water)

Run	A: concentration (ppm)	B: Pressure (psi)	Bulk Density	Drop Density	Response 1 IFT (mN/m)	Response 2 IFT (mN/m)	Response 3 IFT (mN/m)	Average (IFT) (mN/m)
1	722	200	.9621	.67232				
2	722	1100	.96495	.67859				
3	722	2000	.9678	.68629				
4	18401	200	.9696	.67232				
5	18401	1100	.9724	.6796				
6	18401	2000	.9752	.6871				
7	36080	200	.9776	.67232				
8	36080	1100	.98015	.67859				
9	36080	2000	.9834	.6863				

Table 3.9: Actual DOE for contact angle

Run	Factor 1	Factor 2	Response 1	Response 2	Response 3
	A: concentration	B: pressure	R1	R2	R3
	(ppm)	(psi)			
1	722	200			
2	722	1100			
3	722	2000			
4	18401	200			
5	18401	1100			
6	18401	2000			
7	36080	200			
8	36080	1100			
9	36080	2000			

3.8 HPHT Micromodel for Pore Scale Visualization

In HPHT micromodel test rig equipment, the system includes a micromodel casing, accumulator for oil, water, and gas, back pressure regulator, HP syringe pump, ISCO pump, and InduSoft software. In this experiment, the micromodel casing helped to protect the glass micromodel as well as provide a safe workplace for the person who worked with this equipment. The accumulator for oil, water, and gas secured the fluid to sip and elevate the pressure inside the accumulator as well the entire system. An unwanted leakage in the accumulator could create sudden difficulties to run the experiment under high pressure. The back pressure regulator creates a pressure so that fluid cannot come through the outlet and accumulates in the outlet pipeline which will help to increase the outlet pressure as well as inlet pressure. There is a high-pressure syringe (HP syringe) to maintain the confined pressure inside the system. An ISCO pump has been used to supply continuous water to the fluid accumulator to pressurize the internal fluid to move towards the micromodel. An ISCO pump delivers accurate, repeatable flows of virtually any fluid. This pump is used for core flooding or micromodel rig system for the uninterrupted experiment. Also, Indusoft software has been used to operate the experimental, temperature, flow rate, valves, pump set, the pump fills up, and casing fills up. This software recorded all the pressure, flow rate, and pressure difference data every 10 seconds which has been used for further calculation. In Figure 3.6 experimental sequence for pore-scale investigation and evaluation has been presented in a flow chart.

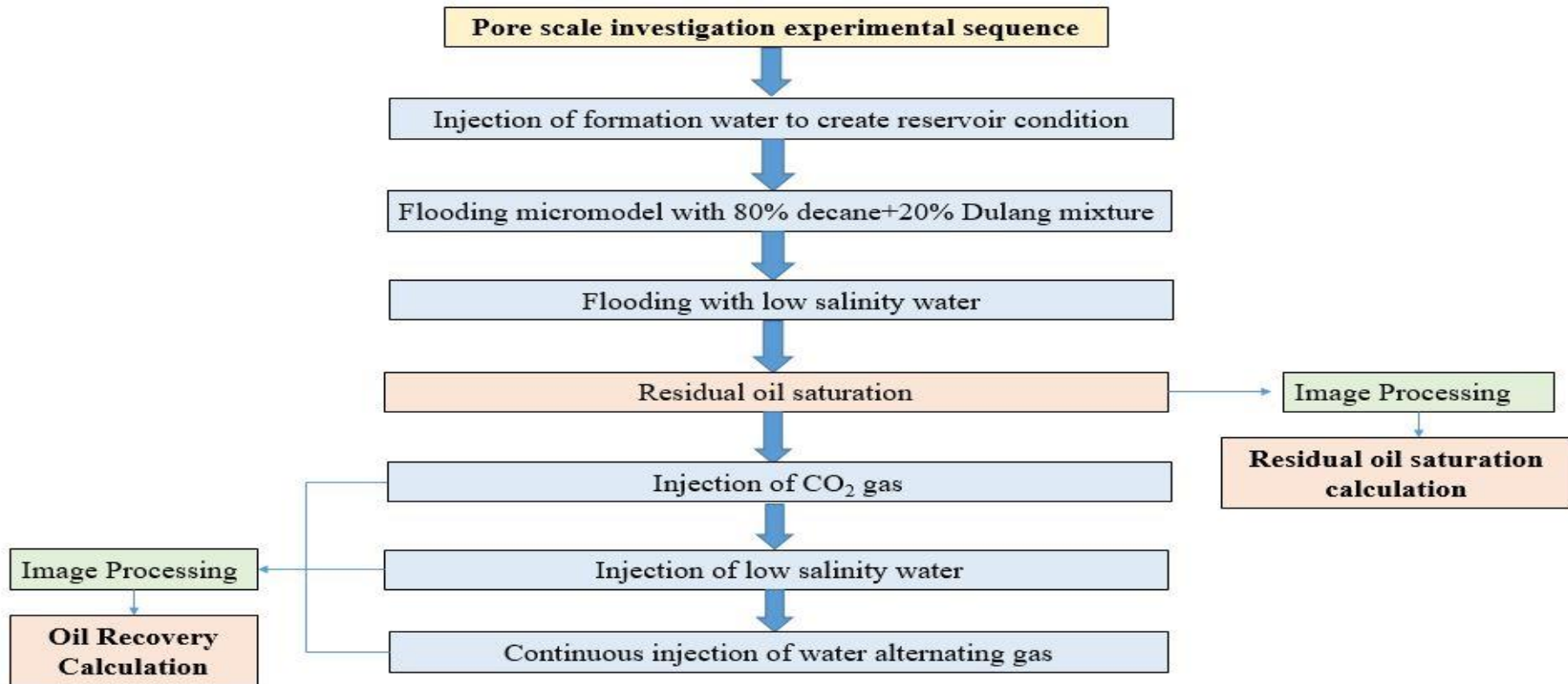


Figure 3.6: Experimental sequence for pore-scale investigation and evaluation

During this work, an injection sequence has been followed to determine the residual oil saturation and final recovery to differentiate the additional oil recovery for different low salinity water. According to the injection sequence, in this work at first formation water has been injected then flooded with the (80% decane + 20 % Dulang, Decane) oil mixture, after flooding the micromodel with the oil phase low salinity water has been injected to visualize and calculate the residual oil saturation. After that, continuous CO₂ injection happened to move residual oil from the place and this continuous injection of low salinity water alternating gas takes place for a long time to visualize the fluid interaction and oil movement. In this experiment, the system pressure was 500 psi due to a slight problem in the back pressure regulator which can lead to micromodel breakdown and equipment loss and the temperature was 22°C due to the problem with the heater. All photos and videos have been captured after every 10 minutes to visualize the entire situation.

In this work, Dulang+Decane mixture has been used to conduct the pore-scale experiment. Though at room temperature Dulang is a waxy crude oil it is very difficult to run HPHT micromodel experiments with it due to the narrow pipelines of HPHT micromodel equipment. Unfortunately, the heater was not working during the experiment, which is why the Dulang+Decane mixture has been employed to avoid the waxy nature of Dulang.

3.9 Recovery Calculation

After continuous injection of water alternating gas, a wide range of photos has been collected from the experiment to evaluate recovery after several time differences and for different low salinity water using image processing. ImageJ image processing software has been used to evaluate recovery from different photos collected during the experiment. ImageJ is a handy software to operate, available for free, and easy to learn. This software helped to calculate all the images very easily within a very short time with high accuracy. Some pre and post steps have been maintained in this recovery calculation.

1. Install ImageJ software and set the scale

Before beginning image processing, it is critical to determine the appropriate scale. Once the image and reference scale are copied into the software, anyone can then set a specific length to represent the distance in the image. In our pore-scale image, we know the length of each grain. it is 550-600 μm . So, set the unit from pixel to μm and the whole dimension will be changed from pixel to μm . Finally, calculate the length of one grain to make sure that the length is from 550-600 μm . If it is between 550-600 μm then the scale is set up for further steps.

In Figure 3.7, the left picture is indicating the set distance of 600 μm and from the image, we get the length for one grain is 581 μm . So, the value is between 550-600 μm and it is indicating the scale setup is correct.

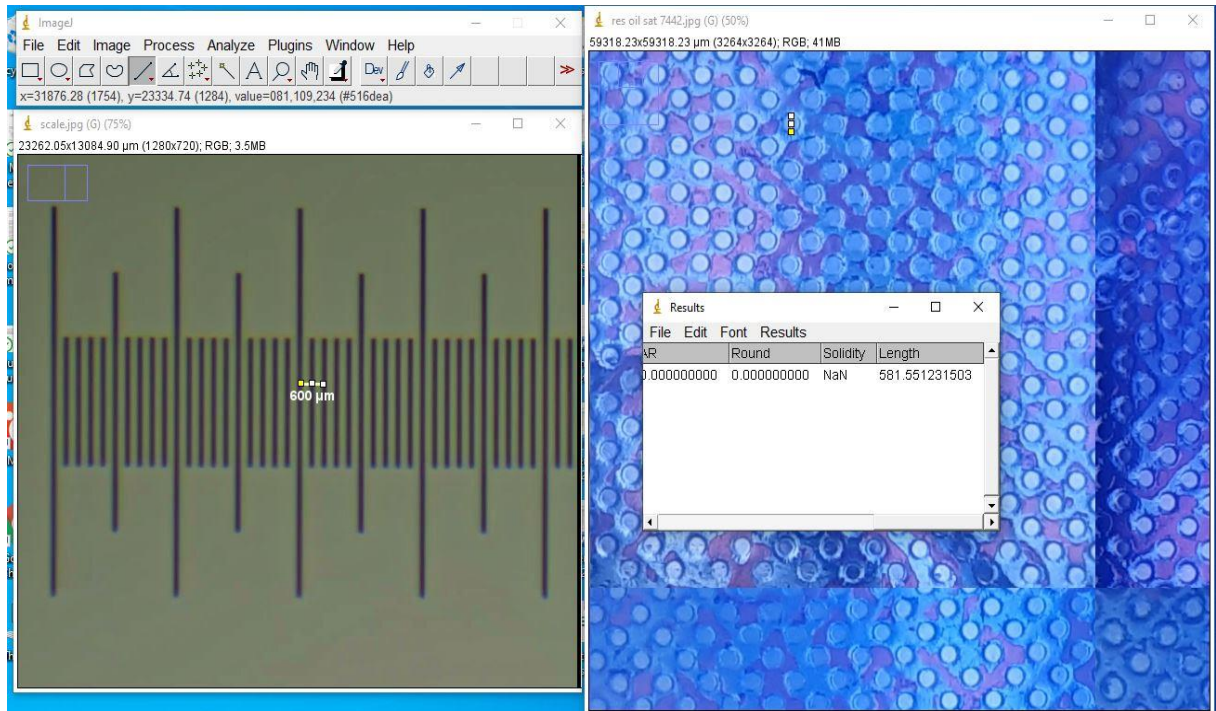


Figure 3.7: Scale setting (oil- red color, brine- blue color)

2. Draw the area and fill

From the image, a specific area with oil has been calculated. For this, change the image type to 8-bit and detect the area with oil. After detecting the area with oil, draw the area without grain and measure the area. After that fill the area already calculated which will help to avoid

repeat calculation of one area. In Figure 3.8 we can see some white areas. These are the area with oil and after calculating each area we fill it with white color for ease of detection.

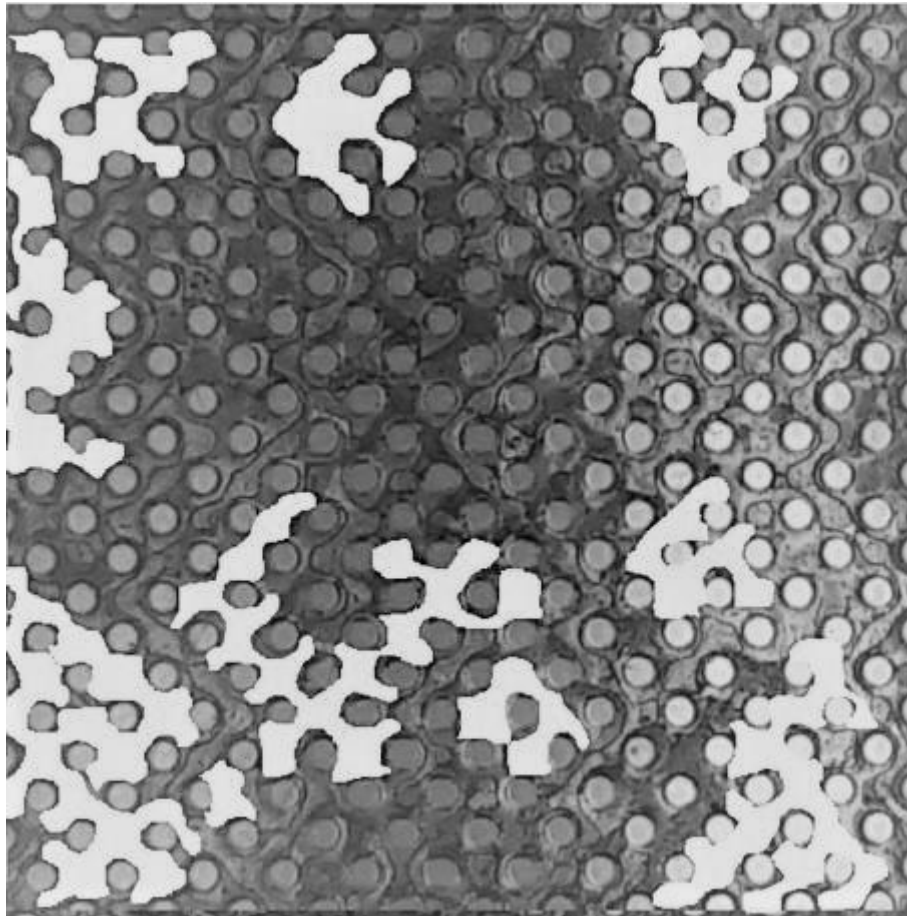


Figure 3.8: Area Calculation and fill

3. Saturation Calculation

The total calculated area of oil from the image analysis has been multiplied by the width of the micromodel to get the volume of total oil. Furthermore, dividing by the actual volume of the micromodel will provide the volume of fluid present in the micromodel, and multiplied by 100 will provide the saturation of specific fluid in the micromodel. For these calculations, we used Microsoft excel.

4. Recovery Calculations

From the saturation calculation, recovery has been calculated and, in this process, we also used Microsoft excel.

3.10 Summary

In this chapter, an in-depth overview of the overall experimental methodology of the current study has been provided. In this study, experiments have been carried out to investigate the pore-scale effect of wettability and spreading coefficient during low salinity water alternating CO₂ gas. These experiments consist of Interfacial tension evaluation, spreading coefficient measurement, contact angle experiment, wettability alteration observation to obtain objective one and two. The effect of CO₂, micromodel porosity. Experimental design and ANOVA analysis with HPHT micromodel operation procedure have been described here with detailed discussion to obtain the third objective.

CHAPTER 4

RESULTS AND DISCUSSIONS

4.1 Introduction

In this chapter, Interfacial tension experimental data analysis, model generation, corresponding graph analysis, spreading coefficient measurement, contact angle measurement, and data analysis have been thoroughly discussed. Additionally, the CO₂ gas effect on spreading coefficient and contact angle has been investigated with detailed analysis. Furthermore, pore-scale investigation of wettability and spreading coefficient effects in low salinity waterflood-WAG EOR has been analyzed using image analysis which has added another dimension to this chapter.

4.2 Interfacial Tension Measurement

This section describes the change in interfacial tension (IFT) due to differences in pressure, brine salinity, and oil. IFT between oil/water, gas/water, and gas/oil phases with CO₂ and without CO₂ will provide a clear idea about the effect of CO₂ on interfacial tension based on experimental data, Response surface methodology (RSM) modeling, and graphs. These experimental studies involved the use of IFT700 equipment in high-temperature and high-pressure conditions. Whereas Design expert software has been used to generate all the RSM models based on the experimental outcome. Later these IFT results have been utilized to measure the values of the spreading coefficient.

4.2.1 Total Samples to Measure IFT

In this study, we have seven different salinity brine, three different oil (Decane, Dulang, Decane+Dulang mixture), and a pressure range from 200-2000 psi. Also, the presence and absence of CO₂ have been considered two experimental conditions to design the DOE of IFT experiments. Based on these conditions and difference in salinity, oil, and pressure, six

different RSM model has been generated to predict any value of interfacial tension for specific pressure and salinity within the range. Table 4.1 is representing the total number of generated models for interfacial tension. From these six models, in this section, only two models (Dulang with CO₂ and Dulang without CO₂) have been described thoroughly, for other models, only the graphs have been discussed to clarify the effect of CO₂, pressure, and salinity on IFT.

Table 4.1: Total RSM models of IFT

No.	With CO ₂			No.	Without CO ₂		
	Salinity	Oil	Pressure		Salinity	Oil	Pressure
1	722	Dulang	200	4	722	Dulang	200
			1100				1100
	18400		2000		18400		2000
	36080				36080		
2	722	Decane	200	5	722	Decane	200
	18400		1100		18400		1100
	36080		2000		36080		2000
3	722	Dulang+Decane	200	6	722	Dulang+Decane	200
	18400		1100		18400		1100
	36080		2000		36080		2000

4.2.2 RSM Model for Brine/Dulang IFT with CO₂

After obtaining data from the experimental run with CO₂ according to the suggested DOE were added in the predetermined slots for the response as shown in Table 4.2.

Table 4.2: Actual design matrix for Brine/Dulang IFT

	Factor 1	Factor 2	Response 1
Run A:	Concentration	B: pressure	IFT
	Ppm	psi	mN/m
1	722	200	18.99
2	722	1100	17.47
3	722	2000	16.5
4	18040	200	18.1
5	18040	1100	12
7	18040	1100	12.21
8	18040	2000	11.62
9	36080	200	15.96
10	36080	1100	14.21
11	36080	2000	13.5

After analyzing all the parameters and responses, a model has been suggested and optimized to get the desired value of interfacial tension. Table 4.3 represents, the suggested model for interfacial tension between the oil/water interphase in presence of CO₂. The regular coefficient of determination (R²), probability (Prob > F), adjusted coefficient of determination (Adj. R²), and predicted coefficient of determination (Pred. R²) are used to validate the suitability of regression models for Interfacial tension. In Table 4.3, the predicted R² value and adjusted R² value are highest for the cubic model respectively the values are 0.9067 and 0.9296. The sequential p-value is less than 0.0001, which implies that all the model terms are significant (Subasi et al., 2016). Based on all the coefficients the suggested model is the cubic model where the quartic model is aliased.

Table 4.3: Model summary statistics for IFT between brine/Dulang interface with CO₂

Source	Sequential p-value	Lack of Fit	Adjusted R²	Predicted R²	
Linear	< 0.0001	< 0.0001	0.4493	0.3919	
2FI	0.5816	< 0.0001	0.4359	0.3685	
Quadratic	< 0.0001	< 0.0001	0.7015	0.6175	
Cubic	< 0.0001	0.0641	0.9296	0.9067	Suggested
Quartic	0.0641		0.9439	0.9042	Aliased

Table 4.3 represents, the suggested model for interfacial tension between the oil/water inter phase in presence of CO₂. The regular coefficient of determination (R^2), probability (Prob > F), adjusted coefficient of determination (Adj. R^2), and predicted coefficient of determination (Pred. R^2) are used to validate the suitability of regression models for Interfacial tension. In Table 4.3, the predicted R^2 value and adjusted R^2 value are highest for the cubic model respectively the values are 0.9067 and 0.9296. The sequential p-value is less than 0.0001, which implies that all the model terms are significant (Subasi et al., 2016). Based on all the coefficients the suggested model is the cubic model where the quartic model is aliased.

4.2.3 Model Analysis

The cubic model (with CO₂ gas) is then subjected to an ANOVA analysis as the model is selected by the software. Table 4.4 represents the ANOVA for the cubic model (in presence of CO₂) and the first column represents all the parameters for the model where A is the concentration of brine (722-36080 ppm) and B was system pressure (200-2000 psi).

In this model, the F-value is 46.50 which indicates the model is significant. Here, P-value is not more than 0.0001 which implies all the model terms are significant. In this case, A, B, AB, A², B², A²B, AB², A³, B³ are significant model terms. For the significant model terms, the values should be less than 0.0001. if there several insignificant model terms are present, the reduction of these terms can improve the model. The Lack of Fit F-value of 2.86 implies there is a 6.41% chance that a Lack of Fit F-value this large could occur due to noise. A significant Lack of fit is bad. This relatively low probability (<10%) is troubling. Based on the sum of squares, mean square, F-value, and P-value the software suggested the cubic model is significant. Moreover, an insignificant lack of fit ensures a good fit for the model.

Table 4.4: ANOVA for Cubic model with CO₂

Source	Sum of Squares	Mean Square	F-value	p-value	
Model	383.44	42.60	46.50	< 0.0001	Significant
A-Concentration	22.13	22.13	24.16	< 0.0001	
B-pressure	48.33	48.33	52.75	< 0.0001	
AB	5.23	5.23	5.71	0.0258	
A ²	8.58	8.58	9.37	0.0057	
B ²	99.38	99.38	108.4	< 0.0001	
A ² B	15.62	15.62	17.04	0.0004	
AB ²	16.58	16.58	18.09	0.0003	
A ³	29.86	29.86	32.59	< 0.0001	
B ³	14.93	14.93	16.30	0.0006	
Residual	20.16	0.9162			
Lack of Fit	6.27	2.09	2.86	0.0641	not significant

Since the models have several negligible terms, they have been decreased and manually simplified by eliminating insignificant terms. After eliminating actual factors, the final empirical models can be expressed as follows,

$$IFT = 9.93 - 6.40A - 7.3B + 0.7610AB + 1.53A^2 + 5.82 B^2 + 2.50A^2 B - 2.79AB^2 + 8.38A^3 + 4.42B^3 \quad (4.1)$$

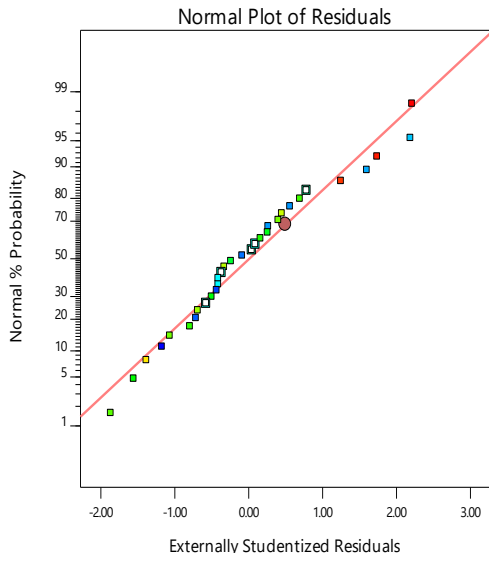
$$IFT = 20.38631 + (0.001070 * concentration) - (0.007710 * pressure) + (1.48729E - 07 * concentration * pressure) - (8.85969E - 08 * [concentration]^2) - (9.22987E - 06 * [Pressure]^2) + (8.89804E - 12 * [Concentration]^2 * pressure) - (1.94713E - 10 * concentration * [pressure]^2) + (1.51629E - 12 * [concentration]^3) + (6.05843E - 09 * [Pressure]^3) \quad (4.2)$$

Here, in equation (4.1), this is the coded equation where A, B, AB, A², B², A²B, AB², A³, B³ all these factors are significant so that these factors are used to generate the final empirical equation for determining interfacial tension between oil/water in presence of CO₂ gas. Moreover, equation 4.2 is representing the actual equation for this model from where any predicted value can be determined between the factor range. Suppose the concentration is 18040 and pressure is 200 psi, according to the equation 4.2,

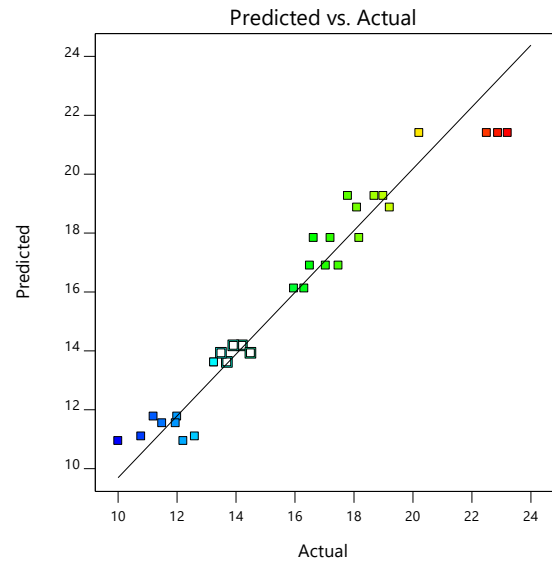
$$\begin{aligned}
 IFT &= 20.38631 + (0.001070 * 18040) - (0.007710 * 200) + (1.48729E - 07 * \\
 &18040 * 200) - (8.85969E - 08 * 18040^2) + (9.22987E - 06 * 200^2) + (8.89804E - \\
 &12 * 18040^2 * 200) - (1.94713E - 10 * 18040 * 200^2) + (1.51629E - 12 * 18040^3) - \\
 &(6.05843E - 09 * 200^3) \\
 &= 17.51 \text{ mN/m}
 \end{aligned}$$

From table 4.2, for 18040 ppm concentration, at 200 psi the IFT values from experiment is 18.11 mN/m where according to the equation 4.2, the IFT value is 17.51mN/m which is known as the predicted value by the software. The deviation between actual value and predicted value is 3.25%. which is representing the model can predict all the values properly as it has given almost same value as we got at the lab. Moreover, this equation can predict the IFT values for different concentration and pressure within the range.

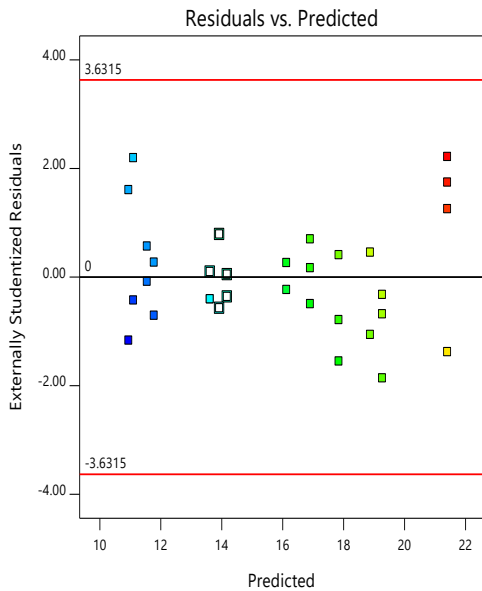
In Figure 4.1, four different types of graphs have been presented where red, green and blue colors are representing the IFT value range. For blue, green, and red the range of IFT is respectively 10-15 mN/m, 15-20 mN/m and 20-25 mN/m. Figure 4.1(a) indicates the normal probability vs externally studentized residual plot. The residual points (differences between the expected values and the test response values) on the straight line are used to ensure the regular distribution of the IFT model. Fig. 4.1(b) represents the expected and actual values of the IFT with the CO₂ model are in place and all the values are near to each other. The higher values are near to each other (red colour). Similarly, Fig. 4.1(c) displays the residual plot concerning increased expected response values. The random distribution of residuals within the graph's red limits demonstrates the precision and predictability of the model. Fig 4.1(d) indicates the residuals vs the run. In other words, the expected variables of the model do not show any clear increase or decrease (Mohammed et al., 2018)(Lai et al., 2014).



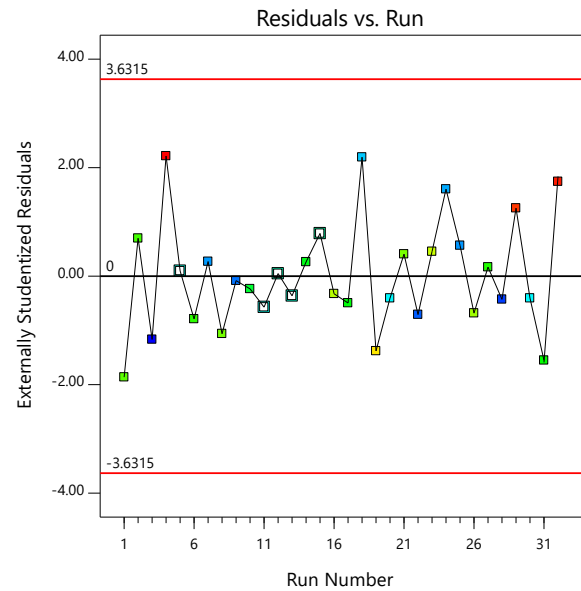
(a)



(b)



(c)



(d)

Figure 4.1: Model diagrams for IFT with CO₂ gas: (a) Normal probability vs. residuals (b) Predicted vs. Actual (c) Residuals vs. predicted (d) Residuals vs. Run

Figure 4.2(a) representing a IFT vs concentration graph where X axis is representing concentration in ppm and Y axis is representing IFT in mN/m at 1100 psi. it has been observed that the value of IFT is dependent on the concentration of brine when the oil phase is Dulang

(waxy crude) and the gas phase is CO₂. The IFT value initially decreased with increasing concentration, and it decreased till 26080 ppm and after that it started increasing and the trend changes to its lowest value. Due to the effect of CO₂ and pressure different concentration have given different values that is representing in the graph. Figure 4.2 (b) representing a IFT vs pressure graph where X axis is representing pressure in psi and Y axis is representing IFT in mN/m at 18040 ppm. The graph indicates that when the pressure increases the value of IFT decreases with it. The highest value of IFT is at 200psi pressure and the lowest value of IFT is at 1515.89 psi. After 1515.89 psi with the increasing pressure, the value of IFT increases. So, 1515.89 was the pressure in which we can get the lowest IFT value in presence of CO₂ gas.

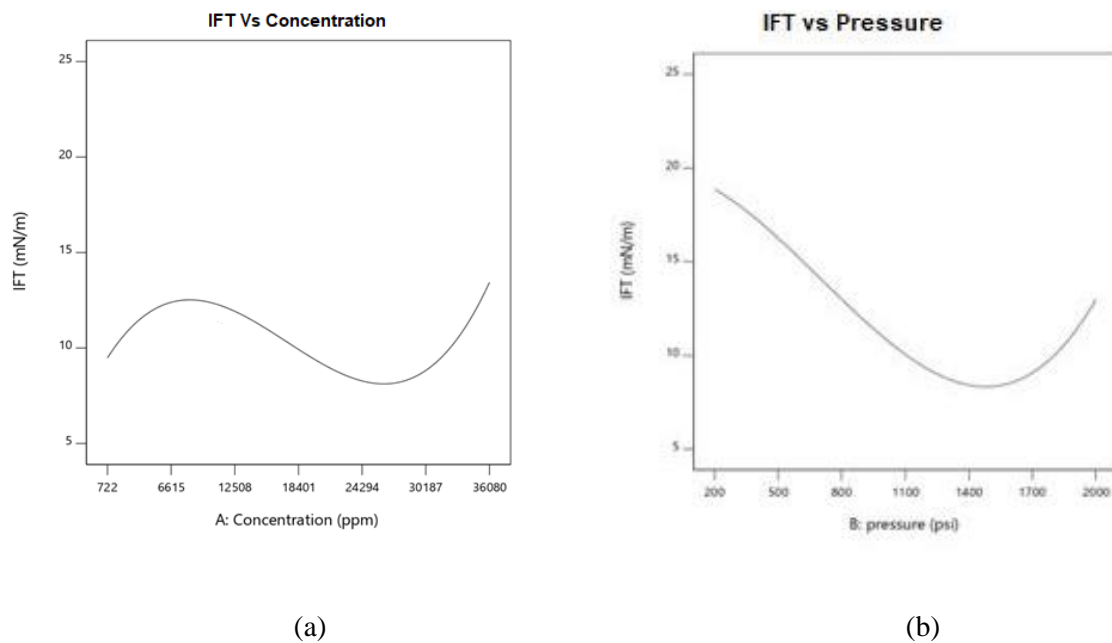


Figure 4.2: IFT vs concentration and pressure (with CO₂) (a) IFT vs. Concentration (at 2000psi) (b) IFT vs. Pressure (at 18040 ppm)

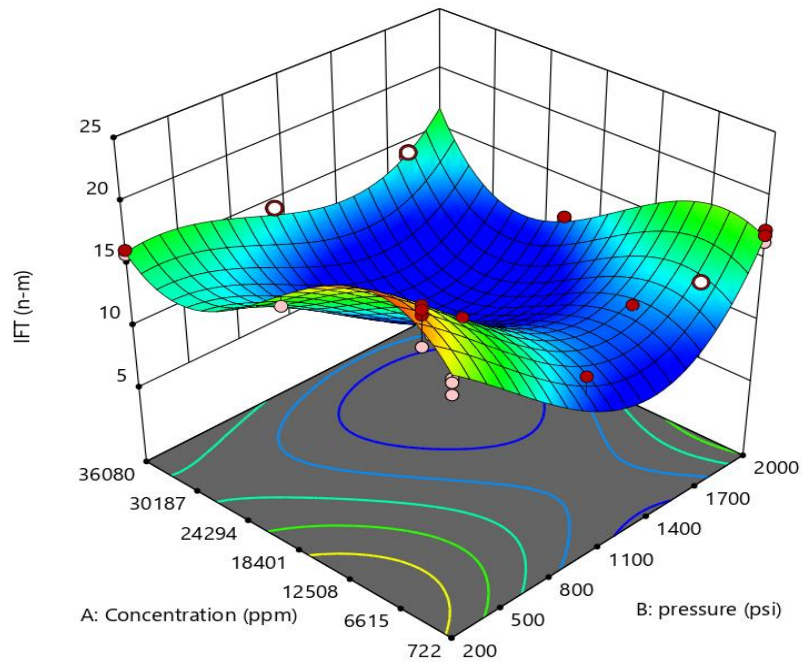


Figure 4.3: Synergistic effects of factors on IFT (with CO₂)

This 3D graph from Figure 4.3 can be used to determine the synergetic effect of pressure, concentration, and CO₂ gas on the interfacial tension. Interfacial tension was observed to increase with rising concentration and to decrease with increasing strain. The effect of CO₂ is more prominent in the IFT with CO₂ than the IFT without CO₂. For example, when the IFT is lowest, the concentration of brine is 26800 ppm, and the pressure is 1515.89 psi.

4.2.4 RSM Model for Brine/Dulang IFT without CO₂

After obtaining data from the experimental run without CO₂ according to the suggested DOE were added in the predetermined slots for the response as shown in Table 4.5.

According to Table 4.6, the predicted R² value and adjusted R² value are highest for the quadratic model respectively the values are 0.7338 and 0.8985 but for other models, the values of R² are not acceptable due to their negative value. The sequential P-value is less than 0.0001 only for the quadratic model which means the confidence level is more than 95% and the model

is significant. Finally, the quadratic model is suggested by the software where the quartic model is aliased.

Table 4.5: Actual design matrix for Dulang/ Brine IFT without CO₂

Run	Factor 1 A: Concentration ppm	Factor 2 B: pressure psi	Response 1 IFT mN/m
1	722	200	15.9
5	722	1100	13.49
6	722	2000	12.49
2	18040	200	12.66
3	18040	200	12.66
4	18040	1100	10.25
7	18040	2000	6.22
8	18040	2000	7.12
9	36080	200	11.91
10	36080	1100	9.339
11	36080	200	7.27

Table 4.6: Model Summary statistics for IFT between oil/water interface without CO₂

Source	Sequential p-value	Lack of Fit	Adjusted R²	Predicted R²	
Linear	0.6873	0.0833	-0.1133	-0.5539	
2FI	0.7803	0.0739	-0.2258	-1.5378	
Quadratic	< 0.0001	0.6419	0.8985	0.7338	Suggested
Cubic	0.4762	0.6111	0.9060	-23.1841	
Quartic	0.6111		0.8803		Aliased

4.2.5 Model Analysis

In the absence of CO₂ gas, the model is suggested quadratic model and after that, the model is subjected to an ANOVA analysis where the first column represents the parameters for the model. A is the concentration of brine (722-36080ppm) and B is pressure (200-2000psi). In Table 4.7, the F-value of this model is 22.24 which indicates the model is significant. Here, P-value is not more than 0.0001 which implies all the model terms are significant. In this case,

A, B, AB, A², and B² are significant model terms. For the significant model terms, the values should be less than 0.0001. if there several insignificant model terms are present, the reduction of these terms can improve the model.

Table 4.7: ANOVA for Quadratic model without CO₂

Source	Sum of Squares	Mean Square	F-value	p-value	
Model	94.32	18.86	22.24	0.0004	Significant
A- Concentration	0.0102	0.0102	0.0121	0.9156	
B-pressure	12.19	12.19	14.37	0.0068	
AB	6.49	6.49	7.66	0.0278	
A ²	49.09	49.09	57.88	0.0001	
B ²	38.12	38.12	44.94	0.0003	
Residual	5.94	0.8482			
Lack of Fit	3.94	0.7874	0.7874	0.6419	not significant

The Lack of Fit F-value of 0.79 implies there is a 64.19% chance that a Lack of Fit F-value this large could occur due to noise. A significant Lack of fit is bad. This relatively low probability (<10%) is troubling. Based on the sum of squares, mean square, F-value, and P-value the software suggested the quadratic model is significant. Final empirical models can be expressed as follows,

$$IFT = 3.09 - 0.0382A + 1.29B + 1.13AB + 5.52A^2 + 5.47B^2 \quad (4.3)$$

$$IFT = -1.14727 - (0.000731 * concentration) - (0.00119731 * pressure) - (0.001197E - 08 + 1.76735E - 10 * concentration^2) + (6.75340E - 08 * pressure^2) \quad (4.4)$$

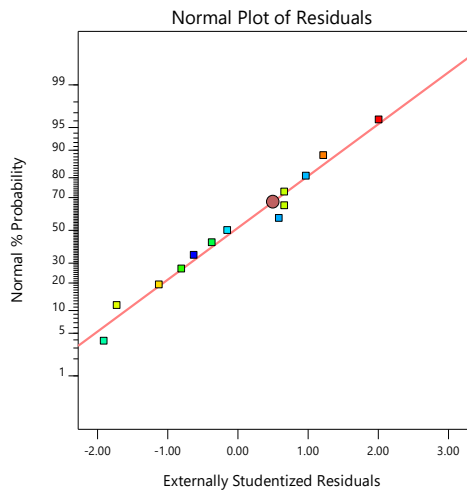
Here, in equation (4.3), this is the coded equation where A, B, AB, A², B² all these factors are significant so that these factors are used to generate the final empirical equation for determining interfacial tension between oil/water in presence of CO₂ gas. Moreover, equation 4.4 is representing the actual equation for this model from where any predicted value can be

determined between the factor range. Suppose the concentration is 18040 and pressure is 200 psi, according to the equation 4.4,

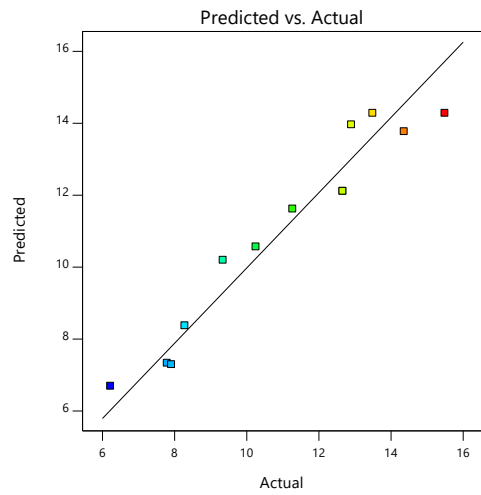
$$\begin{aligned}
 IFT &= -1.14727 - (0.000731 * 18040) - (0.0014731 * 200) - (0.001197E - 08 \\
 &\quad + 1.76735E - 10 * 18040^2) + (6.75340E - 08 * 200^2) \\
 &= 11.15 \text{ mN/m}
 \end{aligned}$$

From table 4.2, for 18040 ppm concentration, at 200 psi the experimental IFT value is 12.2 mN/m whereas the predicted value of the software is 11.15 mN/m where the deviation between the predicted value and the actual value is only 8.27%. This equation is representing how this equation can predict all the value almost like the values we got from the experiment. Moreover, this model can predict the IFT values for different concentration and pressure within the range.

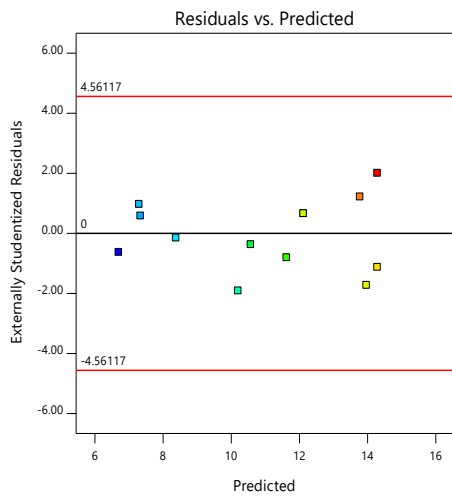
Here, in equations 4.3 A, B, AB, A², B² all these factors were significant so that these factors are used to generate the final empirical equation for determining interfacial tension between oil/water without CO₂ gas. The equation is useful for identifying the relative impact of the factors by comparing the factor coefficients. This equation can be used to make the response predictions for a given level of each factor. In Figure 4.2, four different types of graphs have been presented where red, green and blue colors are representing the IFT value range. For blue, green, and red the range of IFT is respectively 6-9 mN/m, 9-12 mN/m and 12-15 mN/m. In Figure 4.4 all the diagnostic plots are in the range so it is clear that the model will predict all the responses accurately like the previous model.



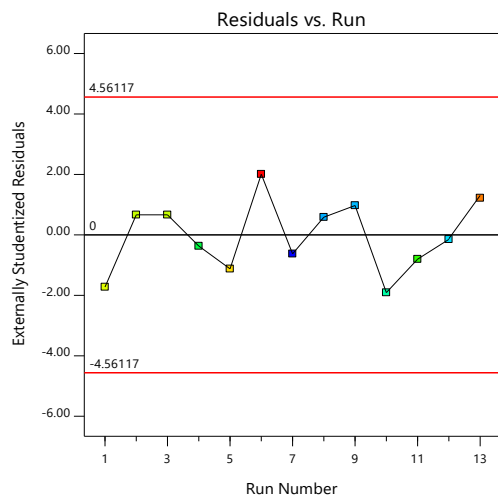
(a)



(b)



(c)



(d)

Figure 4.4: Model diagrams for IFT without CO₂ gas. (a) Normal probability vs. residuals (b) Predicted vs. Actual (c) Residuals vs. predicted (d) Residuals vs. Run

4.2.6 Optimization Using RSM

Based on the models obtained in the previous section, we further determined the optimum brine concentration and pressure that would lead to minimum oil/water IFT for both CO₂ and without CO₂ cases. RSM is a very effective technique to predict interfacial tension values in presence of CO₂ and the absence of CO₂ too.

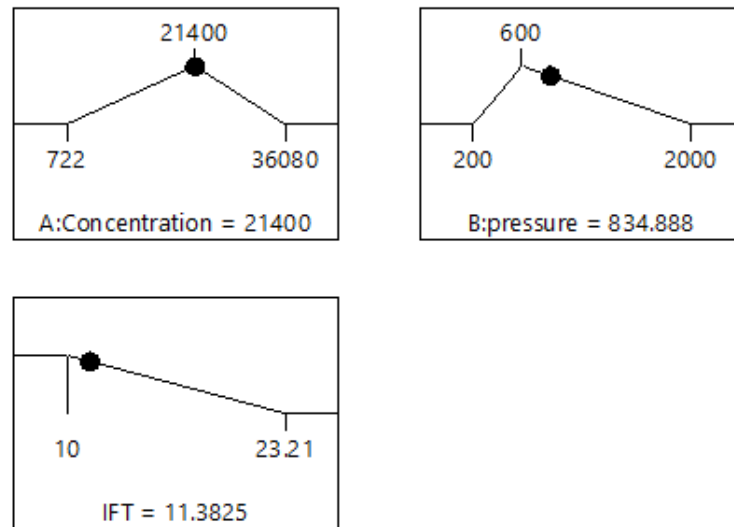


Figure 4.5: Optimization ramp for IFT with CO₂

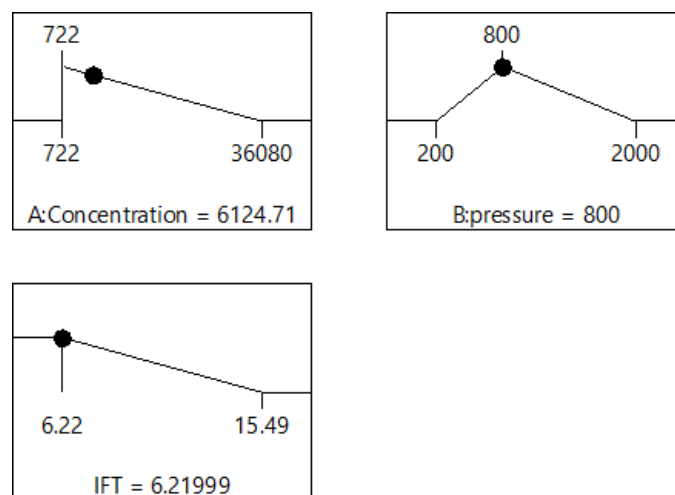


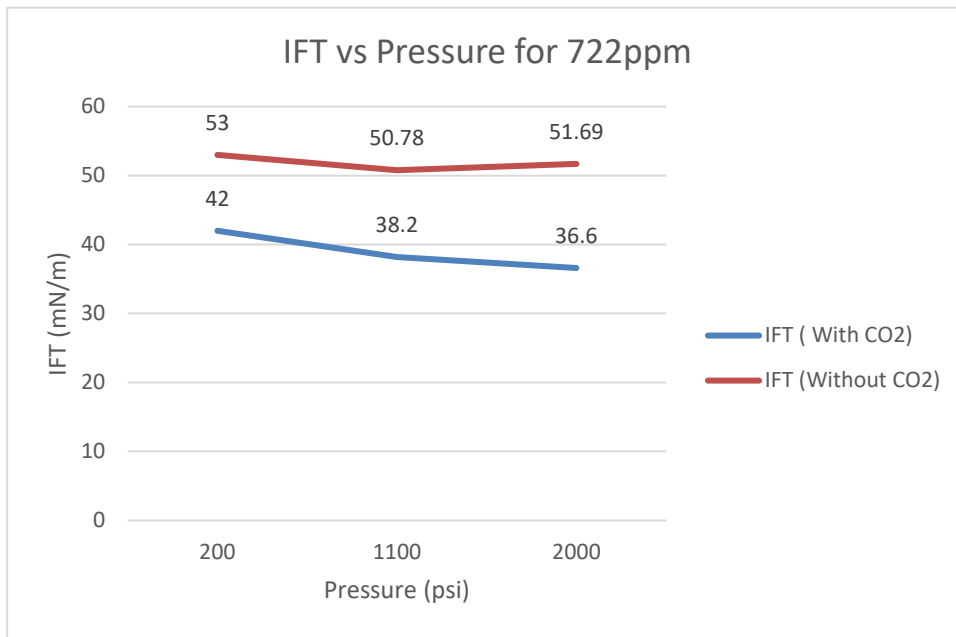
Figure 4.6: Optimization ramp for IFT without CO₂

Figure 4.5 provides a ramp presentation of the optimization and represents brief optimization data of the IFT modelling with CO₂. Here, for optimization the concentration was in a target (21400 ppm), the pressure was in a target (600 psi) and the IFT value was minimized because when oil/water IFT is minimum, it will reduce the capillary force that held the oil, which further helps in mobilization and transportation of oil. The value of IFT is 11.3825 mN-m for the concentration of 21400 ppm and the pressure of 600 psi. The desirability of the predicted IFT value is 0.907. that means it is 90.7% acceptable.

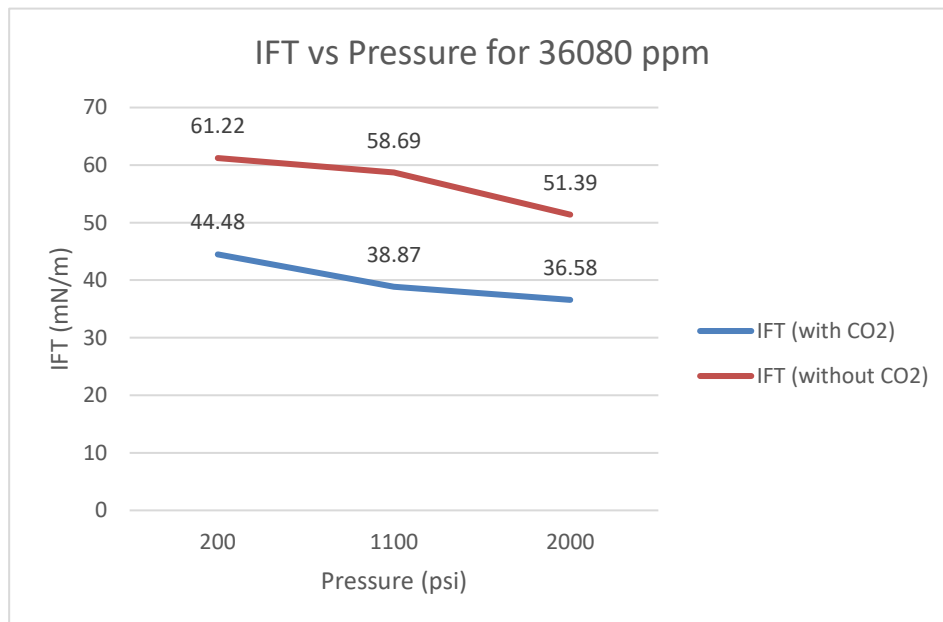
For optimization, in Figure 4.6 the concentration is in a target (722), the pressure is in a target (800 psi) and the IFT value is 6.2199. the IFT value is lowest, it is better for fluid movement held in the rock. the value of IFT is 11.3825 mN-m for the concentration of 722ppm and the pressure 800psi according to Figure 4.5.

4.2.7 Brine/Decane IFT with and without CO₂

From Decane with CO₂ and Decane without CO₂ RSM model, it has been observed that after adding all the obtaining response data from the experimental run according to the suggested DOE in the predetermined slots for the response, RSM suggested quadratic model for both conditions. The interaction model graphs present an intercorrelation analysis among salinity, pressure, and interfacial tension. Furthermore, from the preliminary analysis, brine/decane IFT vs pressure and brine/decane IFT vs Concentration with CO₂ and without CO₂ has been discussed thoroughly.



(a)



(b)

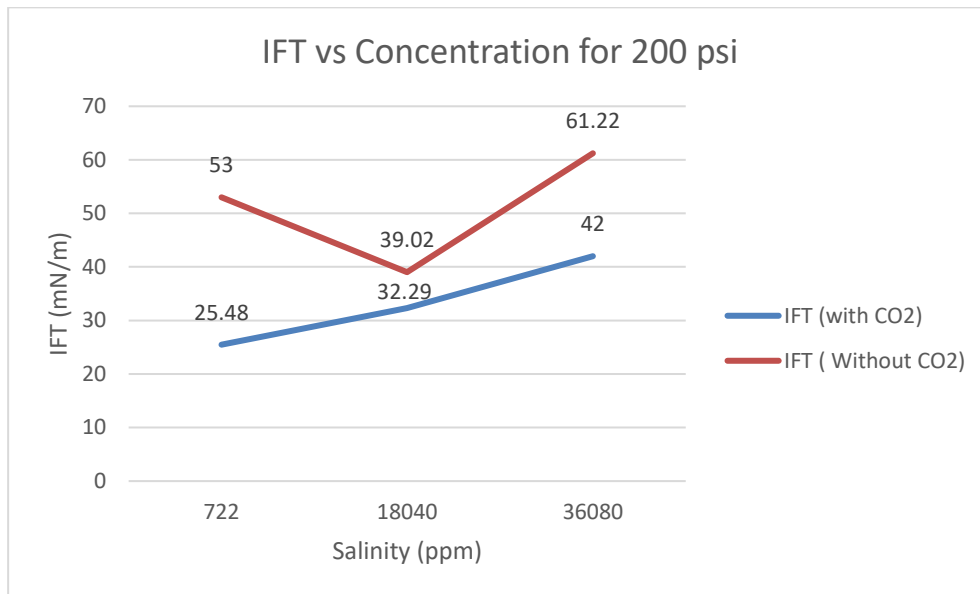
Figure 4.7: Brine/decane IFT vs pressure graph (a) for 722ppm, (b) for 36080 ppm

Here, Figure 4.7 (a) is representing the brine/decane IFT vs pressure graph with and without CO₂ for 722 ppm salinity and 4.7 (b) is representing another graph for brine/decane IFT vs pressure with and without CO₂ for 36080 ppm salinity. For graph 4.7 (a), the Blue trendline is representing the change in IFT for 722 ppm concerning pressure in presence of CO₂ gas and the red trendline is representing the change in IFT for 722 ppm with respect to the pressure in absence of CO₂ gas. A closer inspection of the graph shows that there is a clear trend of IFT value which is decreasing with the increasing pressure for 722 ppm salinity in the presence and absence of CO₂. Furthermore, the value of IFT is lower for 200-2000 psi pressure when CO₂ is present in the system. At 2000 psi, the value of IFT with CO₂ is 36.6 mN/m whereas the value of IFT without CO₂ condition is 51.69 mN/m which is quite higher. Due to the simultaneous effect of pressure and CO₂ gas, the value of the blue trendline has decreased significantly. Whereas due to the only effect of pressure the value of IFT without CO₂ has not decreased dramatically. From this discussion, it can be seen that the effect of CO₂ has played an important role to decrease the value of IFT which is desirable for more recovery.

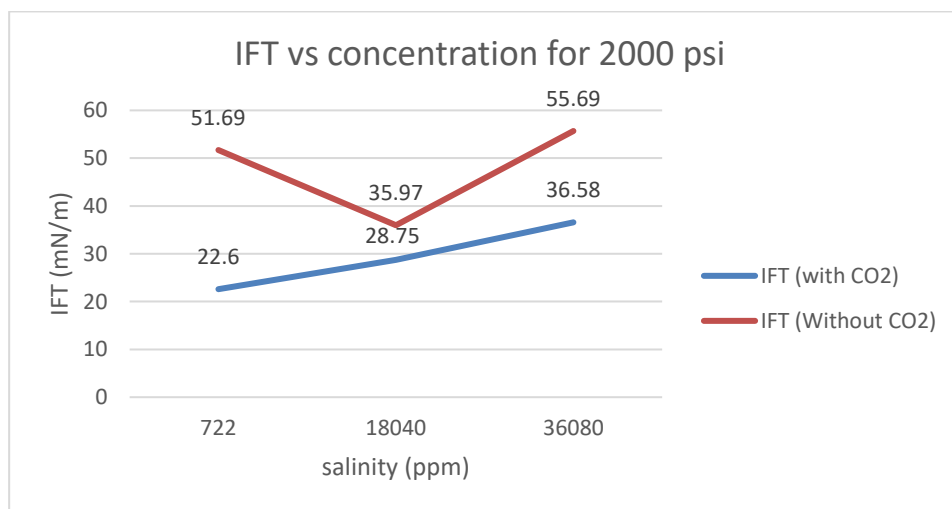
For Figure 4.7 (b), the blue trendline is representing the change in IFT for 36080 ppm concerning pressure in presence of CO₂ gas and the red trendline is representing the change in IFT for 36080 ppm with respect to the pressure in absence of CO₂ gas. From 4.7 (b) the value of IFT has decreased with increasing pressure for both with CO₂ and without CO₂ conditions. When CO₂ is not present in the system the value of IFT is higher than in the system with CO₂. For the blue trendline, the value of IFT is higher for lower pressure and with increasing pressure, the value of IFT has decreased from 42 to 36.6 mN/m. Moreover, Due to the simultaneous effect of pressure and CO₂, it can be observed from the blue trendline that the value of IFT has decreased dramatically than the red trendline.

The red trendline from Figure 4.7(a) can be compared with the red trendline in 4.7(b) and the IFT value has decreased for both trendlines with increasing pressure. Furthermore, the value of IFT is higher for high salinity water (36080 ppm) than for the low salinity water (722 ppm) trendline. In 4.7 (a), at 200 psi pressure, the value of IFT is 53mN/m and 51.69 mN/m at 2000 psi pressure. On the other hand, in Figure 4.7 (b), at 200 psi pressure, the value of IFT is 61 mN/m and 51.39 mN/m at 2000 psi pressure. From the closer inspection of two blue trendlines, it can be observed that due to the simultaneous effect of pressure and CO₂ the trendline has

decreased significantly in Figures 4.7 (a) and 4.7 (b) but for low salinity water it has decreased more than high salinity water. The effect of CO₂ and pressure in interfacial tension is visible in these trendlines and the presence of CO₂ has decreased IFT values significantly.



(a)



(b)

Figure 4.8: Brine/decane IFT vs Concentration graph (a) at 200 psi (b) at 2000 psi

Figure 4.8 (a) is representing the brine/decane IFT vs concentration graph with and without CO₂ for 200 psi pressure and 4.8 (b) is representing another graph for brine/decane IFT vs concentration with and without CO₂ for 2000 psi salinity. For graph 4.8 (a), the blue trendline is representing the change in IFT for 200 psi pressure with respect to concentration in presence of CO₂ gas and the red trendline is representing the change in IFT at 200psi with respect to concentration in absence of CO₂ gas. Now turning to the experimental evidence on two blue trendlines from 4.8 (a), it is clear that at 200 psi pressure the value of IFT is increasing with increasing concentration. For low salinity water, the value of IFT is lower and this may happen due to the solubility of CO₂ at 200psi pressure in low salinity water. For the blue trendline when CO₂ is present in the system, all the IFT values have increased with increasing concentration which is usually according to Oren et al. and Vizika et al. (Oren and Pinczewski, 1994; Vizika et al., 1998). Furthermore, from the red trendline, it can be visualized that the value of IFT is much higher than the blue trendline and due to absence of CO₂ in the system may cause this situation.

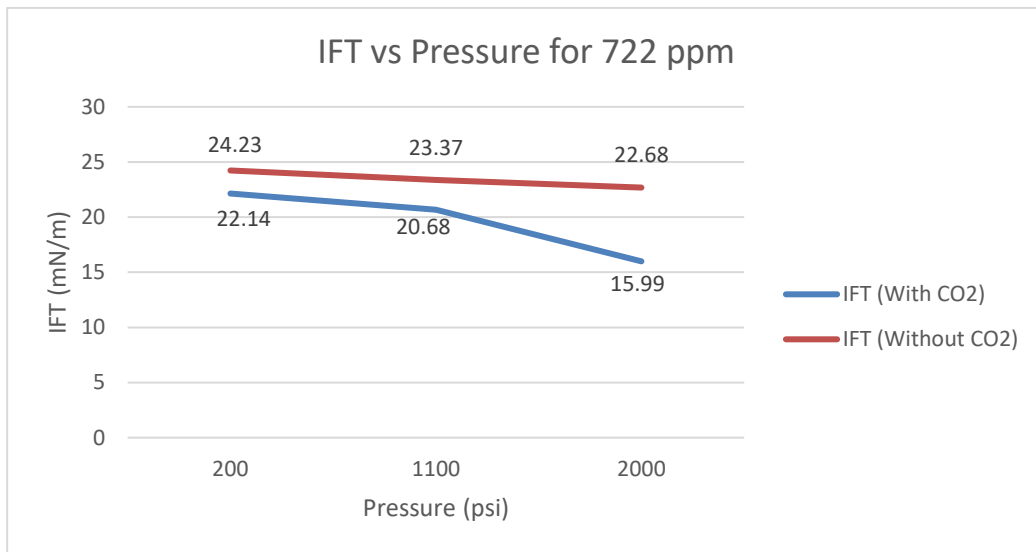
For graph 4.8 (b), the blue trendline is representing the change in IFT for 2000 psi pressure with respect to concentration in presence of CO₂ gas and the red trendline is representing the change in IFT at 2000 psi with respect to concentration in absence of CO₂ gas. In this figure, the trendlines are also showing the same shifting as 4.8 (a). the value of IFT is increasing with increasing concentration. At 2000 psi pressure, for 722 ppm concentration, the IFT is 51.69 mN/m and 55.69 mN/m for 36080 ppm. That means, that low salinity water at higher pressure is giving less interfacial tension which is desirable for more recovery, and it is indicating that CO₂ is more soluble in low salinity water under high pressure.

Trendlines from Figure 4.8 (a) can be compared with the trendlines in 4.8 (b) and the IFT value has increased for both trendlines with increasing concentration. In figure 4.8 (b) the value of IFT for red and blue trendlines is lower than the value of IFT in Figure 4.8 (a). The effect of pressure can be observed from this comparison. Moreover, the Blue trendline from both 4.8 (a) and (b) has given lower IFT and it may happen due to the presence of CO₂ in the system. If a comparison is held between the red trendline and blue trendline then it will be easy to represent the effect of CO₂ during a decrease in the value of IFT. For both figures, the red trendlines have given a higher IFT value than the blue trendline. In 4.8 (b) the lowest value of IFT has given

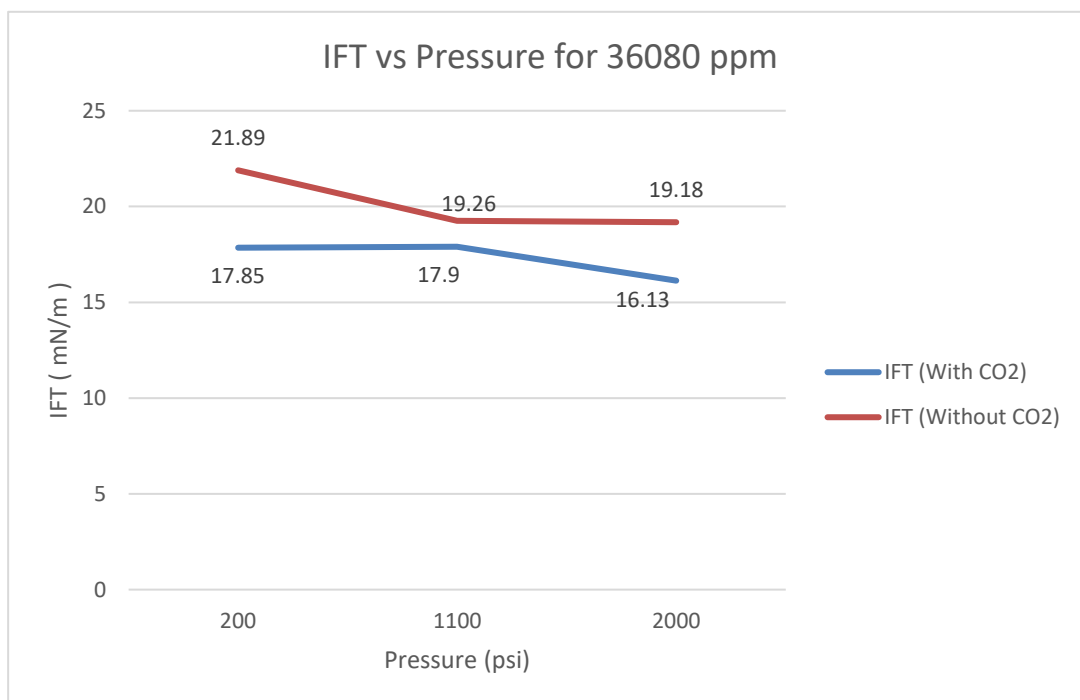
at 2000psi pressure, 722 ppm salinity, and in presence of CO₂. From a closer inspection, it can be said that due to the CO₂ gas and pressure effect the value of IFT has been decreased significantly.

4.2.8 Brine/ Dulang+Decane IFT with and without CO₂

In Dulang+Decane mixture IFT with and without CO₂, from the response surface methodology model, after adding all the responses in the response slot according to the suggested design of experiment (DOE), the software suggested two models based on responses. Furthermore, the Quadratic model has been suggested for both conditions (with CO₂ and without CO₂) where both models are significant as well as lack of fit is not significant. In this part, a Simple graphical analysis has been used to highlight the relation between IFT with salinity and pressure at reservoir temperature with CO₂ and without CO₂. Besides, the effect of CO₂ has been discussed clearly to represent the change in interfacial tension trendlines in the presence and absence of CO₂ gas.



(a)



(b)

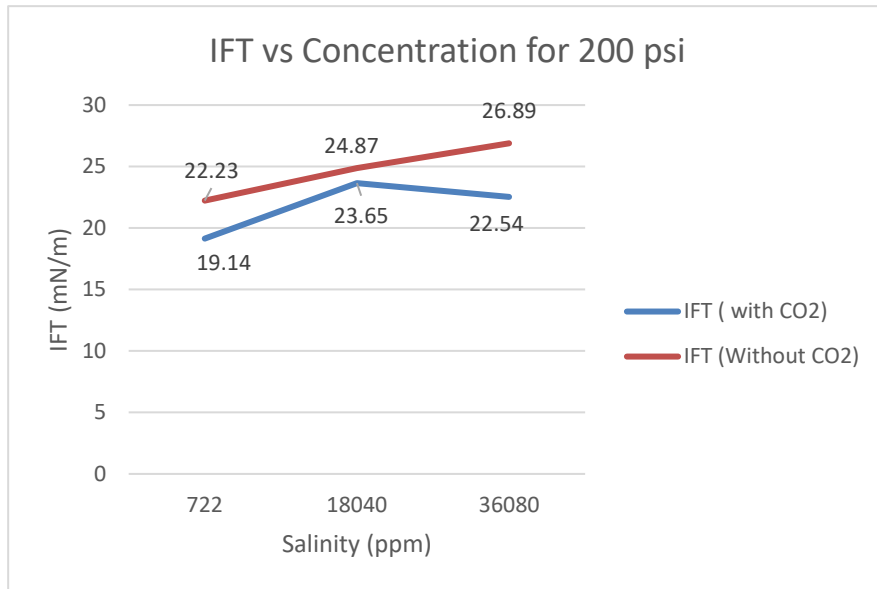
Figure 4.9: Brine/ Decane+Dulang IFT vs pressure (a) for 722 ppm (b) for 36080 ppm

Here, Figure 4.9 (a) is representing the brine/Dulang+Decane IFT vs pressure graph for 722ppm salinity and 4.9 (b) is representing another graph for brine/Dulang+Decane IFT vs pressure for 36080 ppm salinity. For graph 4.9 (a), the Blue trendline is representing the change in IFT for 722 ppm salinity with respect to the pressure in presence of CO₂ gas and the red trendline is representing the change in IFT for 722 ppm salinity with respect to the pressure in absence of CO₂ gas. In Figure 4.9 (a) with increasing pressure, the value of IFT is decreasing for both with CO₂ and without CO₂ conditions. In 4.9 (a), the blue trendline at 200 psi has given a value of IFT 22.14 mN/m and 15.99 mN/m at 2000 psi pressure. From here it can be seen that with increasing pressure, the value of IFT has decreased. whereas the IFT value for the red trendline in Figure 4.9 (a) has decreased slightly. This change in both trendlines has happened due to the presence of CO₂ gas in the system and the effect is significantly visible in the Figures. The presence of CO₂ has helped to decrease the value of IFT in the blue trendline more.

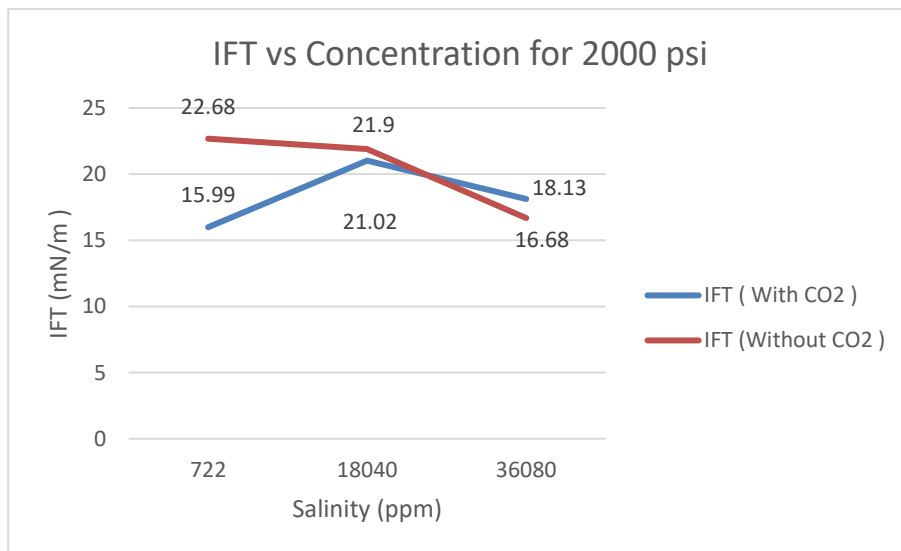
For graph 4.9 (b), the blue trendline is representing the change in IFT for 36080 ppm with respect to the pressure in presence of CO₂ gas and the red trendline is representing the change in IFT for 36080 ppm with respect to the pressure in absence of CO₂ gas. From 4.9 (b) the value of IFT has decreased with increasing pressure for both with CO₂ and without CO₂ conditions. When CO₂ is not present in the system the value of IFT is higher than in the system with CO₂. For the blue trendline, the value of IFT is higher for lower pressure and with increasing pressure, the value of IFT has decreased from 17.85 to 16.13 mN/m. Moreover, Due to the simultaneous effect of pressure and CO₂, it can be observed that from the blue trendline the value of IFT has decreased dramatically than the red trendline.

The red trendline from Figure 4.9 (a) can be compared with the red trendline in 4.9(b) and the IFT value has decreased for both trendlines with increasing pressure. Furthermore, the value of IFT is higher for high salinity water (36080 ppm) than for the low salinity water (722 ppm) trendline. In 4.9 (a), for the blue trendline at 200 psi pressure, the value of IFT is 22.14 mN/m and 15.99 mN/m at 2000 psi pressure. On the other hand, in Figure 4.9 (b), for the blue trendline at 200 psi pressure, the value of IFT is 17.85 mN/m and 16.13 mN/m at 2000 psi pressure. From the closer inspection of two blue trendlines it can be observed that due to the simultaneous effect of pressure and CO₂ the trendline has decreased significantly in Figures 4.9 (a) and 4.9 (b). Moreover, low salinity water has decreased more than high salinity water. The effect of

CO₂ and pressure in interfacial tension is visible in these trendlines and the presence of CO₂ has decreased IFT values significantly.



(a)



(b)

Figure 4.10: Brine/Decane+Dulang IFT vs concentration (a) at 200 psi (b) at 2000 psi

Figure 4.10 (a) is representing the Brine/Decane IFT vs concentration graph with and without CO₂ for 200 psi pressure and 4.10 (b) is representing another graph for brine/decane IFT vs concentration with and without CO₂ for 2000 psi salinity. For graph 4.10 (a), the blue trendline is representing the change in IFT for 200 psi pressure with respect to concentration in presence of CO₂ gas and the red trendline is representing the change in IFT at 200psi with respect to concentration in absence of CO₂ gas. From the experimental analysis on two blue trendlines from 4.10 (a), it is clear that at 200 psi pressure the value of IFT is increasing with increasing concentration. For low salinity water, the value of IFT is lower and this may happen due to the solubility of CO₂ at 200psi pressure in low salinity water. For the blue trendline when CO₂ is present in the system, all the IFT values have increased with increasing concentration which is usual to increase the recovery. Furthermore, from the red trendline, it can be visualized that the value of IFT is much higher than the blue trendline and due to absence of CO₂ in the system may cause this situation.

. For graph 4.10 (b), the blue trendline is representing the change in IFT for 2000 psi pressure with respect to concentration in presence of CO₂ gas and the red trendline is representing the change in IFT at 2000 psi with respect to concentration in absence of CO₂ gas. In this Figure, the trendlines are also showing the same shifting as 4.10 (a). The value of IFT is increasing with increasing concentration and pressure. At 2000 psi pressure, for 722 ppm concentration, the IFT is 15.99 mN/m and 16.68 mN/m for 36080 ppm. That means, that low salinity water at higher pressure is giving less interfacial tension which is desirable for more recovery, and it is indicating that CO₂ is more soluble in low salinity water under high pressure.

From the graphical analysis, it is easy to compare the trendlines from Figures 4.10 (a) and 4.10 (b) and the IFT value has increased for both trendlines with increasing concentration. In figure 4.10 (b) the value of IFT for red and blue trendlines is lower than the value of IFT in Figure 4.10 (a). The effect of pressure can be observed from this comparison. Moreover, the blue trendline from both 4.10 (a) and (b) has given lower IFT and it may happen due to the presence of CO₂ in the system and the solubility of CO₂ in low salinity water under high pressure. If a comparison is held between the red trendline and blue trendline then it will be easy to represent the effect of CO₂ during a decrease in the value of IFT. For both figures, the red trendlines have given a higher IFT value than the blue trendline. In 4.8 (b) the lowest value

of IFT has given at 2000psi pressure, 722 ppm salinity, and in presence of CO₂. From a closer inspection, it can be said that due to the CO₂ gas and pressure effect the value of IFT has decreased significantly.

4.2.9 Discussions from Interfacial Tension Measurement

From IFT vs pressure in the presence and absence of CO₂ gas graphs, it can be stated that the effect of CO₂ is visible for each graph. The change in trendlines may happen due to three factors individually or simultaneously and the factors are pressure, brine concentration, and CO₂ gas.

From Figure 4.7 (a) and (b), decane/brine with and without CO₂ IFT results show that IFT values have decreased with increasing pressure. While CO₂ gas is present in the system the value of IFT is less than the system without CO₂. The IFT values for 722ppm salinity under reservoir pressure have decreased in a significant way than the IFT values for 722 ppm under 200 psi pressure without CO₂ condition. The effect of CO₂ gas, pressure, and salinity has been discussed and observed from the graphical analysis.

For Dulang+Decane/brine fluid system with and without CO₂, it has been observed that CO₂ has positively shifted the trendline. The presence of CO₂ gas for low salinity water has given a lower IFT value than the system containing no CO₂. Also, high salinity water has given a higher value of IFT with respect to the blue trendline. It has been observed from all the figures that with increasing pressure the value of IFT has decreased and with increasing concentration, the value of IFT has increased.

Change in trendlines due to the presence of CO₂ may happen due to the solubility of CO₂ in numerous brine concentrations. When the solubility of CO₂ is higher for any specific concentration than others, the change in trendlines is more prominent for those. In this work, it has been analyzed that for low salinity water with CO₂, trendlines are changing significantly with an indication of CO₂ solubility in low salinity water than in high salinity water. However, some trendlines have changed slightly with an indication that either the effect of pressure and the solubility of CO₂ was moderate for that specific concentration or individually these two

factors were not stable for such concentration. Though it has been noticed that for low salinity water with CO₂ conditions, the interfacial values are decreasing with increasing pressure which is desirable according to Teklu et al. (Teklu et al., 2016a, 2014). For without CO₂ condition, interfacial values have not decreased significantly as well as the effect of pressure was also noticeable.

4.3 Spreading Coefficient Measurement

In this section, utilizing the values of brine/decane, brine/Dulang, and brine/Decane+Dulang IFT along with gas/oil and gas/water surface tension, spreading coefficient calculation and graphical analysis have been discussed specifically. The effect of CO₂ on the spreading coefficient has been discussed after critical analysis. For Dulang with CO₂ and without CO₂, spreading coefficient calculations have been calculated but for decane with and without CO₂ and Decane+Dulang with and without CO₂ only graphical representation has been broadly presented. In addition, all the IFT and surface tension experiments have been conducted at 96°C temperature and (200-2000) psi pressure.

4.3.1 Spreading Coefficient of Dulang with CO₂

From Table 4.8, it has been observed that the spreading coefficient for Dulang with CO₂ has been reported in this work. Before that spreading coefficient for Dulang with CO₂ was not reported in most of the literature review and we get the spreading coefficient values are positive for Dulang. For the high concentration of 36080 ppm, the spreading coefficient value slightly fluctuates with increasing pressure. But when the concentration decreases, with increasing pressure spreading coefficient values, starts increasing. When it is 1804 ppm, the spreading value at 200psi pressure is as low as 2 mN/m. From the literature reviews, the oil can disperse as a thin film on the water substrate when the gas phase is present, and this oil film supports the hydraulic consistency of the oleic phase, resulting in higher oil recovery and lower residual oil saturation. If the value of S is positive, the oil can disperse in the presence of the gas phase as a thin film on the water substrate. The trends for each concentration with changing pressure have been represented in the following graph.

Table 4.8: Spreading coefficient for Dulang with CO₂

Salinity(ppm)	Pressure(psi)	γ_{gw} (mN/m)	γ_{go} (mN/m)	γ_{ow} (mN/m)	Spreading Coefficient (mN/m)
36080	200	83.675	17.964	15.96	49.751
	400	78.889	14.261	16.36	48.268
	600	76.963	11.339	15.87	49.754
	800	72.636	10.364	14.96	47.312
21400	200	73.996	17.964	19.28	36.752
	400	70.542	14.261	17.76	38.521
	600	69.478	11.339	16.14	41.999
18040	200	65.335	17.964	18.872	28.499
	400	61.456	14.261	17.256	29.939
	600	61.003	11.339	15.202	34.462
	800	59.999	10.364	13.001	36.634
7216	200	53.957	17.964	22.453	13.54
	400	50.583	14.261	20.281	16.041
	600	49.774	11.339	17.84	20.595
3608	200	45.5	17.964	21.889	5.647
	400	44.141	14.261	19.883	9.997
	600	42.824	11.339	17.614	13.871
1804	200	41.826	17.964	20.99	2.872
	400	40.665	14.261	17.927	8.477
	600	37.732	11.339	15.44	10.953
722	200	41.696	17.964	19.59	4.142
	400	40.335	14.261	16.96	9.114
	600	37.654	11.339	14.49	11.825

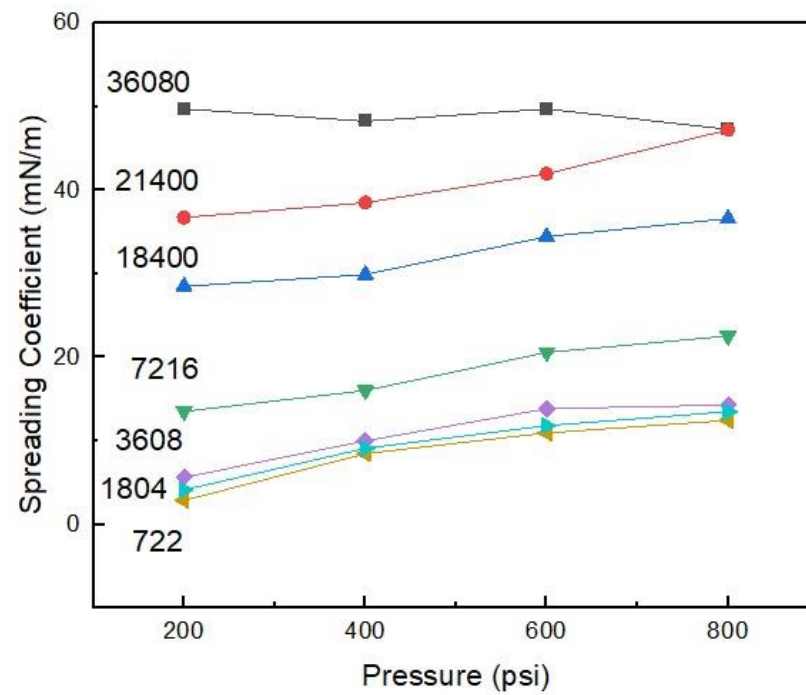


Figure 4.11: Spreading coefficient vs pressure graph for Dulang with CO₂

Figure 4.11 represents the spreading coefficient vs pressure trends for different concentrations. With the changing concentration and pressure spreading coefficient also changes. From the graph, for high salinity water, the spreading coefficient has changed slightly with increasing pressure whereas the low salinity water spreading coefficient has increased prominently with pressure. The most noticeable aspect of this graph is all the concentrations is giving a positive spreading coefficient which is a positive sign to increase the recovery.

4.3.2 Spreading Coefficient of Dulang Without CO₂

From Table 4.9, the spreading coefficient for Dulang without CO₂ is also positive. For the high concentration of 36080 ppm, the spreading coefficient value slightly fluctuates with increasing pressure but when the concentration decreases, with increasing pressure spreading coefficient values start increasing. When it is 1804 ppm, the spreading value at 200psi pressure is not as low as the previous one (with CO₂). It has been established that, the oil can disperse as a thin film on the water substrate when the gas phase is present, and this oil film supports the hydraulic conductivity of the oleic phase, resulting in higher oil recovery and lower residual oil saturation. If the value of S is positive, the oil can disperse in the presence of the gas phase as a thin film on the water substrate. The trends for each concentration with changing pressure have been represented in the following graph.

Table 4.9: Spreading coefficient for Dulang without CO₂

Salinity (ppm)	Pressure (psi)	γ_{gw} (mN/m)	γ_{go} (mN/m)	γ_{ow} (mN/m)	Spreading Coefficient(mN/m)
36080	200	83.675	17.964	11.19	54.521
	400	78.889	14.261	9.99	54.638
	600	76.963	11.339	8.917	56.707
	800	72.636	10.364	8.376	53.896
21400	200	73.996	17.964	7.29	48.742
	400	70.542	14.261	5.39	50.891
	600	69.478	11.339	4.107	54.032
	800	69.002	10.364	3.356	55.282
18040	200	65.335	17.964	6.3	41.071
	400	61.456	14.261	5.41	41.785
	600	61.003	11.339	4.07	45.594
	800	59.999	10.364	3.27	46.365
7216	200	53.957	17.964	10.22	25.773
	400	50.583	14.261	8	28.322
	600	49.774	11.339	6.69	31.745
	800	49.08	10.364	5.74	32.976
3608	200	45.5	17.964	12.116	15.42
	400	44.141	14.261	10.031	19.849
	600	42.824	11.339	8.487	22.998
	800	40.75	10.364	7.483	22.903
1804	200	41.826	17.964	13.236	10.626
	400	40.665	14.261	11.126	15.278
	600	37.732	11.339	9.556	16.837
	800	35.905	10.364	8.526	17.015
722	200	41.696	17.964	13.963	9.769
	400	40.335	14.261	11.837	14.237
	600	37.654	11.339	10.252	16.063
	800	36.008	10.364	9.207	16.437

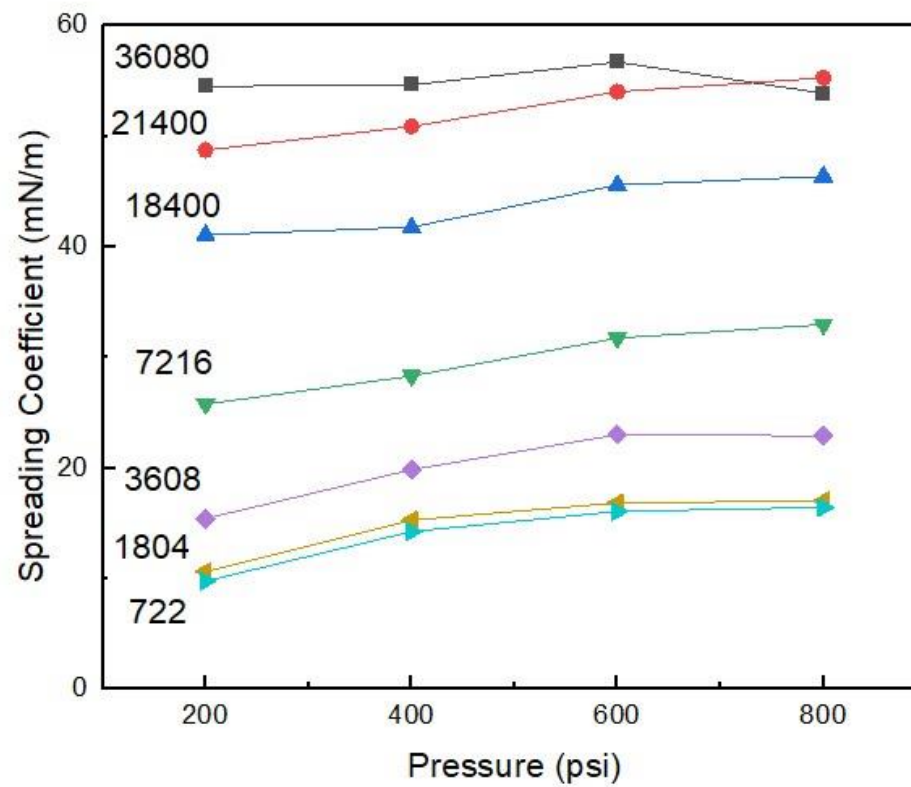


Figure 4.12: Spreading coefficient vs pressure graph for Dulang without CO₂

Figure 4.12 represents the spreading coefficient vs pressure trends for different concentrations. With the changing concentration and pressure, the spreading coefficient also changes. From the graph analysis, we can say that the spreading coefficient value is higher for Dulang without CO₂ than Dulang with CO₂, though the difference is not so high also those conditions is giving a positive spreading coefficient.

4.3.3 Spreading Coefficient of Decane with and without CO₂

In this part, the spreading coefficient of decane with and without CO₂ graph has been summarized and reported significant changes due to changes in pressure and brine salinity.

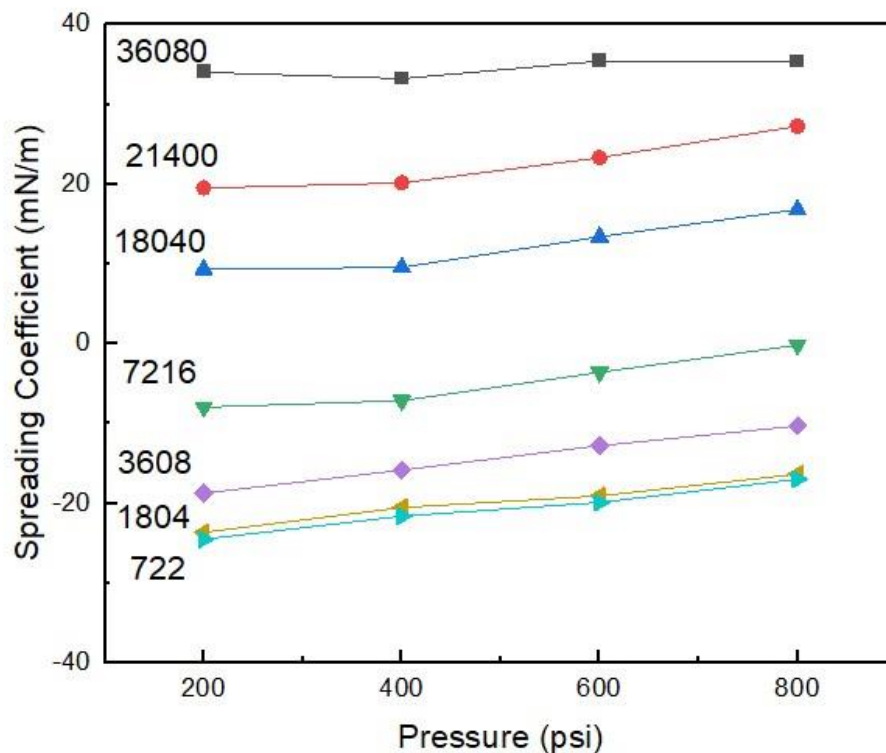


Figure 4.13: Spreading coefficient vs pressure graph for decane with CO₂

In Figure 4.13, the presence of CO₂, an upward shift has been observed in this graph. Spreading coefficient for 36080 ppm has given positive value due to presence of CO₂ where in Figure 4.14 for without CO₂ condition 36080ppm has given a negative value. It is giving a clear idea that the presence of CO₂ has played an important role after this upward shift. The

spreading coefficient value from this graph can be compared with the value in Figure 4.14 which shows in this trendline the value of the spreading coefficient has increased significantly than Figure 4.13 and giving a positive value which is a positive sign towards enhancing oil recovery. A closer inspection of Figure 4.13 shows spreading coefficients for all the trend has increased with increasing pressure which is a usual shift.

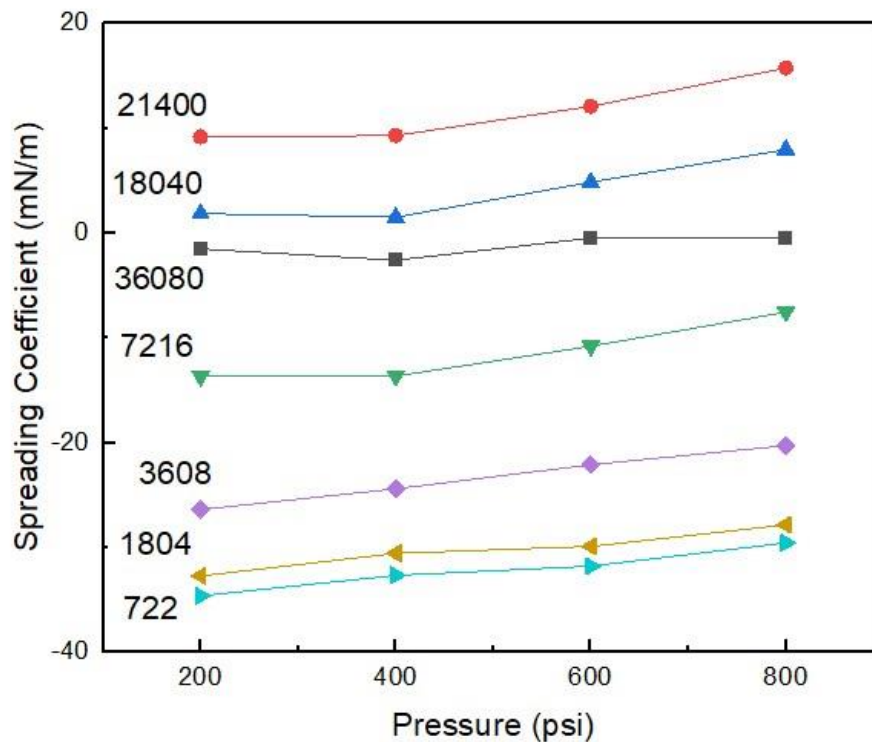


Figure 4.14: Spreading coefficient vs pressure graph for decane without CO₂

Figure 4.14 is presenting all the trendlines for high salinity water to low salinity water spreading coefficient without CO₂ with respect to pressure. From the graph, low salinity (722 ppm) to high salinity water (18040 ppm) has given a negative spreading coefficient. Additionally, from Keller et al. it has been reported that decane has given a negative spreading coefficient whereas, for our wide range of salinity, we also got a positive spreading coefficient for high salinity water (21400 ppm and 36080 ppm) (Keller et al., 1997). This graph is quite revealing in several ways. First, with increasing pressure, all the spreading coefficient values are increasing except 18040 ppm. It can happen 18040 ppm has less effect on pressure where other concentrations are affected by high pressure. Second, the highest spreading coefficient value is for high salinity seawater and the value is 18 mN/m.

4.3.4 Spreading Coefficient of Dulang+Decane with and without CO₂

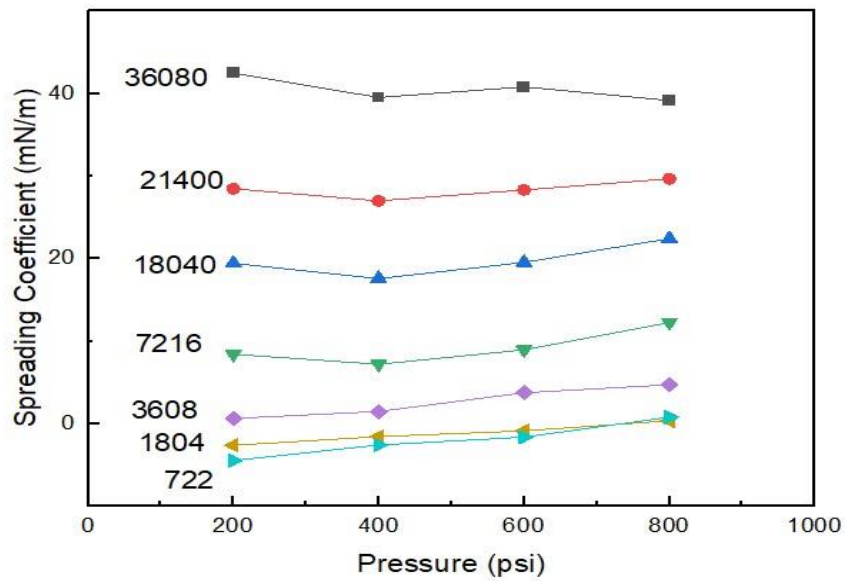


Figure 4.15: Spreading coefficient vs pressure graph for Decane+Dulang with CO₂

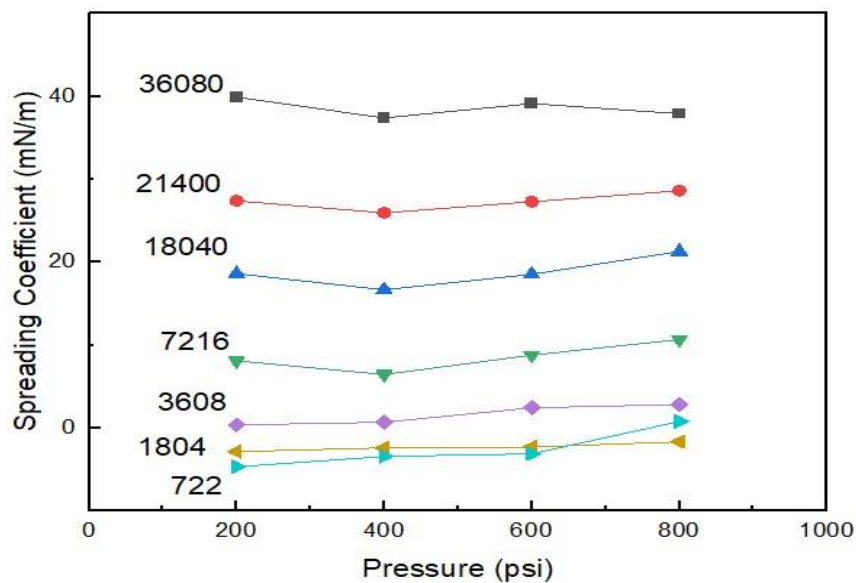


Figure 4.16: Spreading coefficient vs pressure graph for Decane+Dulang without CO₂

In this section, the spreading coefficient of (Decane+Dulang) with and without CO₂ graph has been summarized and reported significant changes due to changes in pressure and brine

salinity. Figure 4.15 and 4.16 is presenting all the trendline for high salinity water to low salinity water spreading coefficient without CO₂ with respect to pressure. Comparing Figures 4.15 and 4.16 it is observed that there is no significant change in spreading coefficient values both for with and without CO₂. All the trendlines are giving similar results for with and without CO₂ conditions which are not usual according to the other results. Further analysis has shown that only for 722ppm at 800psi pressure the value of the spreading coefficient has increased slightly. Moreover, all the spreading coefficient values are increasing with increasing pressure. Surprisingly, the effect of CO₂ is not significant for this oil, salinity, and pressure condition. Most of the salinity is giving a positive spreading coefficient salinity which is giving a positive sign towards more recovery according to the established literature review (Khorshidian et al., 2016; Oren and Pinczewski, 1994).

4.3.5 Discussion from Spreading Coefficient Measurement

From spreading coefficient measurement, both positive spreading coefficient and negative spreading coefficient values are present in this work. For Dulang with and without CO₂, the value of the spreading coefficient has not been reported to date. This work has been presented with all the experimental analyses and discussed with increasing pressure when CO₂ gas is present and absent in the system.

Additionally, decane has given a mostly negative spreading coefficient. The mixture of Dulang and Decane has given positive and negative spreading coefficients together and maximum values are positive. These positive and negative spreading coefficient values are directly depending on the oil/water interfacial tension, gas/oil surface tension, and gas/water surface tension. Moreover, pressure, low salinity water, and CO₂ gas together or individually have played an important role behind these different spreading coefficient values.

From Figures 4.12 to 4.16 we can see that, for some specific pressure, the trendlines are fluctuating and at which point the trendlines are changing, the effect of pressure has been noticeable for that part. For most of the concentrations with increasing pressure, the spreading coefficient values are increasing and shifting towards more positive values, and it is happening due to the more solubility of CO₂ in those brine concentrations. If we notice, then it can be

visualized that some trendlines have not shifted under the presence of CO₂ gas, and no visual change in trendlines with increasing pressure and which is an indication of no effect of pressure and CO₂ in these specific concentrations. It may happen due to less solubility of CO₂ as in Figure 4.15 and Figure 4.16, 1804 ppm for Dulang+Decane mixture spreading coefficient trendline has not changed with pressure and CO₂ gas. Moreover, it has been observed that the CO₂ effect is prominent in these experiments according to the analysis of graphs as the presence of CO₂ has shifted some spreading coefficient trendlines from negative to positive. According to literature reviews, a positive spreading coefficient facilitates more oil films to flow and generate an oil bank by decreasing snap-off and trapped oil (Al-Abri et al., 2019).

4.4 Contact Angle Measurement

In this section, the RSM model for the contact angle of Dulang with and without CO₂ gas has been discussed thoroughly but for other oils (Decane & Dulang+Decane) only the graphical analysis has been presented.

4.4.1 RSM Model for Contact Angle of Dulang with CO₂ and without CO₂ (Water Wet)

After obtaining data from the experimental run with and without CO₂ according to the suggested DOE were added in the predetermined slots for the response as shown in Table 4.10.

Table 4.10: Actual design matrix for Contact angle measurement (Dulang with and without CO₂)

Dulang with CO₂ (water wet)				Dulang without CO₂ (water wet)			
Run	Factor 1 A: concentration Ppm	Factor 2 B: pressure Psi	Response 1 Contact angle degree	Run	Factor 1 A: concentration ppm	Factor 2 B: pressure psi	Response 1 contact angle degree
1	18401	1100	48	1	18401	1100	48
2	18401	1100	46.4	2	722	1100	52
3	18401	200	52	3	18401	1100	59
4	36080	1100	54	4	18401	1100	57
5	18401	1100	56	5	36080	200	51
6	36080	200	48	6	18401	1100	53
7	36080	2000	48	7	18401	200	56
8	722	1100	59	8	36080	2000	45
9	18401	1100	58	9	18401	1100	50
10	18401	2000	50	10	722	200	46
11	722	200	45	11	722	2000	66
12	18401	1100	48.5	12	18401	2000	56
13	722	2000	54	13	36080	1100	58

Table 4.11: Sequential model sum of squares

Dulang with CO ₂					Dulang without CO ₂					
Source	Mean Square	F-value	p-value		Source	Sum of Squares	Mean Square	F-value	p-value	
Mean vs Total	2.212E+05				Mean vs Total	2.010E+05	2.010E+05		0.0072	
Linear vs Mean	199.95	13.99	0.0013		Linear vs Mean	210.1	105.08	8.43	0.026	
2FI vs Linear	0.0000	0.00	1.00		2FI vs Linear	54.76	54.76	7.04	0.0007	
Quadratic vs 2FI	64.49	32.29	0.0003	Suggested	Quadratic vs 2FI	61.29	30.65	24.7	0.863	Suggested
Cubic vs Quadratic	3.11	2.00	0.23	Aliased	Cubic vs Quadratic	0.493	0.246	0.15		Aliased
Residual	1.55				Residual	8.18	1.64			
Total	17053.9				Total	2.014E+05	15489.64			

Table 4.11 represents the suggested model based on DOE and acquired data from the experiment. And RSM suggests a Quadratic model for both. Other models can be used but the accuracy level is very low for those models where the cubic model is aliased for both.

Table 4.12: ANOVA for Quadratic model

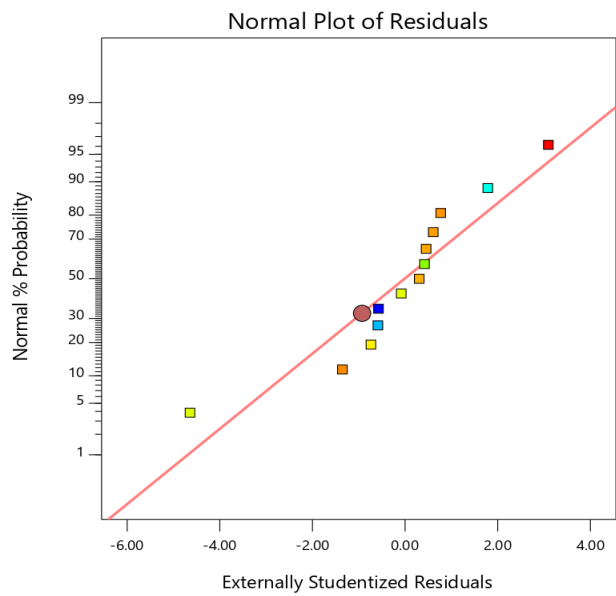
Dulang with CO ₂					Dulang without CO ₂						
Source	Sum of Square	F-value	p-value		Source	Sum of Square	F-value	p-value			
Model	528.89	52.97	0.000	1	significant	Model	326.22	52.64	0.000	1	significant
A-concentration	368.17	184.3	0.000	6		A-concentration	208.86	168.52	0.000	1	
B-pressure	31.74	15.89	0.005	3		B-pressure	1.31	1.05	0.338	7	
AB	0.0000	0.000	1.000			AB	54.76	44.18	0.000	3	
A ²	78.39	39.26	0.000	4		A ²	11.55	9.32	0.018		
B ²	10.26	5.14	0.057			B ²	27.32	22.04	0.002		
Residual	13.98					Residual	8.68				
Lack of Fit	11.47	6.09	0.056	8	not significant	Lack of Fit	5.16	1.95	0.263		not significant

From Table 4.12 we can see that, for Dulang with the CO₂ model, the **Model F-value** of 52.97 implies the model is significant. There is only a 0.01% chance that an F-value this large could occur due to noise. **P-values** less than 0.0500 indicate model terms are significant. The **Lack of Fit F-value** of 6.09 implies there is a 5.68% chance that a Lack of Fit F-value this large could occur due to noise. Lack of fit is bad - we want the model to fit. This relatively low probability (<10%) is troubling. For Dulang without the CO₂ model, the **Model F-value** of 52.64 implies the model is significant. There is only a 0.01% chance that an F-value this large could occur due to noise, **P-values** less than 0.0500 indicate model terms are significant. In this case, A, AB, A², and B² are significant model terms. The **Lack of Fit F-value** of 1.95 implies the Lack of Fit is not significant relative to the pure error. There is a 26.31% chance that a Lack of Fit F-value this large could occur due to noise. Non-significant lack of fit is good - we want the model to fit.

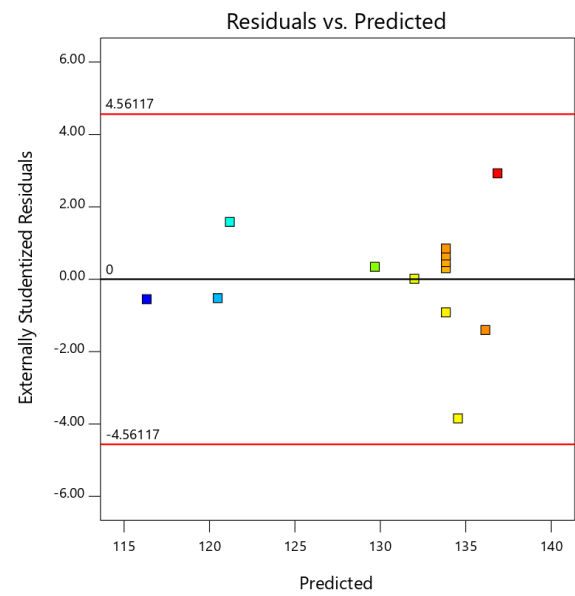
Table 4.13: Fit Statistics

Dulang with CO ₂				Dulang without CO ₂			
Std. Dev.	1.41	R²	0.9742	Std. Dev.	1.11	R²	0.9741
Mean	130.43	Adjusted R²	0.9559	Mean	124.35	Adjusted R²	0.9556
C.V. %	1.08	Predicted R²	0.8108	C.V. %	0.8952	Predicted R²	0.8748
		Model Precision	21.1102			Adeq Precision	25.3864

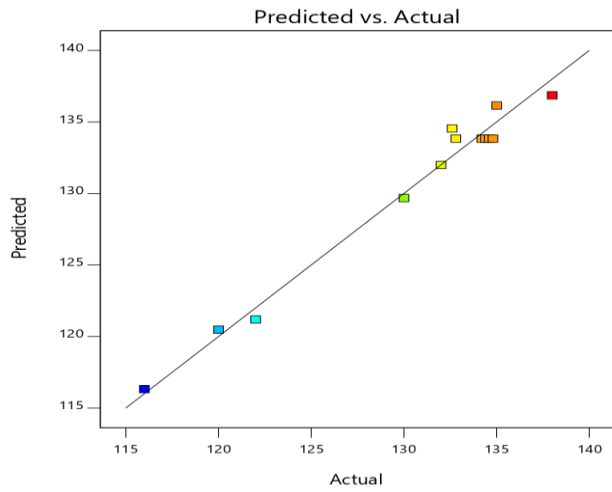
From Table 4.13 we can see that, for Dulang with the CO₂ model, the **Predicted R²** of 0.8108 is in reasonable agreement with the **Adjusted R²** of 0.9559; i.e., the difference is less than 0.2. **Adeq Precision** measures the signal-to-noise ratio. A ratio greater than 4 is desirable. Your ratio of 21.110 indicates an adequate signal. This model can be used to navigate the design space. For Dulang without the CO₂ model, the **Predicted R²** of 0.8748 is in reasonable agreement with the adjusted R² of 0.9556; i.e., the difference is less than 0.2. **Adeq Precision** measures the signal to noise ratio. A ratio greater than 4 is desirable. The ratio of 25.386 indicates an adequate signal. This model can be used to navigate the design space.



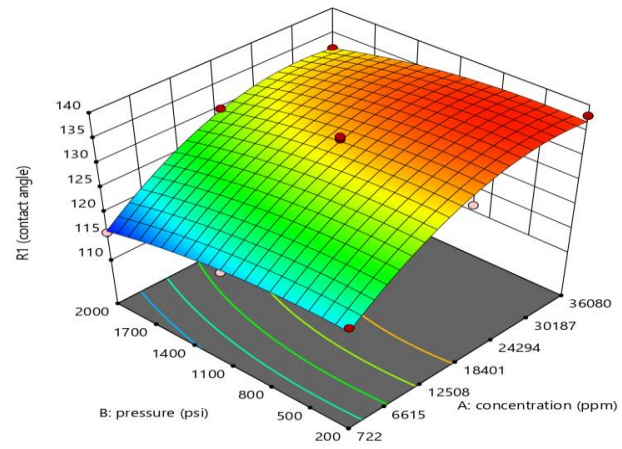
(a) Normal % probability vs residuals



(b) Residuals vs predicted



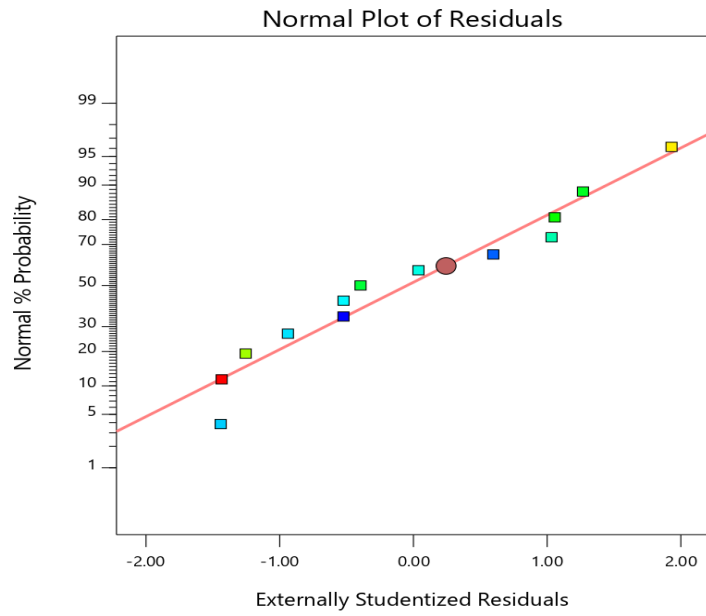
(c) Predicted vs Actual



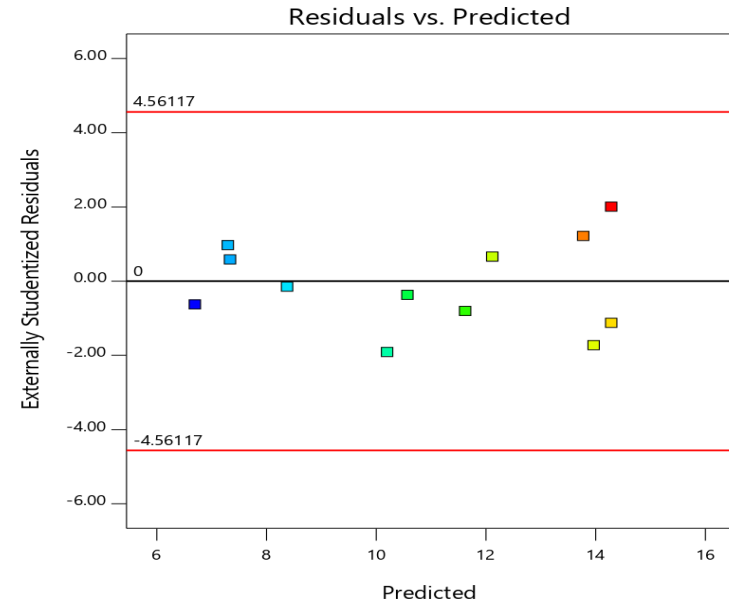
(d) 3D graph

Figure 4.17: Dulang with CO₂ model graphs (a) Normal % probability vs residuals, (b) Residuals vs predicted, (c) Predicted vs Actual, (d) 3D graph

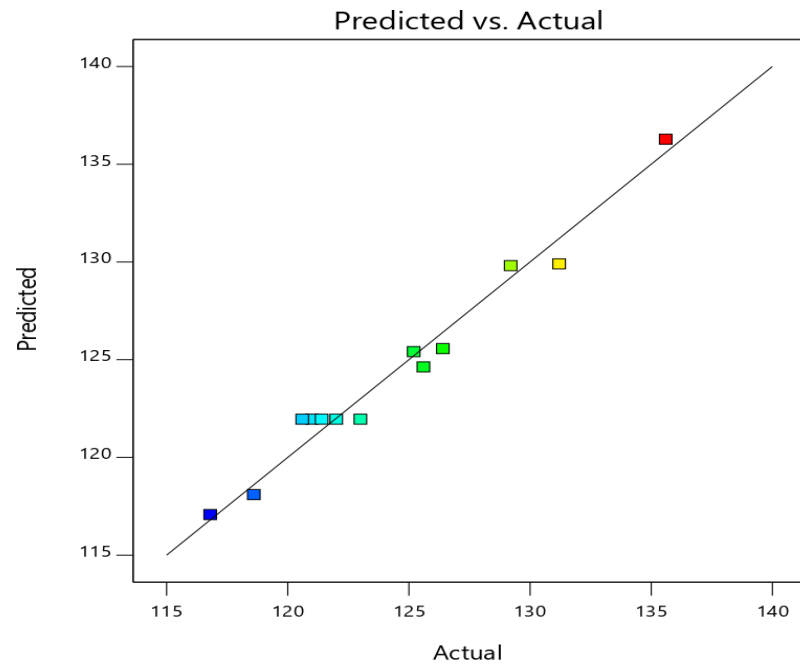
In Figure 4.17, four different types of graphs have been presented where red, green and blue colours are representing the contact angle value range. For blue, green, and red the range of contact angle is respectively 41–50-degree, 50-55 degree and 55-65 degree. 4.7 (a) represents a normal % probability vs residuals graph where all the values are close to the reference line. There is no value which one is very far from the reference line. From 4.17 (b) residual vs predicted graph represents all the values inside the red line. That means there is no noise in these data sets. From 4.17 (c) predicted vs actual values are in the line. So, from these graphs' investigation, we can say that the model is reliable to predict all the values between the maximum and minimum range. This 3D graph in Figure 4.17 (d) represents the synergetic effect of pressure, and concentration on the contact angle (presence of CO₂). From contact angle vs concentration graph represents the contact angle value decreases with the decreasing concentration. The value is highest for 36080 ppm where the contact angle is 59° and for 772 ppm the value for contact angle decreases to 48°. That means wettability shifts towards more wetting phase. Also, with increasing pressure contact angle values decreases very slightly. The simultaneous effect of concentration and pressure represented with increasing pressure and concentration contact angle also increases for Dulang with CO₂ contact angle.



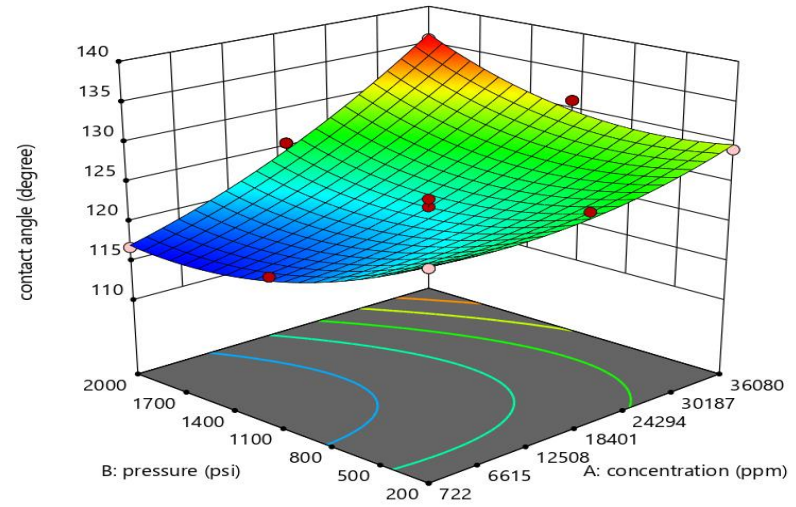
(a) Normal probability vs residuals



(b) Residuals vs Predicted



(c) Predicted vs actual



(d) 3D graph

Figure 4.18: Dulang without CO₂ model graphs (a) Normal % probability vs residuals, (b) Residuals vs predicted, (c) Predicted vs Actual, (d) 3D graph

In Figure 4.18, four different types of graphs have been presented where red, green and blue colors are representing the contact angle value range. For blue, green, and red the range of contact is respectively 50–55-degree, 55-65 degree and 65-75 degree. (a) represents a normal % probability vs residuals graph where all the values are close to the reference line. There is no value which one is very far from the reference line. From 4.18(b) residual vs predicted graph represents all the values inside the red line. That means there is no noise in these data sets. From 4.18(c) predicted vs actual values are in the line. So, from these graphs' investigation, we can say that the model is reliable to predict all the values between the maximum and minimum range. This 3D graph in Figure 4.18(d) represents the synergetic effect of pressure, and concentration on the contact angle (presence of CO₂). From contact angle vs concentration graph represents the contact angle value decreases with the decreasing concentration. The value is highest for 36080ppm where the contact angle is 129.7° and for 772 ppm the value for contact angle decreases to 118°. That means wettability shifts towards water wet where 118° is itself represents, in water-wet surface Dulang without CO₂ behaves like a non-wetting fluid but incomplete wetting condition. Also, with increasing pressure contact angle values decreases very slightly. After 1100psi, the value of the contact angle slightly starts increasing. The simultaneous effect of concentration and pressure represented with increasing pressure and concentration contact angle also increases for Dulang without CO₂ contact angle. Because of the simultaneous effect, the contact angle value changes only from 65° to 61°. So, the alteration for Dulang with CO₂ is more drastic and prominent.

4.4.2 Visual observation of Contact angle

In this work, contact angle measurement has been carried out with IFT700 equipment and then an image analysis has been done using ImageJ software to validate the result from IFT700. In this section, the change in contact angle for decane and Dulang with and without CO₂ at oil-wet and water-wet conditions with respect to pressure has been presented in table 4.14 and 4.15. The contact angle for decane oil-wet, Decane+Dulang oil-wet, and Decane+Dulang oil wet contact angle vs pressure has been discussed in the following subsection. In Table 4.14, for 722 ppm salinity, with increasing pressure, the contact angle has increased from 140 degrees to 143 degrees. The value of the contact angle is shifting toward the more non-wetting

state. Also, for 18040 ppm salinity, the value of contact angle has been shifted from 136 degrees to 147 degrees and this shifting of contact angle is representing the effect of pressure in the system and the same shifting observed for high salinity water. During the experiment, it has been observed that with increasing pressure the area of the oil bubble has been decreased as well as the stability of the oil bubble increased under high pressure. Moreover, the angle of oil with Berea rock slice has decreased under high pressure.

Table 4.14: Contact angle calculation with IFT700 and ImageJ for Decane and Dulang with and without CO₂ oil wet

Samples	Brine concentration	Run	Pressure	IFT700 Left angle	IFT700 Right angle	Image J Left angle	Image J Right angle
Decane with CO ₂ water wet	722 ppm	1	200	140.8	138.3	142	138.625
		2	1100	140.8	140.8	141.09	141.09
		3	2000	143.2	141.5	144.5	144.03
	18040 ppm	4	200	136	145.4	145.8	146.1
		5	1100	145	146.3	148.1	147.9
		6	2000	147	135.2	150	149.1
	36080 ppm	7	200	138	137.6	137.7	138.1
		8	1100	142	137.8	143	138
		9	2000	150.3	149.4	148	149
Decane without CO ₂ water wet	722 ppm	10	200	148	148	145.4	144.7
		11	1100	147	146.2	147.6	146.4
		12	2000	146	148	152	149
	18040 ppm	13	200	129	130	129	129.2
		14	1100	121	122	120.2	122.5
		15	2000	122	122	122.5	122
	36080 ppm	16	200	136	136	136	135
		17	1100	136	135	135.2	134.1
		18	2000	134	133.2	133.2	133.4
722 ppm	19	200	142	142.5	141	141.6	
	20	1100	141.8	141.6	141	141.1	
	21	2000	140.2	140.1	139	140	
Dulang with CO ₂	18040 ppm	22	200	138	138.5	138	139
		23	1100	137.8	137.3	137	137.3
		24	2000	137.1	137.9	136	137.1
	36080 ppm	25	200	136	136.6	136	135

water		26	1100	137	137.8	137	138
wet		27	2000	134	134.2	134	135
	722ppm	28	200	148	147	147.4	146
		29	1100	148.2	148	147.2	147
		30	2000	147.8	146.6	146.8	146
	18040 ppm	31	200	147	147.3	146	147
Dulang		32	1100	146.4	146.1	146.8	146.3
without		33	2000	146	145.6	146.4	145
CO ₂	36080 ppm	34	200	145	144.6	145.6	144
water		35	1100	143	143.6	143.8	143
wet		36	2000	138	138.6	138.7	138

Table 4.15: Contact angle calculation with IFT700 and ImageJ for Decane and Dulang with and without CO₂ water wet

Samples	Brine concentration	Run	Pressure	IFT700 Left angle	IFT700 Right angle	Image J Left angle	Image J Right angle	
Decane with CO ₂ water wet	722 ppm	1	200	40	41	42	42.625	
		2	1100	38	37.8	36.09	35.09	
		3	2000	36.8	41.5	44.5	44.03	
	18040 ppm	4	200	48.1	48.4	49.8	46.1	
		5	1100	42.4	43.3	42.1	43.9	
		6	2000	46	45.2	44.2	44.7	
		36080 ppm	7	200	52	52.6	57.7	57
			8	1100	49	48.8	46	46.9
			9	2000	47	44.4	45	44
Decane without CO ₂ water wet	722 ppm	10	200	42.2	42.8	42	42.4	
		11	1100	40.8	40	40.8	40.5	
		12	2000	38	39.8	40	40.6	
	18040 ppm	13	200	44.9	44	46	46	
		14	1100	37	37.4	40	42.5	
		15	2000	41	42	41.6	42.4	
		36080 ppm	16	200	52.7	53	53.8	53.5
			17	1100	47	45	45.2	44.1
			18	2000	46	46.2	48.2	49.4
Dulang with CO ₂ water wet	722 ppm	19	200	49	52.5	52	53	
		20	1100	48	41.6	46	42.1	
		21	2000	46	46.5	44.4	44.2	
	18040 ppm	22	200	44	48.5	48	49	
		23	1100	42.8	37.3	37	37.3	
		24	2000	40.1	40.9	40	40	
		36080 ppm	25	200	52	46.6	46	45

		26	1100	45	47.8	47	48
		27	2000	48	48.2	47	47.8
Dulang	722ppm	28	200	58	57	57.4	56
without		29	1100	54.2	58	47.2	47
CO ₂		30	2000	52	56.6	56.8	56
water	18040 ppm	31	200	63	63.3	66	67
wet		32	1100	56.4	56.1	56.8	46.3
		33	2000	54	54.6	56.4	55
	36080 ppm	34	200	66	64.6	60.6	64
		35	1100	60	63.6	63.8	63
		36	2000	58	58.6	58.7	58

4.4.3 Contact Angle vs Concentration at Reservoir Condition (Water Wet)

The interaction graph for the contact angle of Dulang, Decane and Dulang+ Decane with CO₂ and without CO₂ at water-wet condition has been presented in Figure 4.19. Here, the dark blue bar is for the contact angle of Dulang, Decane and Dulang+Decane at 722ppm with and without CO₂ and light blue bar is representing the contact angle of Dulang, Decane and Dulang+Decane at 36080 ppm with and without CO₂ at reservoir condition. From Table 4.15, with increasing pressure, contact angle is decreasing for different salinity water. At 200 psi pressure, for high salinity water the contact angle values are higher than low salinity water and the values are shifting towards more wetting state. For low salinity water, the shifting of contact angle is prominent whereas a slight alteration has happened for high salinity water. The effect of CO₂ is also visible in this graph. When CO₂ is not present in the system the contact angle values are higher for both low salinity water and high salinity water than the system with CO₂.

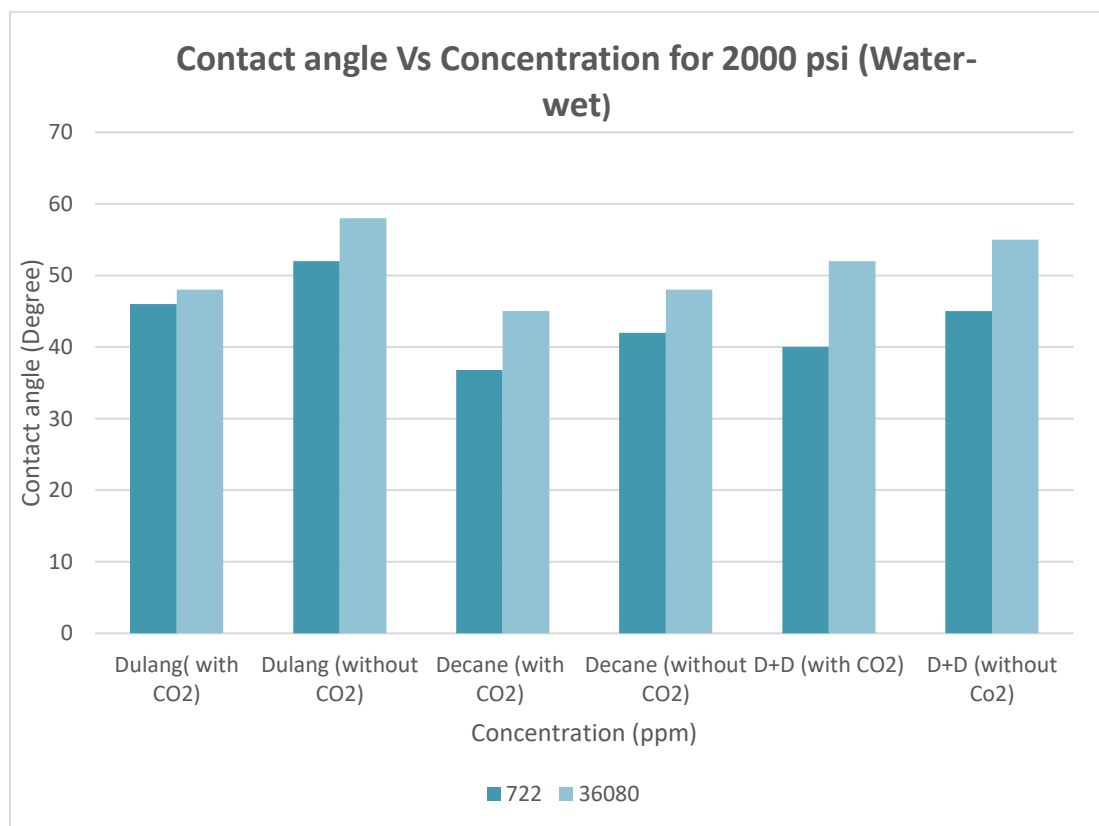


Figure 4.19: Contact angle vs concentration at reservoir condition in water-wet rock

In Graph 4.19, at reservoir condition, all the contact angle values are less than 90 degrees. For different pressure, brine salinity, oil, presence and absence of CO₂ gas, the contact angle values has been changed in a noticeable way. For Dulang with CO₂, 722ppm salinity has given less contact angle value than 36080ppm. From the same graph, when CO₂ is not present in the system with Dulang oil, both salinities has given higher contact angle values than the system without CO₂. Whereas high salinity water has given slightly higher contact angle values than low salinity. The presence of CO₂ helped to alter the wettability for low salinity towards more wetting phase which is indicating low salinity water has better wettability shifting ability than high salinity water. Also, for Decane, from table 4.15 it can be stated that at reservoir temperature and pressure when CO₂ is present in the system the contact angle value is less than the system has no CO₂. Whereas with increasing pressure the contact angle value decreases and wettability has shifted to more water-wet condition. The effect of CO₂ is prominent for both oil and wettability shifting towards wetting phase is also visible. At reservoir condition, decane has shifted towards more water-wet wetting system where the value of contact angle is lower for the system with CO₂. Additionally, though Dulang is a waxy crude but due to high temperature and pressure, the value of contact angle is slightly higher than decane. From Dulang+Decane with and without CO₂, contact angle values has shifted like Dulang and Decane oil. The effect of low salinity water and CO₂ is prominent and visible during wettability alteration.

4.4.4 Contact angle vs Concentration at Reservoir Condition (Oil Wet)

The interaction graph for the contact angle of Dulang, Decane and Dulang+ Decane with CO₂ and without CO₂ at oil-wet condition has been presented in Figure 4.20. Here, the dark blue bar is for the contact angle of Dulang, Decane and Dulang+Decane at 722ppm with and without CO₂ and light blue bar is representing the contact angle of Dulang, Decane and Dulang+Decane at 36080 ppm with and without CO₂ at reservoir condition. From Table 4.15, with increasing pressure, contact angle is decreasing for different salinity water. At 200 psi pressure, for high salinity water the contact angle values are higher than low salinity water and the values are shifting towards more wetting state. For low salinity water, the shifting of contact angle is prominent whereas a slight alteration has happened for high salinity water. The effect

of CO₂ is also visible in this graph. When CO₂ is not present in the system the contact angle values are higher for both low salinity water and high salinity water than the system with CO₂. From this table it is visible that the contact angle values are higher than the values of contact angle for water-wet condition and all the values are more than 90 degrees.

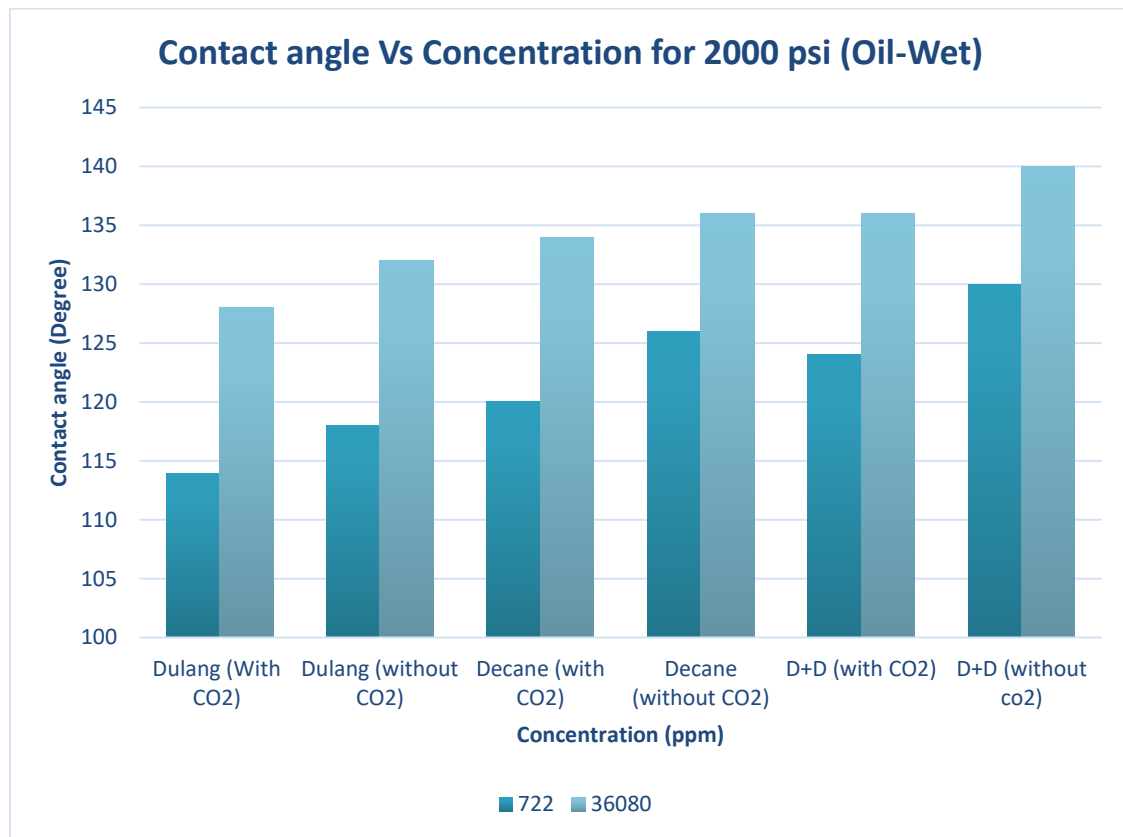


Figure 4.20: Contact angle vs concentration at reservoir condition in oil-wet rock

From Graph 4.20, for 722ppm Dulang with CO₂ it has been noticed that low salinity water has been altered towards water wet whereas high salinity water has given higher contact angle and shifted towards more oil-wet state. At reservoir condition, Dulang, decane and Dulang+Decane oils contact angle is lower for low salinity water and it shifted towards more water-wet state. This scenario is common for all the high salinity bar. For 722ppm salinity with decane oil, it can be seen that the value of contact angle is 120 degrees where for 36080 ppm its 132 degrees. The change in contact angle due to salinity difference is visible in this graph. Moreover, in decane with CO₂, for 722 ppm and 36080 ppm the contact angle values are respectively 120 degrees and 132 degrees. Additionally, in decane without CO₂ system, for 722

ppm and 36080 ppm the contact angle values are respectively 127 degrees and 137 degrees. The increase in contact angle value and the effect of CO₂ is visible in the graph. The effect of CO₂ is prominent for each oil and wettability shifting towards water-wet is also visible in Figure 4.20.

4.4.5 Discussion from Contact Angle Measurement

From the contact angle experiment, it can be stated that low salinity water and pressure is the most influential factor in altering the wettability where CO₂ gas has played as a minor factor. Though the simultaneous effect of CO₂ gas and pressure has altered the wettability significantly.

From this investigation, it has been observed that for low salinity water, with increasing pressure the trendlines are shifting towards a water-wet system when CO₂ gas is present. Under high pressure, the solubility of CO₂ in brine has increased in a noticeable way which has worked as a major factor to alter the wettability of the water-wet system. Though in some cases only the effect of CO₂ gas is visible. As an example, in Figure 4.20 contact angle for the low salinity water trendline has changed with pressure and the contact angle has altered toward more wetting phase, and between these two analyses, the only presence of CO₂ made this significant change. Based on the degree of solubility of CO₂ gas in any brine salinity plays an important role to alter the wettability. Moreover, wettability alteration towards water wet is desirable according to other work and it helps to increase the overall recovery (Al-Abri et al., 2019; AlQuraishi et al., 2019).

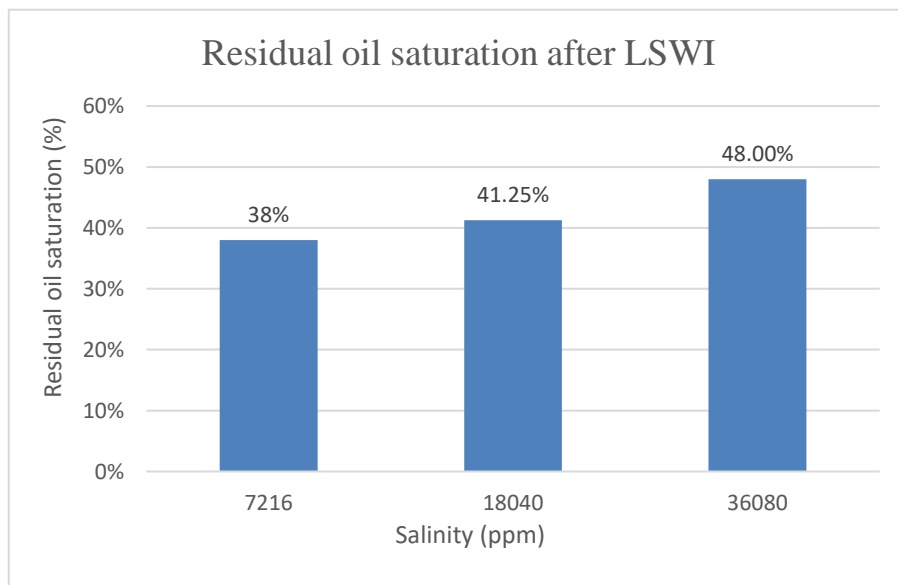
This wettability alteration may happen based on some mechanisms, such as fine migration, multi-component ion exchange, and electrical double layer effect. From another analysis, any of these mechanisms can be an influential factor towards wettability alteration though it is very difficult to analyze and visualize the effects of such an experiment. According to another analysis, the water-wet system with low salinity water facilitates more recovery according to the finding and it may happen due to the attraction of the water phase towards the large pores occupying them which decreases the amount of oil occupied by other pores as well as decreases

residual oil saturation. An oil bank has been observed for both water-wet and oil-wet conditions when the salinity is low, and this part has been discussed in the next part extensively.

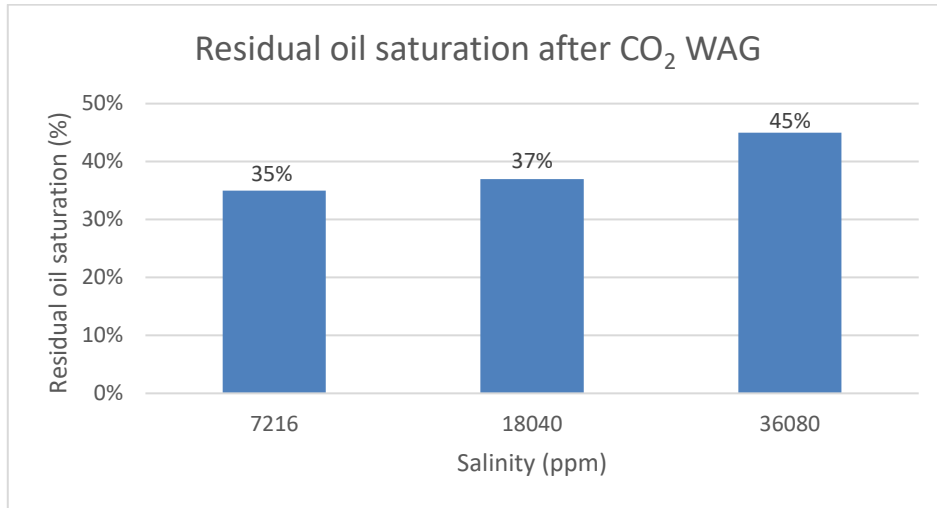
4.5 HPHT micromodel for pore-scale visualization of LSWACO₂

In this section, pore-scale calculation and related graphs have been analyzed to find out the factors contributing to enhanced oil recovery. To calculate the area of fluid inside the micromodel we used ImageJ software and further volume calculation has been conducted using MS Excel. A critical analysis of fluid movement and distribution has been described broadly to clarify the effect of salinity, spreading coefficient, and pressure.

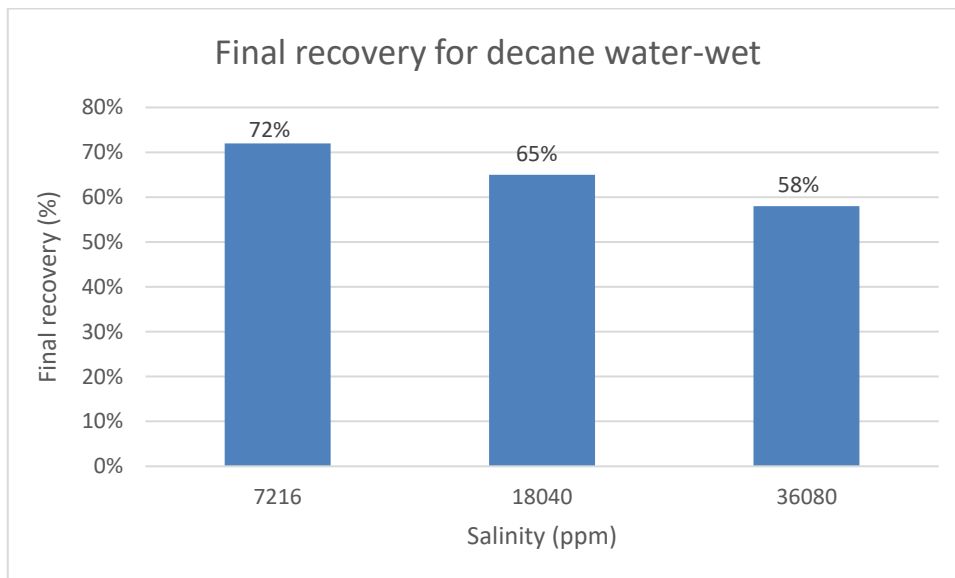
4.5.1 Enhanced Oil Recovery for Decane Water Wet Condition



(a)



(b)



(c)

Figure 4.21: Graphical analysis of Enhanced oil recovery for decane water wet (a) Residual oil saturation after low sal (b) Residual oil saturation after CO₂ WAG (c) Final Recovery for decane water-wet

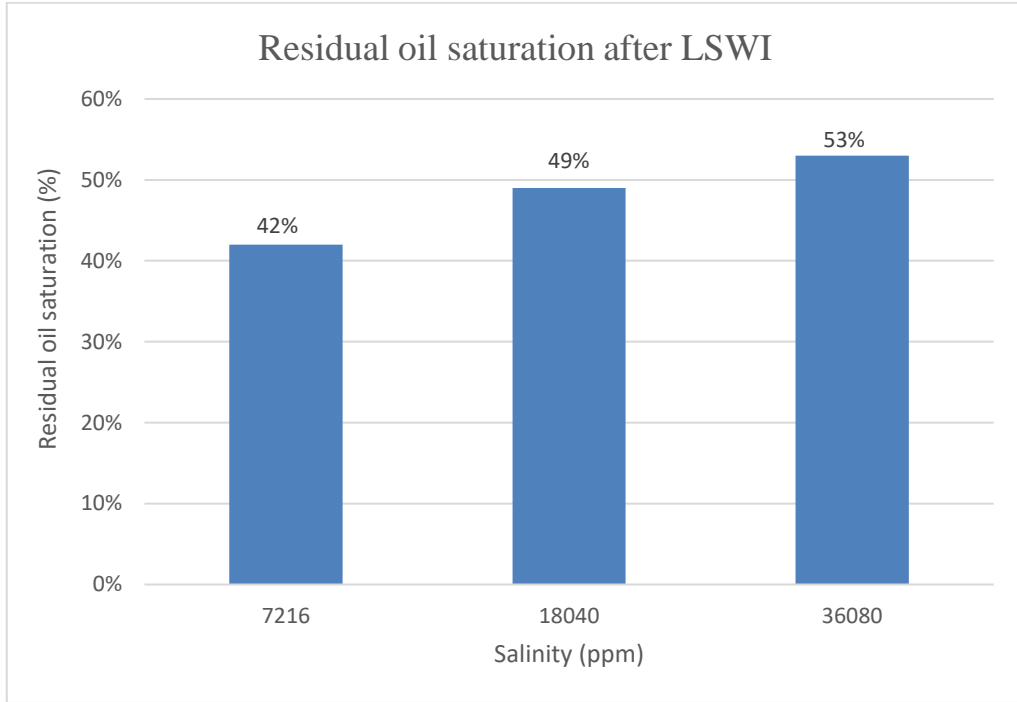
A graphical analysis of recovery for 7216 ppm, 18040 ppm, and 36080 ppm has been presented in the following graph. Initially flushing the micromodel with 21400ppm to establish the initial water saturation, then flushed it with the oil phase. To get the residual oil saturation

after LSWF, oil phase has been flushed with 722ppm salinity brine. After that, CO₂ has been injected into the system to decrease the residual oil saturation. After a consecutive injection of brine and CO₂ gas, the final recovery has been recorded. During the WAG cycle, three types of brine concentration such as 7216 ppm, 18040 ppm, and 36080 ppm, and two types of oil such as, decane and Decane+Dulang mixture have been used respectively to analyze the effect of salinity, contact angle, and spreading coefficient in the recovery process. From Figure 4.30 (a) we can see that after the low salinity water flood stage, residual oil saturation has been calculated and for 7216 ppm the value of residual oil saturation is 38%. Residual oil saturation for 18040 ppm and 36080 ppm is respectively 41.25% and 48%. From here it can be stated that the residual oil saturation is high for high salinity water and low for low salinity water. For 7216 ppm, the spreading coefficient value is negative but due to low salinity and water-wet condition, it has given a great recovery after the low salinity water injection. Eventually, 36080ppm and 18040ppm have a positive spreading coefficient, and the wetting state is water wet but due to high salinity, it is not giving high recovery like 7216 ppm salinity.

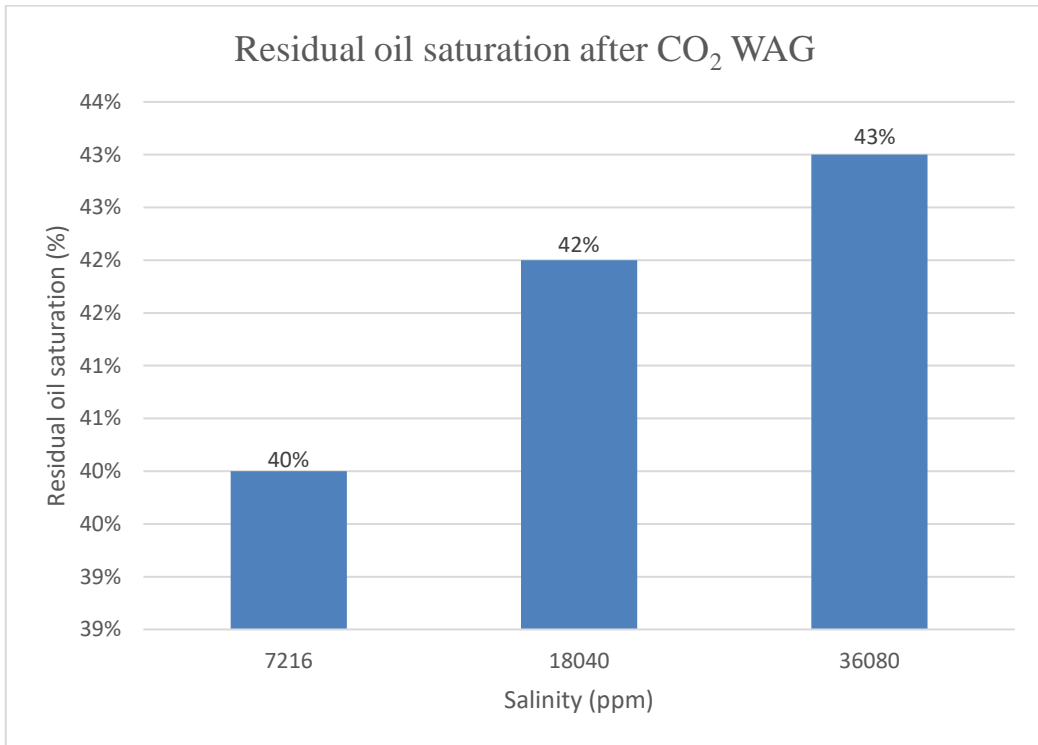
From Figure 4.30 (b) after CO₂ WAG, the residual oil saturation has decreased for all the salinity regardless of the fluid system's positive spreading coefficient or negative spreading coefficient. For 7216 ppm salinity, residual oil saturation has been decreased to 35% through a very small change in recovery. Furthermore, for 18040 ppm and 36080 ppm the residual oil saturation is 37% and 45% whereas, for both salinity, recovery increased noticeably. This may happen due to the effect of CO₂ and positive spreading coefficient, although this point, we suggest further investigations need to be conducted to explain the effect when subjected to different wetting conditions and salinity.

After continuous injection of water alternating gas, the final recovery has been calculated and it is shows that low salinity water is giving the highest recovery at 72% followed by 18040 at 65% final recovery and finally 36080 ppm has given 58%.

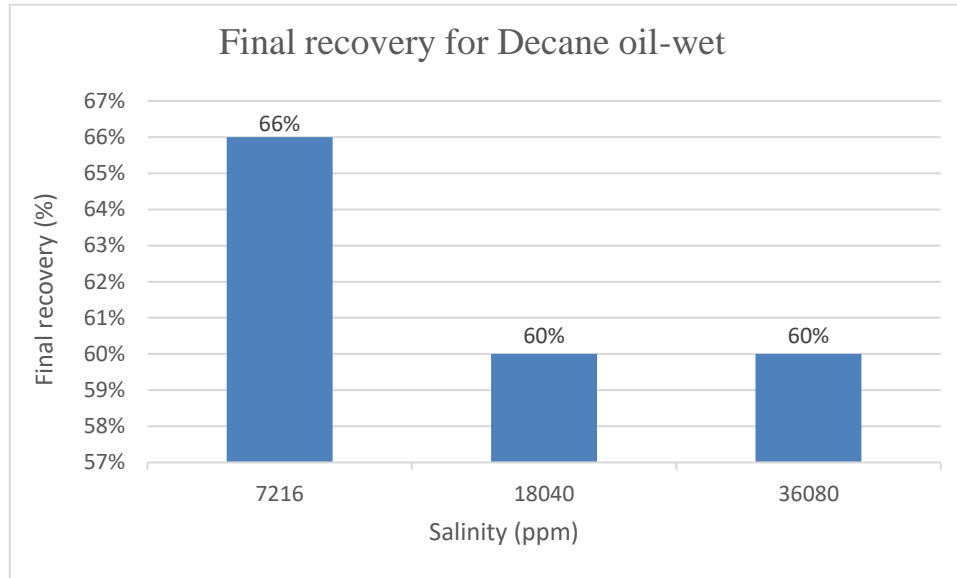
4.5.2 Enhanced Oil Recovery for Decane Oil-Wet Condition



(a)



(b)



(c)

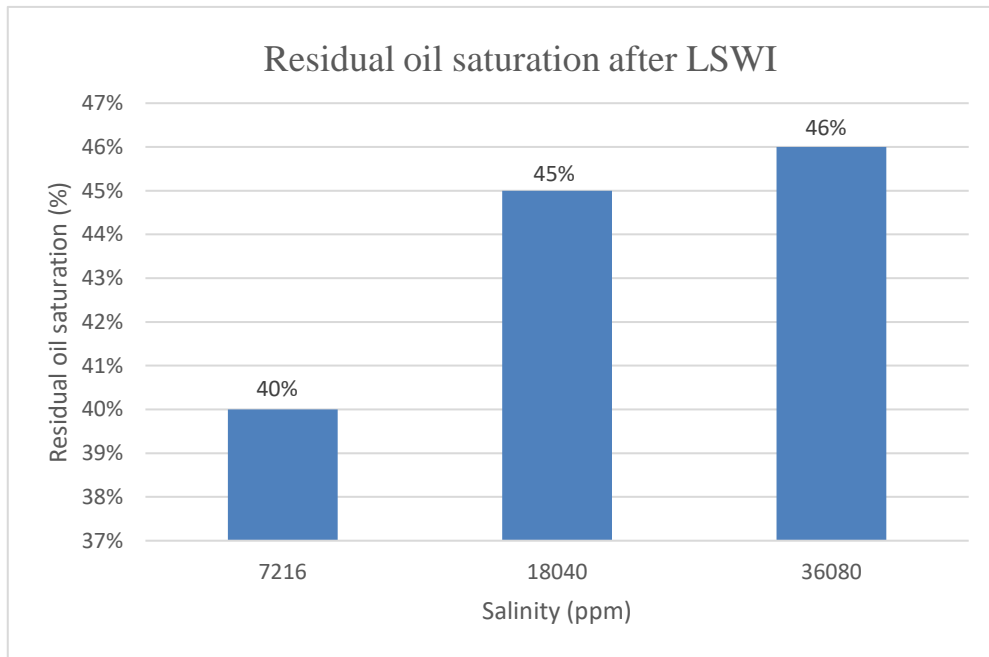
Figure 4.22: Graphical analysis of Enhanced oil recovery for decane oil-wet (a) Residual oil saturation after low sal (b) Residual oil saturation after CO₂ WAG (c) Final Recovery of decane oil-wet

A graphical analysis of recovery for 7216 ppm, 18040 ppm, and 36080 ppm for decane oil-wet conditions has been presented in the following graph. Figure 4.22 represents enhanced oil recovery for decane oil wet (a) Residual oil saturation after low salinity water flood (b) Residual oil saturation after CO₂ WAG (c) Final Recovery of decane oil wet. In Figure 4.22 (a) we can see that for low salinity water, residual oil saturation is lower than in high salinity water and seawater. Residual oil saturation is respectively 42%, 49%, and 53%. For low salinity water, the spreading coefficient is negative according to our previous finding and the wetting condition is oil-wet. Due to the negative spreading coefficient and oil-wet condition the primary residual oil saturation is higher than in the water-wet condition as from the previous finding we got water-wet condition gives better wettability alteration than the oil-wet condition. For 18040 ppm and 36080 ppm, these salinities have given a positive spreading coefficient but due to the wetting condition and high salinity, these are giving more residual oil saturation than the water-wet condition. From this analysis, it is clear that wettability and salinity are playing a role as major factors whereas the spreading coefficient is playing a minor factor.

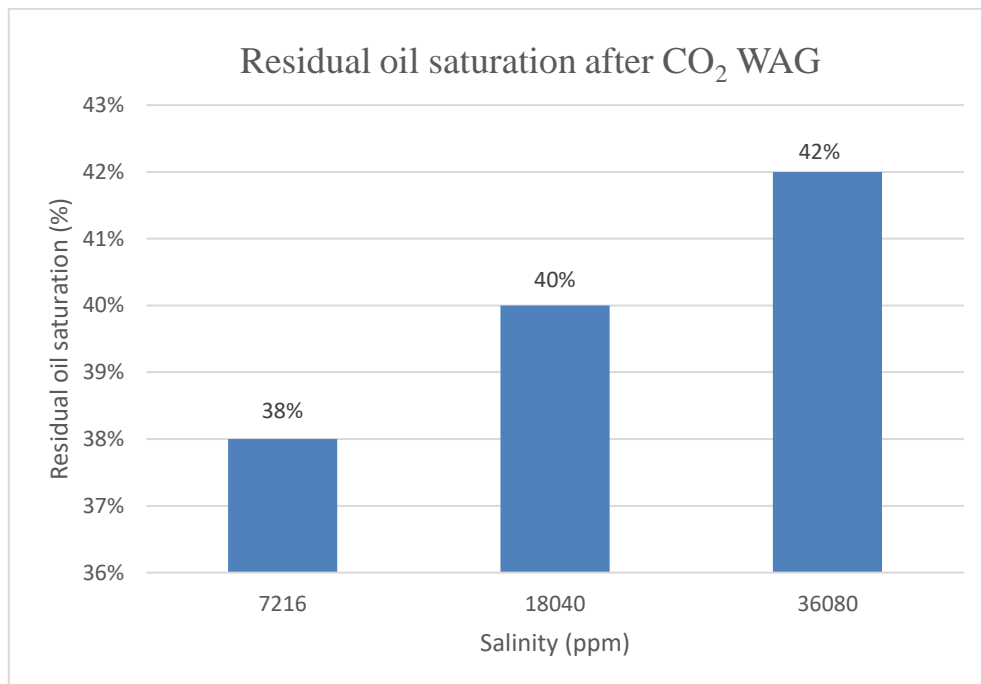
In Figure 4.22 (b) the oil saturation after CO₂ WAG has been presented with graphical analysis. Here, we can see that the residual oil saturation has decreased for all three concentrations, and respectively it is 40%, 42%, and 46% after flushing with CO₂. The oil saturation has not decreased significantly. It can happen for two reasons; the first is due to the negative spreading coefficient, and the second is the oil-wet condition. According to Oren et al. and Khorshidian et al., a negative spreading coefficient could not facilitate the thin oil film flow to form a big oil bank which will increase the further oil recovery. Moreover, the oil-wet condition has been considered a negative factor during oil recovery. In addition, for high salinity water residual oil saturation decreased noticeably and it may happen due to a positive spreading coefficient.

In Figure 4.22 (c) the final recovery has been presented for low salinity water and high salinity water after a consecutive run of brine and CO₂. The final recovery is 66% for low salinity water and 60% for high salinity water and seawater. Although the spreading coefficient is negative, and the wetting condition is oil-wet for low salinity water, it is giving the highest recovery. It can be happened due to the low salinity water condition and the recovery is lower than in water wet conditions. So, it can be stated that low salinity water with water condition is a major factor behind higher recovery where spreading coefficient is playing a minor role behind it.

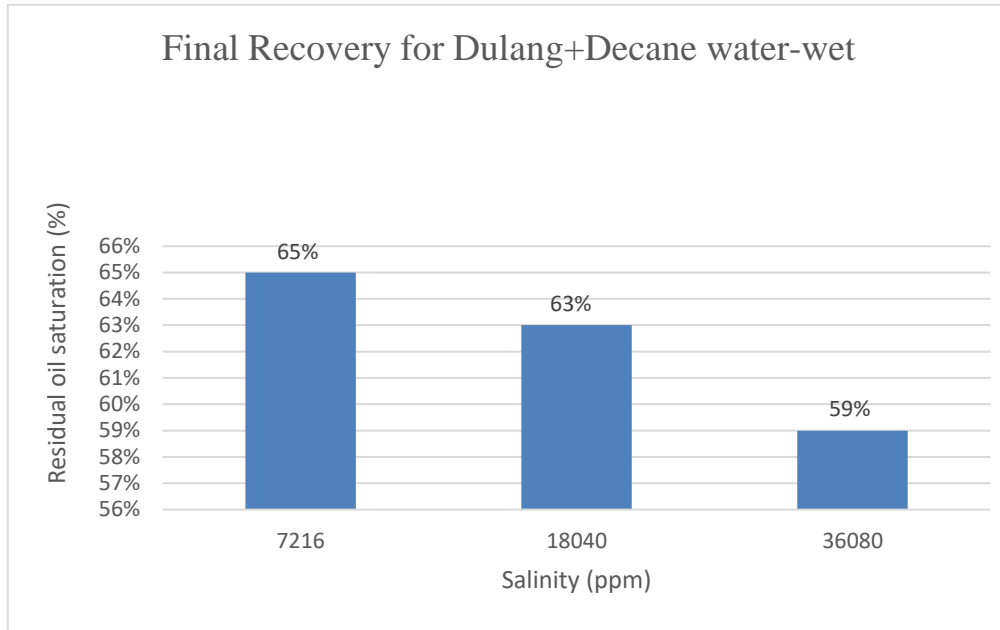
4.5.3 Enhanced Oil Recovery for Decane+Dulang Water Wet Condition



(a)



(b)



(c)

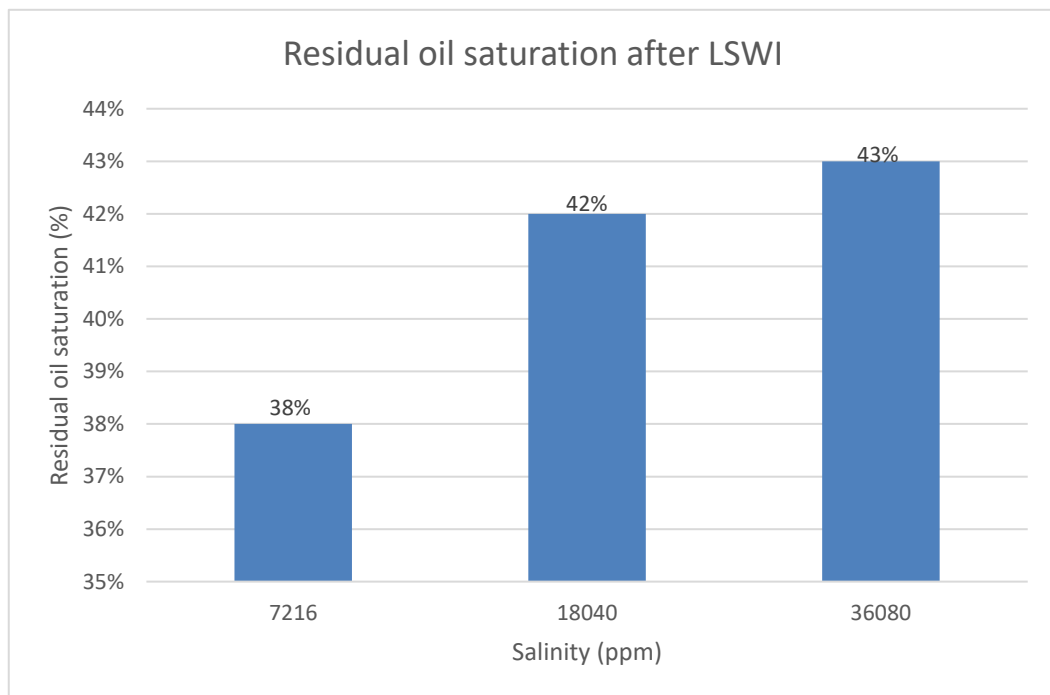
Figure 4.23: Graphical analysis of Enhanced oil recovery for Dulang+Decane water-wet (a) Residual oil saturation after low sal (b) Residual oil saturation after CO₂ WAG (c) Final Recovery of Decane+Dulang water-wet

A graphical analysis of recovery for 7216 ppm, 18040 ppm, and 36080 ppm for Decane+Dulang water-wet condition has been presented in the following graph. Figure 4.23 represents enhanced oil recovery for Decane+Dulang water wet (a) Residual oil saturation after low salinity injection (b) Residual oil saturation after CO₂ WAG (c) Final Recovery of Decane+Dulang water wet. In Figure 4.23 (a) the residual oil saturation for low salinity water is 38% and for high salinity water and seawater, it is 42% and 43%. For both (18040 ppm and 36080 ppm) high salinity water, the residual oil saturation is almost the same. For these three salinities, all have given a positive spreading coefficient.

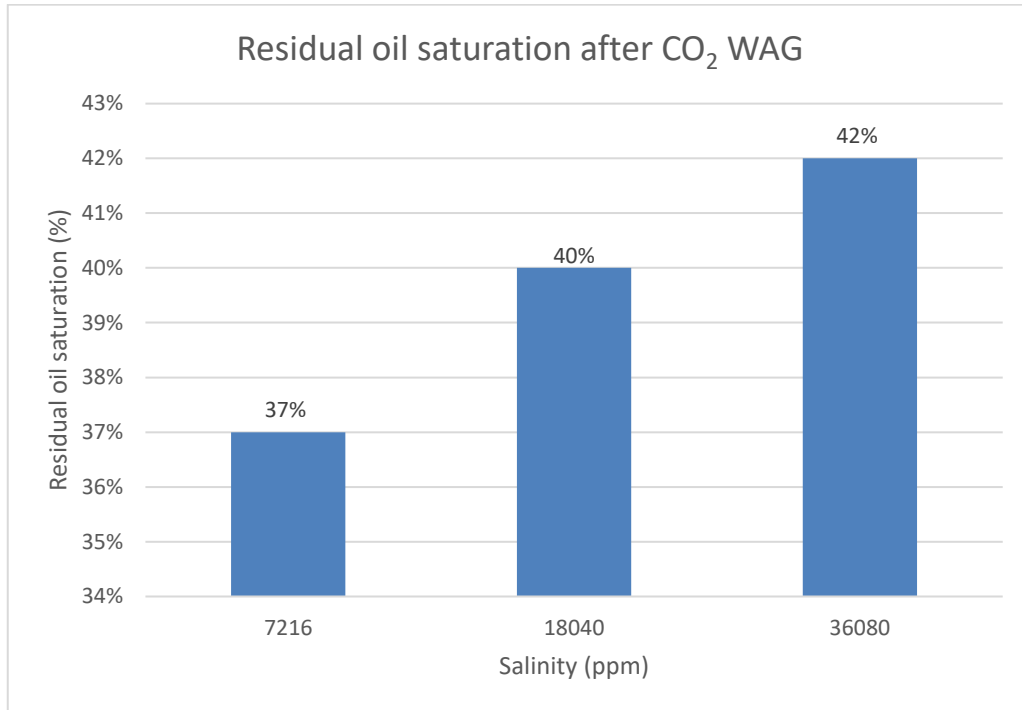
After CO₂ WAG, Figure 4.23 (b) shows the residual oil saturation has decreased slightly for the low salinity water and high salinity water. The slight decrease in residual oil after CO₂ WAG can be attributed to a higher density of the Decane+Dulang oil mixture. This consequently restricted injected fluids (brine, CO₂ gas) to move the oil phase.

From Figure 4.23 (c), the final recovery after the consecutive flush of brine and CO₂ is shown. The final recovery for low salinity water is 65% and high salinity water and seawater is 63% and 59%. Eventually, the results have shown low salinity water has given more recovery than high salinity water and seawater for Dulang+Decane water-wet system.

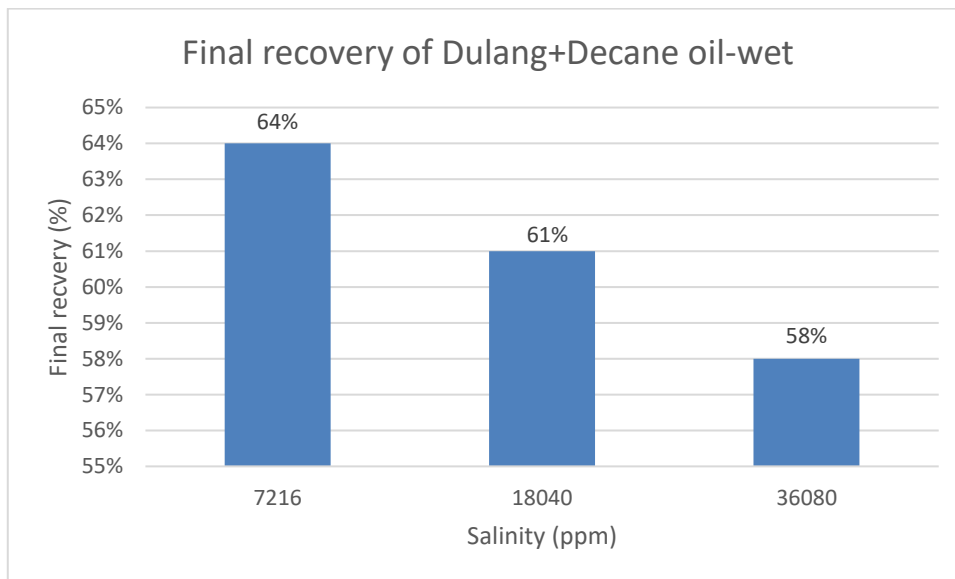
4.5.4 Enhanced oil Recovery for Decane+Dulang Oil Wet Condition



(a)



(b)



(c)

Figure 4.24: Graphical analysis of Enhanced oil recovery for Dulang+Decane oil-wet (a) Residual oil saturation after low salinity (b) Residual oil saturation after CO₂ WAG (c) Final Recovery of Decane+Dulang oil-wet

A graphical analysis of recovery for 7216 ppm, 18040 ppm, and 36080 ppm for Decane+Dulang oil-wet condition has been presented in the following graph. Figure 4.24 represents enhanced oil recovery for Decane+Dulang water wet (a) Residual oil saturation after low salinity water flood (b) Residual oil saturation after CO₂ WAG (c) Final Recovery of Decane+Dulang oil wet. In Figure 4.24 (a) the residual oil saturation for low salinity water is 40% and for high salinity water, it is 45% and 46% respectively. For low salinity water, the residual oil saturation in oil-wet (40%) is higher than in water-wet (38%) conditions.

Figure 4.24 (b) is representing oil saturation after CO₂ flush and for low salinity water, the residual oil saturation is 38%. The residual oil recovery decreased by only 2% more than the previous low salinity water flood. It can be happened due to the density of Dulang+Decane and oil-wet conditions. For high salinity water, the residual oil saturation decreased significantly (45% after LSWF to 40% after CO₂ WAG for 18040 ppm) but overall, it is still higher compared to residual oil for low salinity brine after CO₂ WAG. The same can be said for 36080 ppm brine.

In Figure 4.24 (c) the final recovery has been presented and the recovery is slightly higher for low salinity water (64%). The trend of final recovery is similar for both water-wet and oil-wet condition with Dulang+Decane mixture. Namely more recovery is expected as the salinity is decreasing. The results presented here will be further discussed in the next section.

4.5.5 Discussion from Enhanced Oil Recovery Calculation

From all these result analyses and recovery calculations, it has been observed that the recovery values are changing based on three factors. These three factors are wettability, brine salinity, and spreading coefficient where water-wet condition, low salinity water, and positive spreading coefficient have been considered positive factors. In Table 4.16 the positive sign (+) has been considered a positive factor toward more recovery and the negative sign (-) has been considered a negative factor. Moreover, it is easy to detect the major and minor factors from the Table. For decane water-wet, when the salinity is low salinity all the factors are affected positively, and the overall recovery is higher than in any other system. For high salinity water, the recovery decreased to 65% because of one negatively affecting factor. For the

Dulang+Decane mixture, the recovery is not higher than decane. The reason behind this can be the density of the Dulang+Decane mixture or the significant snap-off that happened which increased the percentage of trapped and unswept oil.

Table 4.16: Factors affecting enhanced oil recovery

Condition	Salinity (ppm)	Low salinity	High salinity	WW	OW	Positive spreading	Negative spreading	Overall recovery (%)
	7216	+		+			-	72 %
Decane water wet	18040		-	+		+		65 %
	36080		-	+		+		58 %
	7216	+			-		-	66 %
Decane oil-wet	18040		-		-	+		60 %
	36080		-		-	+		60 %
	7216	+		+		+		65%
Dulang+Decane water wet	18040		-	+		+		63%
	36080		-	+		+		59%
	7216	+			-	+		64%
Dulang+Decane oil wet	18040		-		-	+		61%
	36080		-		-	+		58%

It has been observed that in this work, salinity and wettability have acted as major factors and spreading coefficient as a minor factor. In sections 4.5.5.1 and 4.5.5.2, the effect of wettability and spreading coefficient has been discussed during three-phase fluid flow as well as final recovery.

4.5.5.1 Effect of wettability

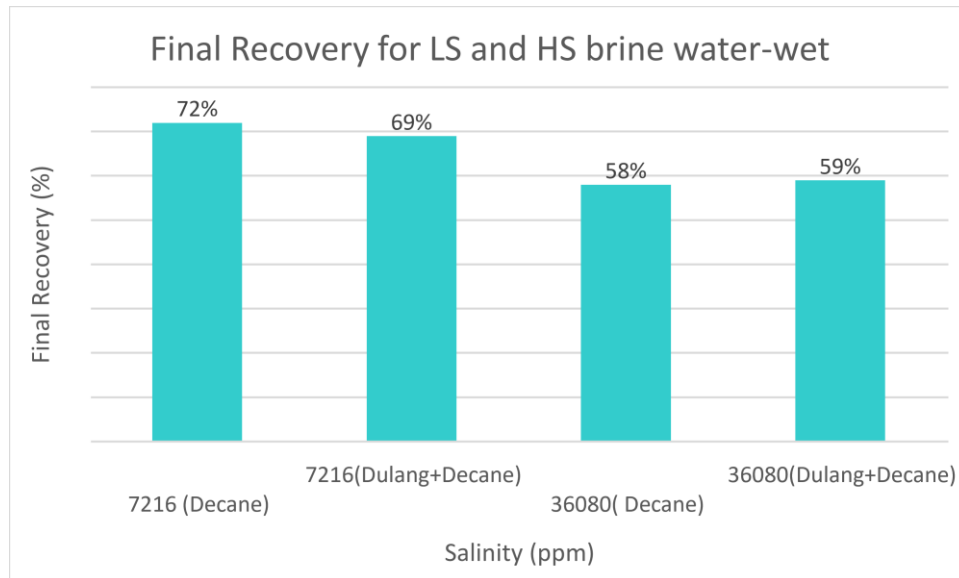


Figure 4.25: Final recovery for high salinity and low salinity water during water-wet condition (@500psi)

In this section, Figure 4.25 is representing the variation in final recovery with respect to different oil (Decane, Dulang+Decane), and salinity brine (LS and HS) under water-wet wetting conditions. In Figure 4.25 under water-wet conditions, the recovery for decane oil and 7216 ppm salinity is 72% whereas Dulang+Decane oil, 7216 ppm salinity has given 69% recovery. Furthermore, for Decane oil, 36080 ppm salinity the recovery is 58%, and 59% recovery has been observed during Dulang+Decane and 36080 ppm. From this figure, it can be seen that under water-wet conditions for low salinity water the recovery is quite higher than in high salinity water. The effect of wettability is significant for low salinity water. Moreover, Figure 4.25 is representing the final recovery concerning different oil (Decane, Dulang+Decane), and salinity brine (LS and HS) under oil-wet conditions.

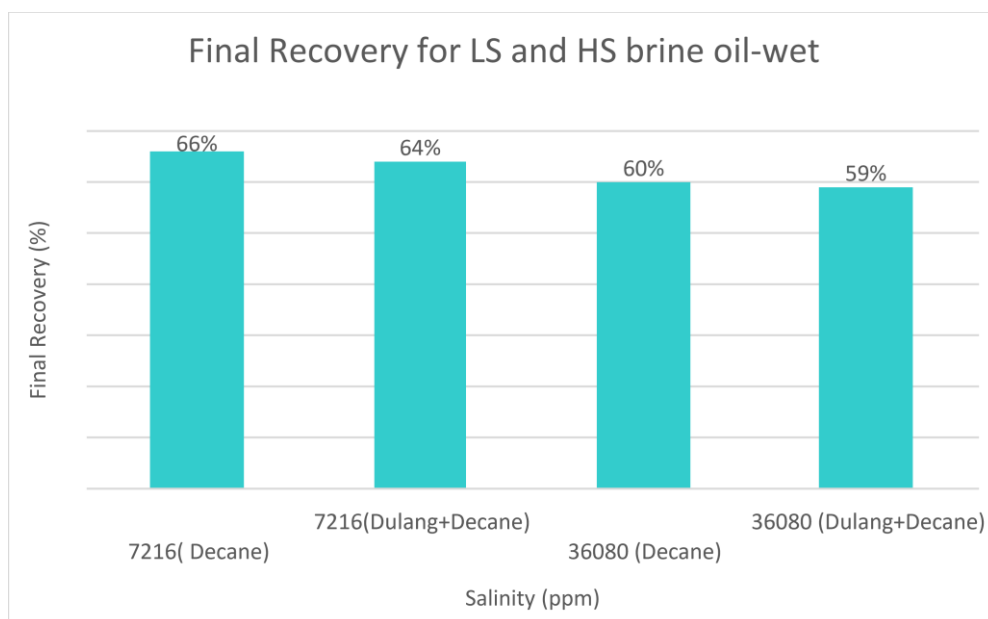
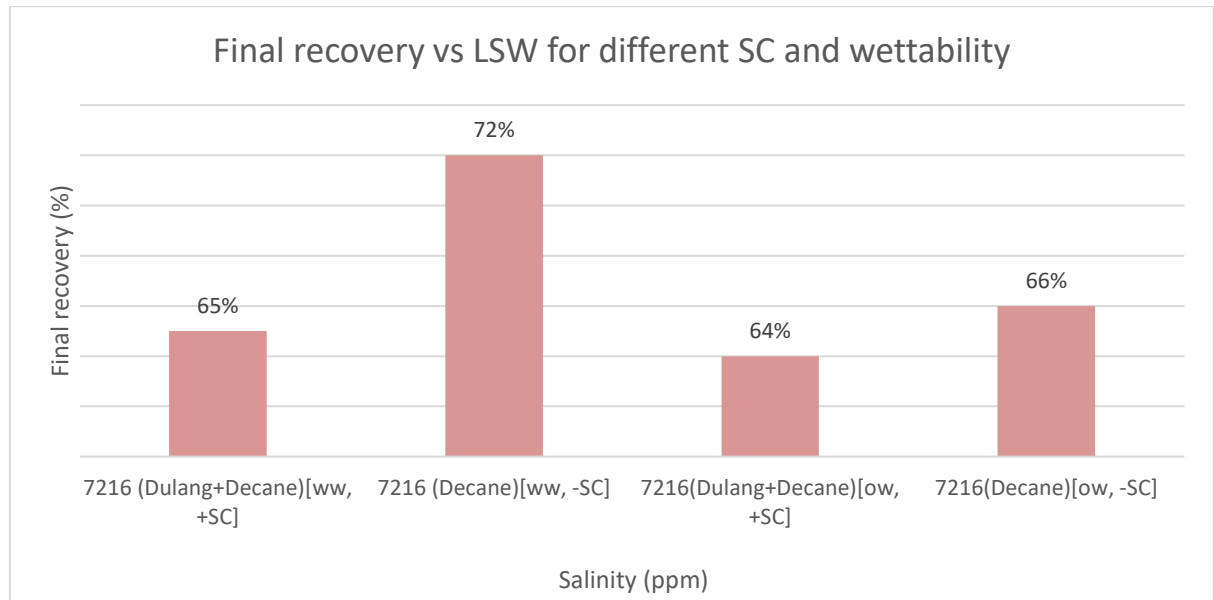


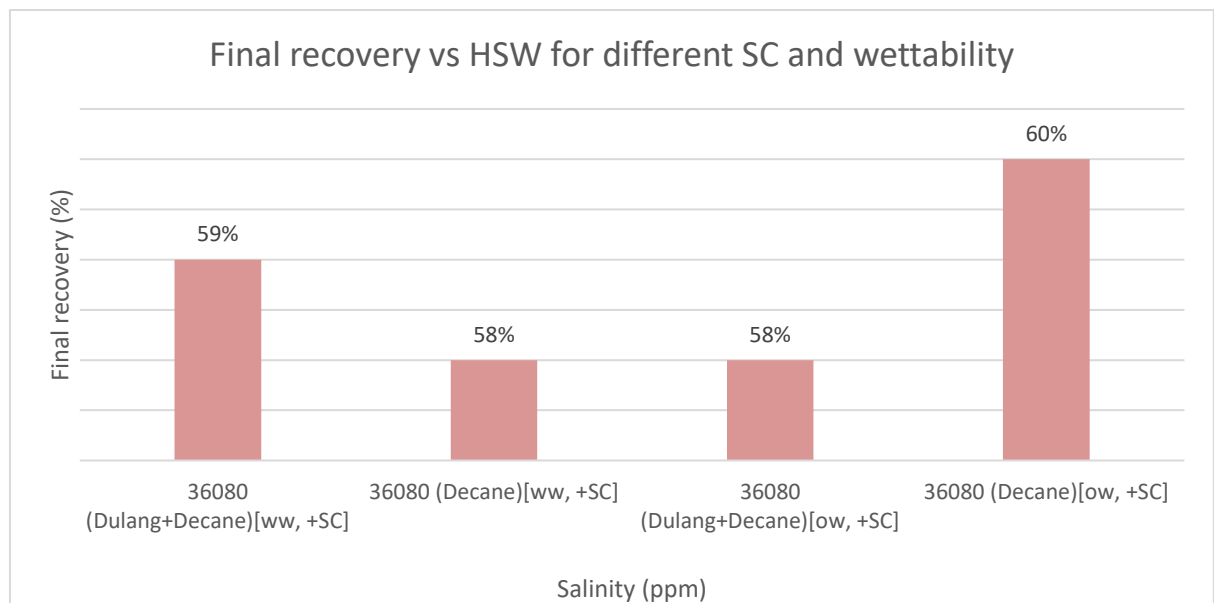
Figure 4.26: Final recovery for high salinity and low salinity water during the oil-wet condition (@500psi)

In Figure 4.26, the recovery for decane, 7216 ppm salinity is 66% and Dulang+Decane, 7216 ppm salinity has given 64% recovery. For high salinity water, decane and Dulang+Decane both oils have given respectively 60% and 59% final recovery. From the closer inspection between 4.25 and 4.26, the recovery has been decreased significantly when the wettability has been changed from water-wet to oil-wet. Under the oil-wet condition, for both low salinity water and high salinity water the recovery has been decreased more than water-wet condition. The decrease in recovery is respectively 8%, 5%, 2%, and no change. It can be observed that the effect of wettability is mostly significant for low salinity water according to the current observation and it is clear that the recovery is directly or indirectly dependent on wettability.

4.5.5.2 Effect of Spreading Coefficient



(a)



(b)

Figure 4.27: Final recovery vs brine salinity for different SC and wettability at 500 psi a) for Low salinity water, b) for High salinity water

The spreading coefficient affects the three-phase fluid flow system, and this effect varies according to the samples and operating conditions. Figure 4.27 is representing final recovery vs brine salinity for different spreading coefficients (SC) and wettability at 500psi. In Figure 4.27 (a) final recovery vs low salinity water for different spreading coefficients and wettability has been presented. For 7216ppm salinity, the spreading coefficient is positive for Dulang+Decane oil under water-wet conditions and the final recovery is 65%. Under the same condition, Decane has given a negative spreading coefficient and the recovery is 72% which is higher than Dulang+Decane oil. Though due to a positive spreading coefficient Dulang+Decane would have given more recovery, it is not happening here. It may happen due to Decane and Decane+Dulang density as decane is lighter than the Decane+Dulang mixture and it is easy for brine and CO₂ gas to move lighter oil.

For oil-wet conditions, both oils have given a positive spreading coefficient under 500psi pressure. The recovery is 64% and 66% for both Dulang+Decane mixture and decane oil. This recovery is quite low compared to water-wet conditions. Though the spreading coefficient value is positive but due to oil-wet conditions the overall recovery is not increasing significantly. It has been observed from this figure that the effect of the spreading coefficient is not playing a major role in this study. A positive spreading coefficient cannot increase the recovery significantly.

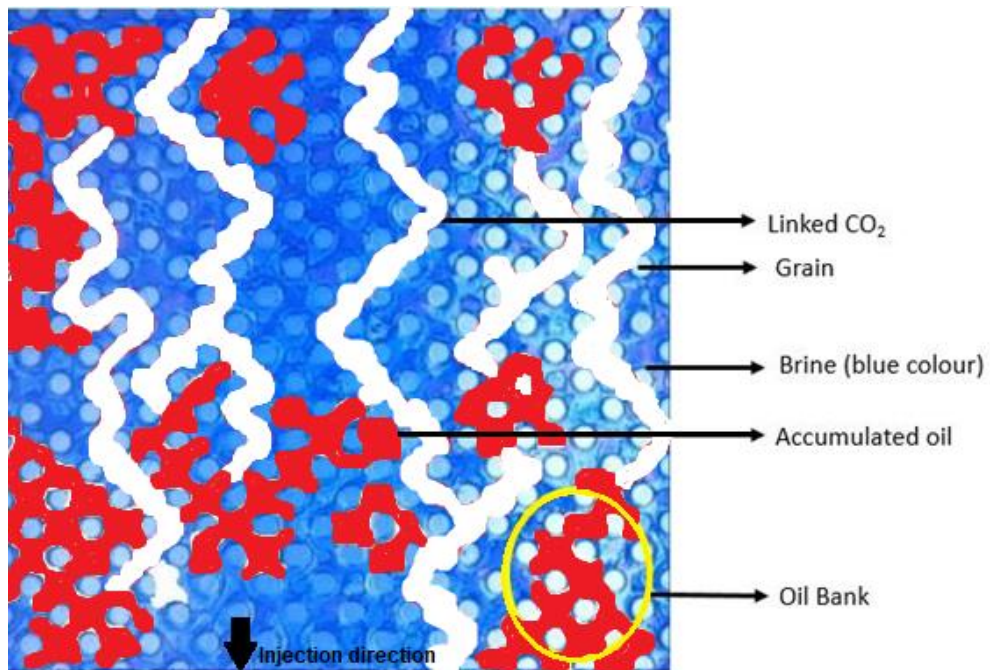
In Figure 4.27 (b) final recovery vs high salinity water for different spreading coefficients and wettability has been presented. In the water-wet condition, Dulang+Decane mixture and Decane oil have given a positive spreading coefficient and the recovery is 59% and 58% whereas in the oil-wet condition the recovery is 58% and 60% for Dulang+Decane mixture and decane oil. Due to the positive spreading coefficient, all the recovery values are near to each other. The recovery values are not fluctuating significantly. Though the recovery has been decreased with increased salinity and the effect of the spreading coefficient is not prominent as the effect of salinity and wettability in this study.

As for all the condition, the spreading coefficient values are mostly positive but when the salinity and wettability are changing the recovery also changes. The effect of the spreading coefficient is very low according to the operating condition and samples of this work.

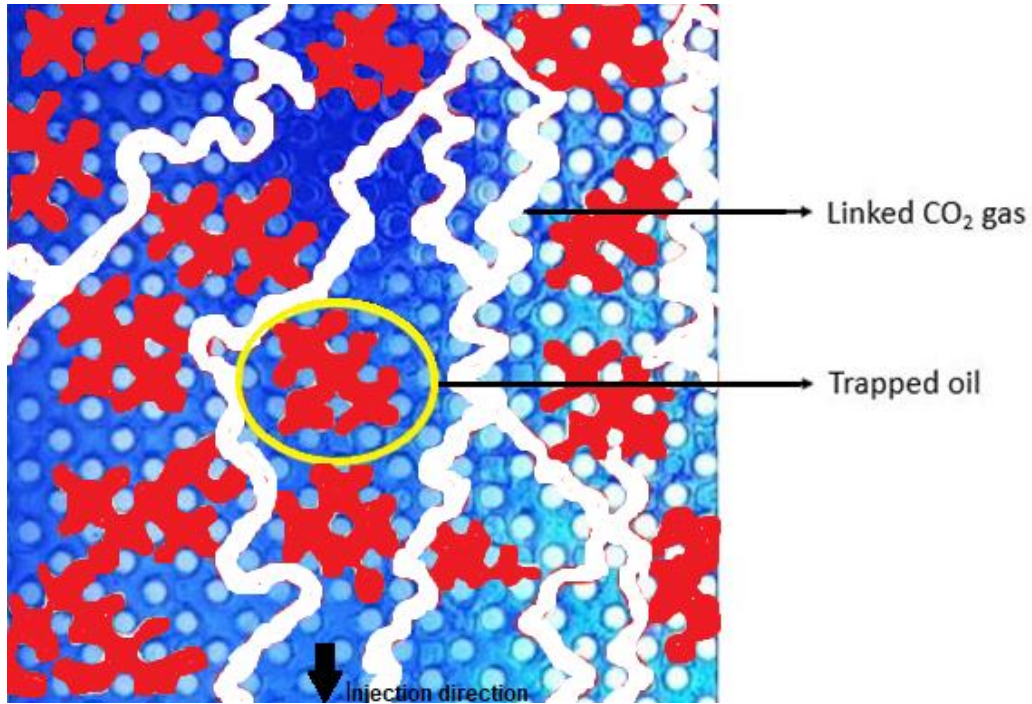
4.6 Fluid Mobilization and Distribution in Pore-scale

In this section, fluid mobilization and distribution for low salinity water and high salinity water under water-wet and oil-wet conditions have been discussed with image analysis. CO₂ gas distribution, formation of oil bank, linked CO₂ gas, trapped oil has been discussed and the cause of oil bank formation and trapped oil has been highlighted with immense importance.

4.6.1 Fluid Mobility and Distribution Analysis for water-wet condition



(a)



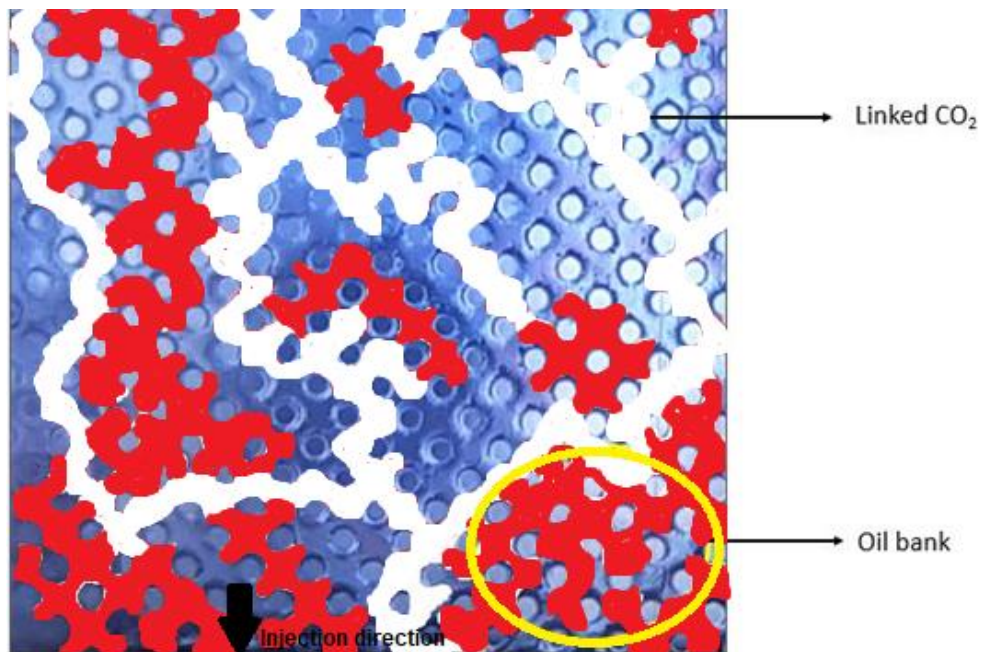
(b)

Figure 4.28: Representation of fluid mobilization and distribution for low salinity and high salinity water under water-wet conditions a) Oil bank formation during low salinity water flooding b) Trapped and unswept oil during high salinity water flooding

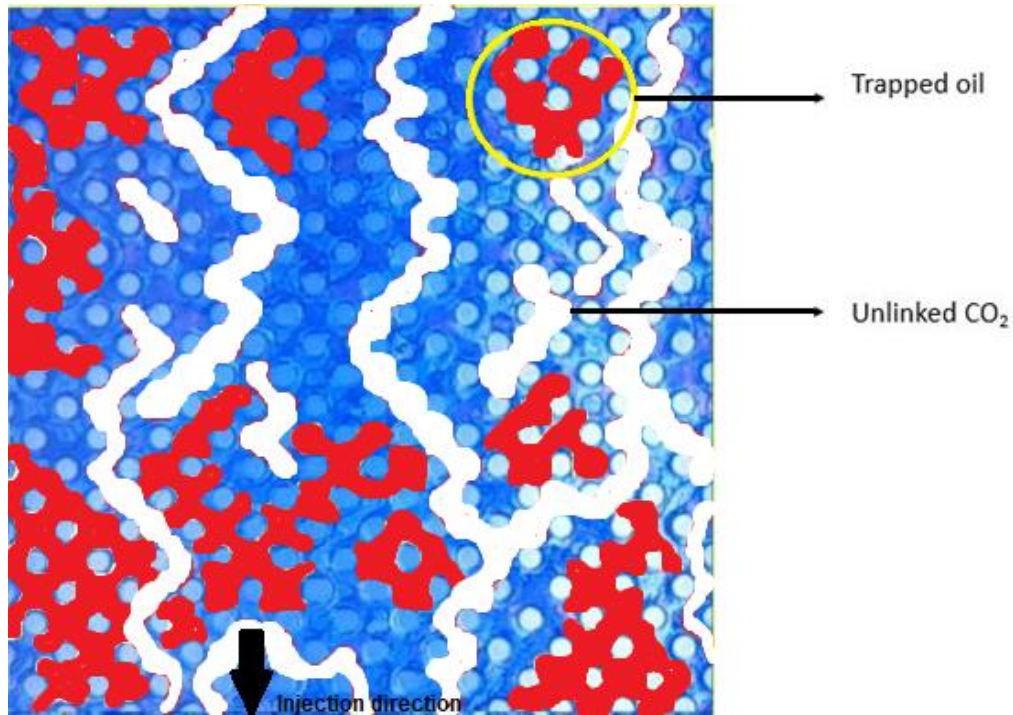
Figure 4.28 is representing fluid distribution and mobilization for decane oil and Dulang+Decane oil where oil bank formation and trapped oil have been detected and the factors affecting this oil bank formation are also discussed widely under water-wet conditions. In Figure 4.28 (a) white lines are representing the distribution of CO₂ gas and the link between gas pockets, blue-colored fluids are 7216ppm low salinity brine, red-colored fluids are oil, and the yellow circled portion is for oil bank. In this Figure, we can see that CO₂ gas has a link between gas lines and it has flushed the oil phase which has formed an oil bank. This oil bank is an indication of enhanced oil recovery. It has been stated in several literature reviews that when a fluid has a positive spreading coefficient and water-wet conditions then a thin film of fluid becomes a continuous phase through the substrate surface. In the case of a water-oil-gas system, in the presence of gas, the oil phase can spread on the water and form an oil bank.

In Figure 4.28 (b), the red lines are representing linked CO₂ gas and the yellow circle is for trapped oil. Here, we can see that CO₂ gas is passing through the oil, and it is not making any prominent oil bank and a group of trapped oil has been detected. These trapped oils could not form any thin oil film which can form an oil bank to increase the oil recovery. Positive and negative spreading conditions are playing a minor role during the formation of an oil bank whereas salinity and the water-wet condition is playing a vital role to form an oil bank. For low salinity water, in water-wet conditions active oil bank has formed prominently whereas for high salinity water there is no active oil bank. Several trapped oils are detected during high salinity water conditions. Due to these situations, we get lower recovery for high salinity water for decane and Decane+Dulang oil. Furthermore, the same situation has been observed for both decane and Dulang+Decane oil.

4.6.2 Fluid Mobility and Distribution analysis for Oil-wet condition



(a)



(b)

Figure 4.29: Representation of fluid mobilization and distribution for low salinity and high salinity water under oil-wet conditions a) Oil bank formation during low salinity water flooding b) Trapped and unswept oil during high salinity water flooding

In Figure 4.29 (a) white lines are for CO₂ gas and the yellow circled part is representing the oil bank. From this Figure, a prominent oil bank has formed during low salinity water flooding and under positive spreading coefficient, oil-wet condition. CO₂ gas has mobilized oil, which has formed a link between oil phases. A prominent group of oil banks has been detected in this Figure which is indicating an increase in oil recovery. According to Oren et al. and Khorshidian et al., positive spreading coefficient and water-wet condition help to form an oil bank where in this work it has been found that under positive or negative spreading coefficient and oil-wet condition, due to the low salinity of water a group of active oil bank has been formed and detected (Khorshidian et al., 2016; Oren and Pinczewski, 1994). Moreover, a noticeable fact has been found from the observation and visualization that the amount of active oil bank is less than in water-wet conditions which is the reason behind less oil recovery than in water-wet conditions.

In Figure 4.29 (b), CO₂ gas lines are not interconnected as in other Figures, also trapped CO₂ has been detected here with trapped oil. There is some linked CO₂ and unlinked CO₂ gas has detected and no active oil bank is there due to the absence of an active oil bank the recovery percentage was lower for this condition. High salinity water cannot mobilize more oil and interconnect them to form an oil bank which would increase the recovery. It may happen due to the density of the Decane+Dulang mixture or the salinity of brine. In this salinity, the CO₂ effect is less, and recovery is not as high as in low salinity brine conditions.

In this work, it has been observed from micromodel experiments that during active oil bank formation the impact of the spreading coefficient was not noticeable compared to other factors such as salinity and wettability. The scenario during water-wet and oil-wet conditions for each oil was the same but the water-wet condition facilitates more active oil bank formation than the oil-wet condition. Due to this higher amount of oil bank during the water-wet condition, more oil recovery has been observed than oil-wet condition according to recovery calculation in section 4.5.

4.6.3 Active Displacement Mechanism During Three-Phase Flooding

Figure 4.30 and 4.31 is the representation of displacement of fluid during low salinity water and CO₂WAG flooding using timelapse. During these experiments, it has been observed that when CO₂ gas was injected, most of the time CO₂ gas phase displaced the oil phase rather than the water phase. In Figure 4.39, it has been noticed that this oil phase has surrounded the gas phase and direct contact between the water phase and gas phase has not been observed significantly. Whereas a contact between the oil and gas phase has been observed during all the experiments. According to Keller et al. and Oren et al., this type of displacement happens with the assistance of double drainage and the double imbibition process (Keller et al., 1997; Oren and Pinczewski, 1994). During low salinity water with a positive spreading coefficient, water-wet and oil-wet conditions it has been observed that oil has been displaced with CO₂ gas significantly and formed an oil bank. Whereas low salinity water has bypassed during LSW injection without displacing a significant amount of oil phase. When low salinity water was surrounded by oil and CO₂ gas, water has been displaced through crevices. Eventually, sufficient pressure during gas injection has displaced oil, which subsequently facilitates contact

between the gas and oil phase. Moreover, Oil layers are observed when the oil phase meets CO₂ gas. On the other hand, during high salinity water, this scenario has been changed and the oil bank was not visible significantly due to the bypassed water phase and gas phase. The gas phase was surrounded by the oil phase which increased the amount of trapped oil. Furthermore, the presence of oil layers between gas and water indicates the effect of the double drainage and imbibition process.

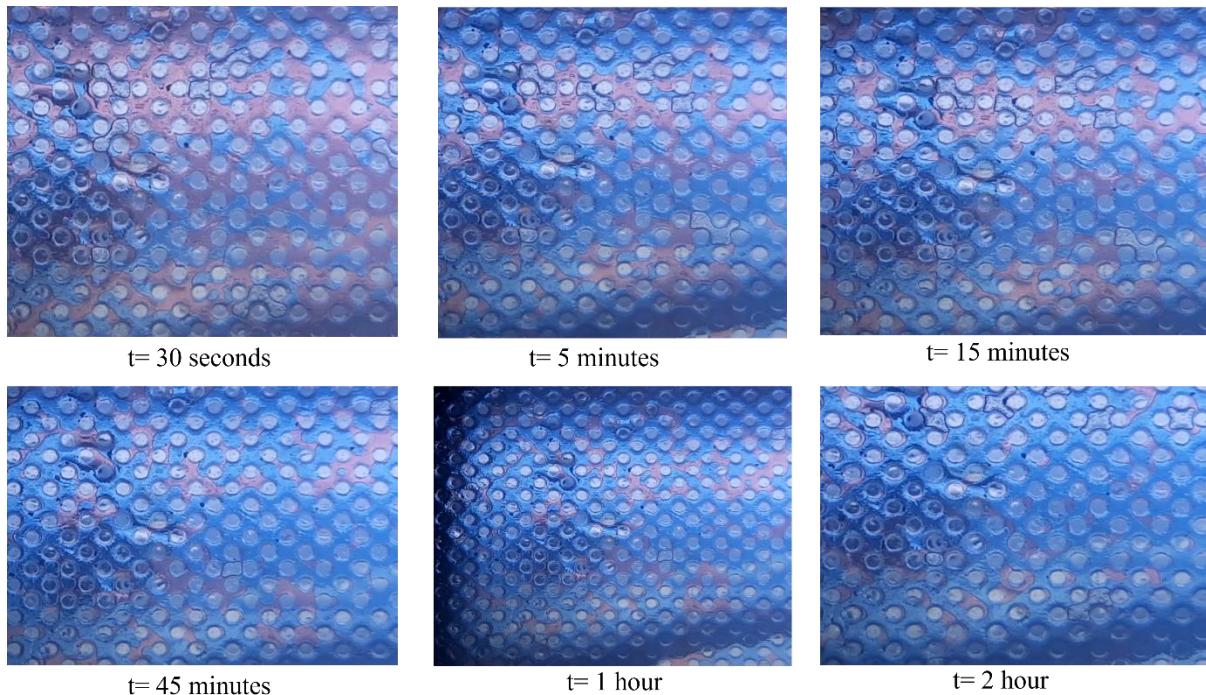


Figure 4.30: Representation of displacement of fluid during low salinity water flooding using timelapse

According to Figure 4.30, fluid displacement after low salinity water flooding has been observed. From a timelapse representation, it can be described that, after 30 seconds, when low salinity water starts displacing the oil phase a significant amount of oil was present in the micromodel and low salinity water gradually displaced the Decane+Dulang oil phase. After 5 minutes of continuous LSWF, the amount of oil phase has been decreased in the micromodel but some of the connected oil banks were observed in the micromodel. After 45 minutes, most of the connected oil was already disconnected but not flushed totally. After 1 hour of continuous low salinity water flooding, a significant amount of oil has been left in the micromodel and the interaction between the oil and water phase was noticeable. After 2 hours,

the oil amount in the micromodel decreased but to mobilize the maximum amount of oil a continuous CO₂ gas has been injected in the next step.

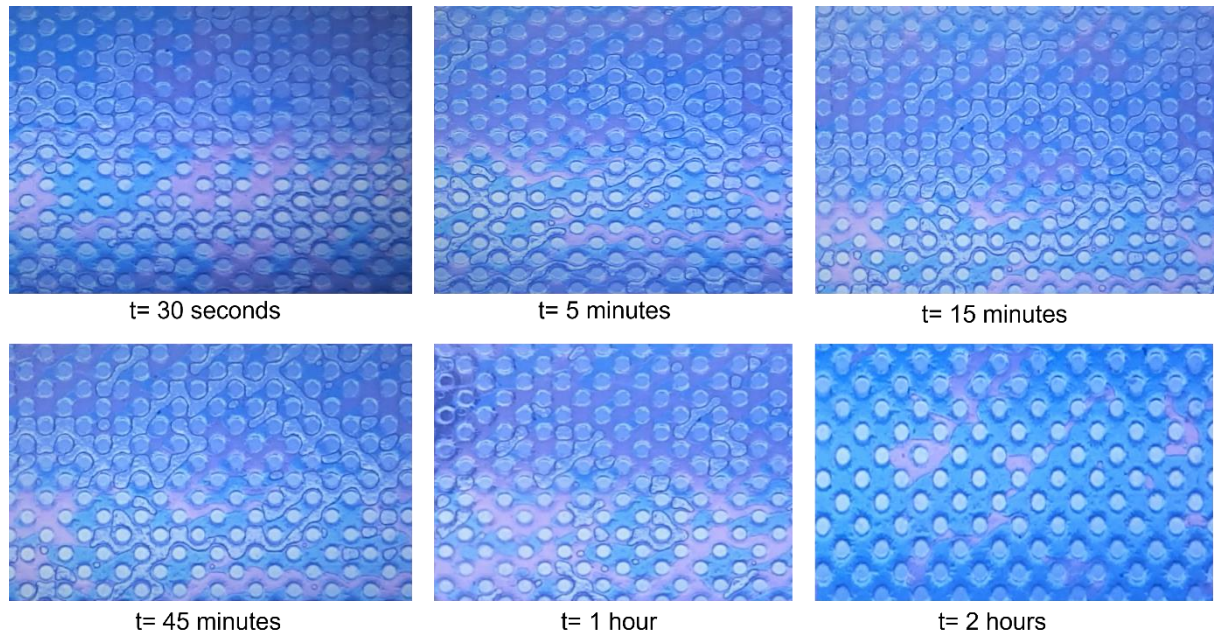


Figure 4.31: Representation of displacement of fluid during CO₂WAG flooding using timelapse

After Flushing with CO₂ WAG, according to Figure 4.31, a direct interaction between the oil phase and gas phase has been observed and the oil phase was displaced more than the water phase by the gas phase. After 30seconds of flushing with CO₂ gas, connected gas strains mostly displaced the oil phase and tried to mobilize those oil banks. After 5 minutes this scenario was more common and significant for the entire micromodel. After 15 minutes, a significant amount of oil has already been flushed by the gas phase. After 45 minutes, in some space, an observation of gas snap-off and trapped oil left by snaped-off gas has been noticed. After 1 hour of flooding, in some spaces oil phase surrounded some of the gas bubbles and created individual trapped gas surrounding the oil phase. Whereas after 2 hours of gas flooding the amount of trapped gas has been gradually decreased and left those oil phases in the micromodel.

4.7 Summary

In this chapter, the effect of CO₂ on interfacial tension, spreading coefficient, and contact angle have been discussed. These experimental results clearly show enough evidence that during LSWACO₂ pressure and CO₂ gas have played an important role in wettability alteration and spreading coefficient. An extensive investigation has been employed using micromodel to validate the effect of spreading coefficient and wettability on LSWAG flooding. It has been observed that low salinity water and water-wet wetting condition contribute a significant effect on the recovery mostly whereas the spreading coefficient played a minor role.

CHAPTER 5

CONCLUSIONS AND RECOMMENDATION

5.1 Conclusion

In this work, the effect of spreading coefficient and wettability has been observed and discussed during low salinity water alternating CO₂ gas flooding. Seven different types of brine salinity, three different types of oil, and CO₂ gas has been used in this experimental work. Two different conditions have been considered to observe the effect of CO₂ in the IFT and contact angle measurements. In addition, micromodel experiments with water-wet and oil-wet conditions have been performed to evaluate the effect of spreading coefficient and better wetting properties during low salinity water alternating CO₂ gas.

From the IFT measurements, it has been observed that IFT values have been decreased with increasing pressure, and the effect of CO₂ on IFT values was visible. Low salinity water has given lower IFT values, and this value has been used to calculate the spreading coefficient. The positive and negative spreading coefficient was found for Decane but for Dulang, only a positive spreading coefficient was found in the presence and absence of CO₂. Decane and Dulang mixture also provide positive and negative spreading coefficients. After all these analyses it is observed that when CO₂ is present in the system, it is giving a more positive spreading coefficient value than without the CO₂ condition. when the system gives a positive spreading coefficient then it leads to an improvement in the oil recovery, and it has been observed in this study.

During contact angle calculation, it has been observed that the water wet condition is giving comparatively better wettability alteration than the oil-wet condition though for some oil the wettability alteration is almost the same for both conditions. Whereas wettability alteration towards water wet is considered as a positive shifting of wettability and in this work water-wet condition also shows the wettability shifting. Moreover, the presence of CO₂ has the influence to shift the wettability towards water wet.

From pore-scale investigation, more recovery was obtained for low salinity water. According to the observation and calculation, during micromodel flooding spreading coefficient worked as a minor factor whereas wettability and salinity played the major factor according to 4.5.5.1 and 4.5.5.2. A prominent amount of oil bank has been detected during low salinity water flooding which excludes the effect of spreading coefficient and wettability. On the other hand, during high salinity water flooding trapped oil and CO₂ gas has been detected. This oil bank has been considered a major factor behind enhanced oil recovery than trapped oil conditions.

5.2 Recommendations

With respect to the result analysis and extensive literature review, some recommendations are listed to make this study more viable in terms of field applications.

- Instead of the Berea core chip, the measurement of contact angle using carbonate and sandstone rock will provide a better insight into wettability alteration.
- Wettability and spreading coefficient are also some important aspects that need due consideration in future studies and measurements using clay will provide a better idea about low salinity water alternating gas flooding.
- This study has been carried out at a temperature of 96°C and pressure ranging from 200 - 2000 psi. Higher temperature and pressure ranges need to be considered to investigate applications in various reservoir conditions.
- Effects of low salinity water under water-wet and oil-wet conditions need to be investigated using carbonate and sandstone rock using different oil and salinity water.
- To use the micromodel results in pore network modelling or simulation.

LIST OF PUBLICATIONS

1. **Rahman, Musfika**, And Iskandar Dzulkarnain. "RSM for Modelling the CO₂ Effect in the Interfacial Tension Between Brine and Waxy Dulang Crude Oil During LSW-WAG EOR." *Journal Of Advanced Research in Fluid Mechanics and Thermal Sciences* 85.2 (2021): 159-174.

REFERENCES

- Abd Shukor, A. Bin, 2014. CERTIFICATION OF APPROVAL.
- Afzali, S., Rezaei, N., Zendehboudi, S., 2018. A comprehensive review on enhanced oil recovery by water alternating gas (WAG) injection. *Fuel* 227, 218–246.
- Al-Abri, H., Pourafshary, P., Mosavat, N., Al Hadhrami, H., 2019. A study of the performance of the LSWA CO₂ EOR technique on improvement of oil recovery in sandstones. *Petroleum* 5, 58–66. <https://doi.org/10.1016/j.petlm.2018.07.003>
- Al-Aulaqi, T., Grattoni, C., Fisher, Q., Musina, Z., Al-Hinai, S., 2011. Effect of temperature, oil asphaltene content, and water salinity on wettability alteration, in: SPE/DGS Saudi Arabia Section Technical Symposium and Exhibition. Society of Petroleum Engineers.
- Alagorni, A.H., Yaacob, Z. Bin, Nour, A.H., 2015. An overview of oil production stages: enhanced oil recovery techniques and nitrogen injection. *Int. J. Environ. Sci. Dev.* 6, 693.
- AlQuraishi, A.A., Amao, A.M., Al-Zahrani, N.I., AlQarni, M.T., AlShamrani, S.A., 2019. Low salinity water and CO₂ miscible flooding in Berea and Bentheimer sandstones. *J. King Saud Univ. - Eng. Sci.* 31, 286–295. <https://doi.org/10.1016/j.jksues.2017.04.001>
- Amirian, T., Haghighi, M., Mostaghimi, P., 2017. Pore scale visualization of low salinity water flooding as an enhanced oil recovery method. *Energy & Fuels* 31, 13133–13143.
- Anbari, A., Chien, H.-T., Datta, S.S., Deng, W., Weitz, D.A., Fan, J., 2018. Microfluidic Model Porous Media: Fabrication and Applications. *Small* 14, 1703575. <https://doi.org/https://doi.org/10.1002/sml.201703575>
- Araujo, Y C, Araujo, M., Guzman, H., Moya, G., 2001. Effect of the spreading coefficient on two-phase relative permeability, in: SPE International Symposium on Oilfield Chemistry. Society of Petroleum Engineers.
- Araujo, Y. C., Araujo, M., Guzmán, H., Moya, G., 2001. Effect of the Spreading Coefficient on Two-Phase Relative Permeability. *Proc. - SPE Int. Symp. Oilf. Chem.* 669–676. <https://doi.org/10.2523/65385-ms>
- Austad, T., RezaeiDoust, A., Puntervold, T., 2010. Chemical mechanism of low salinity water flooding in sandstone reservoirs, in: SPE Improved Oil Recovery Symposium. Society of Petroleum Engineers.
- Barnaji, M.J., Pourafshary, P., Rasaie, M.R., 2016. Visual investigation of the effects of clay minerals on enhancement of oil recovery by low salinity water flooding. *Fuel* 184, 826–835. <https://doi.org/10.1016/j.fuel.2016.07.076>
- Bazazi, P., Sanati-Nezhad, A., Hejazi, S.H., 2019. Wetting phase disintegration and detachment: Three-dimensional confocal imaging of two-phase distributions. *Phys. Rev. Appl.* 11, 14042.

- Bear, J., 2013. Dynamics of fluids in porous media. Courier Corporation.
- Blunt, M.J., 2017. Multiphase flow in permeable media: A pore-scale perspective. Cambridge University Press.
- Cao, S.C., Jung, J., Radonjic, M., 2019. Application of microfluidic pore models for flow, transport, and reaction in geological porous media: from a single test bed to multifunction real-time analysis tool. *Microsyst. Technol.* 25, 4035–4052.
- Chang, L.-C., Chen, H.-H., Shan, H.-Y., Tsai, J.-P., 2009a. Effect of connectivity and wettability on the relative permeability of NAPLs. *Environ. Geol.* 56, 1437–1447.
- Chang, L.-C., Tsai, J.-P., Shan, H.-Y., Chen, H.-H., 2009b. Experimental study on imbibition displacement mechanisms of two-phase fluid using micro model. *Environ. Earth Sci.* 59, 901–911.
- Chapman, E.M., Yang, J., Crawshaw, J.P., Boek, E.S., 2013. Pore Scale Models for Imbibition of CO₂ Analogue Fluids in Etched Micro-model|| junctions Using Micro-fluidic Experiments and Direct Flow Calculations. *Energy Procedia* 37, 3680–3686.
- Chen, D., Pyrak-Nolte, L.J., Griffin, J., Giordano, N.J., 2007. Measurement of interfacial area per volume for drainage and imbibition. *Water Resour. Res.* 43.
- Chen, J.-D., Wilkinson, D., 1985. Pore-scale viscous fingering in porous media. *Phys. Rev. Lett.* 55, 1892.
- Chen, S., Li, H., Yang, D., Tontiwachwuthikul, P., 2010. Optimal parametric design for water-alternating-gas (WAG) process in a CO₂-miscible flooding reservoir. *J. Can. Pet. Technol.* 49, 75–82.
- Cheng, J.-T., Giordano, N., 2002. Fluid flow through nanometer-scale channels. *Phys. Rev. E* 65, 31206.
- Cheng, J., Pyrak-Nolte, L.J., Nolte, D.D., Giordano, N.J., 2004. Linking pressure and saturation through interfacial areas in porous media. *Geophys. Res. Lett.* 31.
- Chequer, L., Al-Shuaili, K., Genolet, L., Behr, A., Kowollik, P., Zeinijahromi, A., Bedrikovetsky, P., 2019. Optimal slug size for enhanced recovery by low-salinity waterflooding due to fines migration. *J. Pet. Sci. Eng.* 177, 766–785.
- Cheraghian, G., 2015. An experimental study of surfactant polymer for enhanced heavy oil recovery using a glass micromodel by adding nanoclay. *Pet. Sci. Technol.* 33, 1410–1417.
- Chiquet, P., Broseta, D., Thibeau, S., 2007. Wettability alteration of caprock minerals by carbon dioxide. *Geofluids* 7, 112–122.
- Conrad, S.H., Wilson, J.L., Mason, W.R., Peplinski, W.J., 1992. Visualization of residual organic liquid trapped in aquifers. *Water Resour. Res.* 28, 467–478.

- Corapcioglu, M.Y., Yoon, S., Chowdhury, S., 2009. Pore-scale analysis of NAPL blob dissolution and mobilization in porous media. *Transp. porous media* 79, 419–442.
- Corapcioglu, Y.M., Chowdhury, S., Roosevelt, S.E., 1997. Micromodel visualization and quantification of solute transport in porous media. *Water Resour. Res.* 33, 2547–2558.
- Crain, E.R., 2002. Crain's petrophysical handbook. Spectrum 2000 Mindware Limited.
- Crandall, D., Ahmadi, G., Smith, D.H., Bromhal, G., 2010. Direct, dynamic measurement of interfacial area within porous media. National Energy Technology Lab.(NETL), Pittsburgh, PA, and Morgantown, WV
- Dang, C., Nghiem, L., Nguyen, N., Chen, Z., Nguyen, Q., 2016. Evaluation of CO₂ Low Salinity Water-Alternating-Gas for enhanced oil recovery. *J. Nat. Gas Sci. Eng.* 35, 237–258. <https://doi.org/10.1016/j.jngse.2016.08.018>
- Dang, C.T.Q., Nghiem, L.X., Chen, Z.J., Nguyen, Q.P., 2013. Modeling low salinity waterflooding: ion exchange, geochemistry and wettability alteration, in: SPE Annual Technical Conference and Exhibition. Society of Petroleum Engineers.
- Dong, M., Forai, J., Huang, S., Chatzis, I., 2005. Analysis of Immiscible Water-Alternating-Gas (WAG) Injection Using Micromodel Tests. *J. Can. Pet. Technol.* 44. <https://doi.org/10.2118/05-02-01>
- Dong, M., Liu, Q., Li, A., 2007. Micromodel study of the displacement mechanisms of enhanced heavy oil recovery by alkaline flooding, in: Proceedings of the International Symposium of the Society of Core Analysts. Citeseer, pp. 2007–2047.
- Emadi, A., Sohrabi, M., 2013. Visual investigation of oil recovery by low salinity water injection: Formation of water micro-dispersions and wettability alteration. *Proc. - SPE Annu. Tech. Conf. Exhib.* 6, 4168–4182.
- Esene, C., Zendejboudi, S., Aborig, A., Shiri, H., 2019. A modeling strategy to investigate carbonated water injection for EOR and CO₂ sequestration. *Fuel* 252, 710–721.
- Fattahi Mehraban, M., Farzaneh, S.A., Sohrabi, M., Sisson, A., 2020. Novel Insights into the Pore-Scale Mechanism of Low Salinity Water Injection and the Improvements on Oil Recovery. *Energy & Fuels* 34, 12050–12064.
- Fernandez Rivas, D., Kashid, M.N., Agar, D.W., Turek, S., 2008. Slug flow capillary microreactor hydrodynamic study. *African Rev. Phys.* 1.
- Fjelde, I., Asen, S.M., Omekeh, A.V., 2012. Low salinity water flooding experiments and interpretation by simulations, in: SPE Improved Oil Recovery Symposium. Society of Petroleum Engineers.
- Fredriksen, S.B., Rognmo, A.U., Fernø, M.A., 2016. Pore-Scale Mechanisms During Low Salinity Waterflooding: Water Diffusion and Osmosis for Oil Mobilization . <https://doi.org/10.2118/180060-MS>

- Gaol, C.L., Wegner, J., Ganzer, L., 2020. Real structure micromodels based on reservoir rocks for enhanced oil recovery (EOR) applications. *Lab Chip* 20, 2197–2208.
- Gerami, A., Alzahid, Y., Mostaghimi, P., Kashaninejad, N., Kazemifar, F., Amirian, T., Mosavat, N., Warkiani, M.E., Armstrong, R.T., 2019. Microfluidics for porous systems: fabrication, microscopy and applications. *Transp. Porous Media* 130, 277–304.
- Gogoi, S., Gogoi, S.B., 2019. Review on microfluidic studies for EOR application. *J. Pet. Explor. Prod. Technol.* 9, 2263–2277.
- Grattoni, C.A., Almada, M.B.P., Dawe, R.A., 1997. Pore and core-scale displacement mechanisms with spreading and wetting effects during three-phase flow. *SPE Lat. Am. Caribb. Pet. Eng. Conf. Proc.*
- Gutiérrez, B., Juárez, F., Ornelas, L., Zeppieri, S., De Ramos, A.L., 2008. Experimental study of gas–liquid two-phase flow in glass micromodels. *Int. J. Thermophys.* 29, 2126–2135.
- Hematpour, H., Mardi, M., Edalatkhah, S., Arabjamaloei, R., 2011. Experimental study of polymer flooding in low-viscosity oil using one-quarter five-spot glass micromodel. *Pet. Sci. Technol.* 29, 1163–1175.
- Jarrahan, K., Seiedi, O., Sheykhani, M., Sefti, M.V., Ayatollahi, S., 2012. Wettability alteration of carbonate rocks by surfactants: a mechanistic study. *Colloids Surfaces A Physicochem. Eng. Asp.* 410, 1–10.
- Javadpour, F., Fisher, D., 2008. Nanotechnology-based micromodels and new image analysis to study transport in porous media. *J. Can. Pet. Technol.* 47.
- Jiang, H., Nuryaningsih, L., Adidharma, H., 2010. The Effect of Salinity of Injection Brine on Water Alternating Gas Performance in Tertiary Miscible Carbon Dioxide Flooding: Experimental Study. *SPE West. Reg. Meet.* <https://doi.org/10.2118/132369-MS>
- Kalaydjian, F.-M., Moulu, J.C., Vizika, O., Munkerud, P.K., 1997. Three-phase flow in water-wet porous media: gas/oil relative permeabilities for various spreading conditions. *J. Pet. Sci. Eng.* 17, 275–290.
- Karadimitriou, N.K., Hassanizadeh, S.M., 2012. A review of micromodels and their use in two-phase flow studies. *Vadose Zo. J.* 11.
- Karadimitriou, N.K., Hassanizadeh, S.M., Joekar-Niasar, V., Kleingeld, P.J., 2014. Micromodel study of two-phase flow under transient conditions: Quantifying effects of specific interfacial area. *Water Resour. Res.* 50, 8125–8140.
- Karadimitriou, N.K., Joekar-Niasar, V., Hassanizadeh, S.M., Kleingeld, P.J., Pyrak-Nolte, L.J., 2012. A novel deep reactive ion etched (DRIE) glass micro-model for two-phase flow experiments. *Lab Chip* 12, 3413–3418. <https://doi.org/10.1039/C2LC40530J>
- Kawelah, M.R., Alzobaidi, S., Thomas, G., Abdel-Fattah, A.I., Gizzatov, A., n.d. Interaction of Surfactants at Nanoscale With Water-Wet and Oil-Wet Calcite Surfaces at Reservoir

Conditions, in: AAPG ACE 2018.

- Kechut, N.I., Nadeson, G., Ahmad, N., Raja, D.M., 2001. Evaluation of CO₂ gas injection for major oil production fields in malaysia-experimental approach case study: Dulang field, in: SPE Asia Pacific Improved Oil Recovery Conference. Society of Petroleum Engineers.
- Keller, A.A., Blunt, M.J., Roberts, P. V., 1997. Micromodel Observation of the Role of Oil Layers in Three-Phase Flow. *Transp. Porous Media* 26, 277–297. <https://doi.org/10.1023/A:1006589611884>
- Kennedy, C.A., Lennox, W.C., 1997. A pore-scale investigation of mass transport from dissolving DNAPL droplets. *J. Contam. Hydrol.* 24, 221–246.
- Khajepour, H., Mahmoodi, M., Biria, D., Ayatollahi, S., 2014. Investigation of wettability alteration through relative permeability measurement during MEOR process: A micromodel study. *J. Pet. Sci. Eng.* 120, 10–17. <https://doi.org/https://doi.org/10.1016/j.petrol.2014.05.022>
- Khalafi, E., Hashemi, A., Zallaghi, M., Kharrat, R., 2018. An experimental investigation of nanoparticles assisted surfactant flooding for improving oil recovery in a micromodel system. *J Pet Environ. Biotechnol* 9, 1000355.
- Khodaii, A., Mousavi, E.S., Khedmati, M., Iranitalab, A., 2016. Identification of dominant parameters for stripping potential in warm mix asphalt using response surface methodology. *Mater. Struct.* 49, 2425–2437.
- Khorshidian, H., James, L.A., Butt, S.D., 2018. Pore-Level Investigation of the Influence of Wettability and Production Rate on the Recovery of Waterflood Residual Oil with a Gas Assisted Gravity Drainage Process. *Energy and Fuels* 32, 6438–6451. <https://doi.org/10.1021/acs.energyfuels.7b02621>
- Khorshidian, H., James, L.A., Butt, S.D., 2016. The Role of Film Flow and Wettability in Immiscible Gas Assisted Gravity Drainage 1–6.
- Kim, B.J., Meng, E., 2015. Review of polymer MEMS micromachining. *J. Micromechanics Microengineering* 26, 13001.
- Kim, H.N., Nam, S.-W., Swamy, K.M.K., Jin, Y., Chen, X., Kim, Y., Kim, S.-J., Park, S., Yoon, J., 2011. Rhodamine hydrazone derivatives as Hg²⁺ selective fluorescent and colorimetric chemosensors and their applications to bioimaging and microfluidic system. *Analyst* 136, 1339–1343.
- Kulkarni, M.M., Rao, D.N., 2005. Experimental investigation of miscible and immiscible Water-Alternating-Gas (WAG) process performance. *J. Pet. Sci. Eng.* 48, 1–20.
- Lager, A., Webb, K.J., Black, C.J.J., Singleton, M., Sorbie, K.S., 2008. Low salinity oil recovery-an experimental investigation1. *Petrophysics* 49.
- Lai, J., Wang, H., Wang, D., Fang, F., Wang, F., Wu, T., 2014. Ultrasonic extraction of

- antioxidants from Chinese sumac (*Rhus typhina* L.) fruit using response surface methodology and their characterization. *Molecules* 19, 9019–9032.
- Land, C.S., 1968. Calculation of imbibition relative permeability for two-and three-phase flow from rock properties. *Soc. Pet. Eng. J.* 8, 149–156.
- Li, H., Zheng, S., Yang, D., 2013. Enhanced swelling effect and viscosity reduction of solvent (s)/CO₂/heavy-oil systems. *Spe J.* 18, 695–707.
- Li, S., Torsæter, O., 2014. An experimental investigation of EOR mechanisms for nanoparticles fluid in glass micromodel, in: Paper SCA2014-022 Was Prepared for Presentation at the International Symposium of the Society of Core Analysts Held in Avignon, France. pp. 8–11.
- Lichtman, J.W., Conchello, J.-A., 2005. Fluorescence microscopy. *Nat. Methods* 2, 910–919.
- Lifton, V.A., 2016. Microfluidics: an enabling screening technology for enhanced oil recovery (EOR). *Lab Chip* 16, 1777–1796.
- Linstrom, P.J., Mallard, W.G., 2001. The NIST Chemistry WebBook: A chemical data resource on the internet. *J. Chem. Eng. Data* 46, 1059–1063.
- Liu, F., Wang, M., 2020. Review of low salinity waterflooding mechanisms: Wettability alteration and its impact on oil recovery. *Fuel* 267, 117112.
- Liu, Y., Block, E., Squier, J., Oakey, J., 2021. Investigating low salinity waterflooding via glass micromodels with triangular pore-throat architectures. *Fuel* 283, 119264. <https://doi.org/https://doi.org/10.1016/j.fuel.2020.119264>
- Liu, Y., Nolte, D.D., Pyrak-Nolte, L.J., 2011. Hysteresis and interfacial energies in smooth-walled microfluidic channels. *Water Resour. Res.* 47.
- Liu, Z., Li, Y., Luan, H., Gao, W., Guo, Y., Chen, Y., 2019. Pore scale and macroscopic visual displacement of oil-in-water emulsions for enhanced oil recovery. *Chem. Eng. Sci.* 197, 404–414.
- Lu, T.X., Biggar, J.W., Nielsen, D.R., 1994. Water movement in glass bead porous media: 2. Experiments of infiltration and finger flow. *Water Resour. Res.* 30, 3283–3290.
- Lun, Z., Fan, H., Wang, H., Luo, M., Pan, W., Wang, R., 2012. Interfacial tensions between reservoir brine and CO₂ at high pressures for different salinity. *Energy & fuels* 26, 3958–3962.
- Maeda, H., Okatsu, K., 2008. EOR Using thin oil film drainage mechanism in water wet oil reservoir. *SPE Asia Pacific Oil Gas Conf. Exhib. 2008 - "Gas Now Deliv. Expect.* 3, 1271–1286.
- Mahmoodi, M., James, L.A., Johansen, T., 2018a. Automated advanced image processing for micromodel flow experiments; an application using labVIEW. *J. Pet. Sci. Eng.* 167, 829–

- Mahmoodi, M., Mahdavi, S., James, L.A., Johansen, T., 2018b. A quick method to fabricate large glass micromodel networks. *Microsyst. Technol.* 24, 2419–2427. <https://doi.org/10.1007/s00542-018-3828-z>
- Mahzari, P., Sohrabi, M., Cooke, A.J., Carnegie, A., 2018. Direct pore-scale visualization of interactions between different crude oils and low salinity brine. *J. Pet. Sci. Eng.* 166, 73–84. <https://doi.org/10.1016/j.petrol.2018.02.051>
- Mani, V., Mohanty, K.K., 1997. Effect of the spreading coefficient on three-phase flow in porous media. *J. Colloid Interface Sci.* 187, 45–56. <https://doi.org/10.1006/jcis.1996.4700>
- Mejia, L., Zhu, P., Hyman, J.D., Mohanty, K.K., Balhoff, M.T., 2020. Coreflood on a chip: Core-scale micromodels for subsurface applications. *Fuel* 281, 118716.
- Meybodi, H.E., Kharrat, R., Araghi, M.N., 2011. Experimental studying of pore morphology and wettability effects on microscopic and macroscopic displacement efficiency of polymer flooding. *J. Pet. Sci. Eng.* 78, 347–363.
- Mohammadi, M., Mahani, H., 2020. Direct insights into the pore-scale mechanism of low-salinity waterflooding in carbonates using a novel calcite microfluidic chip. *Fuel* 260, 116374.
- Mohammed, B.S., Khed, V.C., Nuruddin, M.F., 2018. Rubbercrete mixture optimization using response surface methodology. *J. Clean. Prod.* 171, 1605–1621.
- Moradpour, N., Pourafshary, P., Zivar, D., 2021. Experimental analysis of hybrid low salinity water alternating gas injection and the underlying mechanisms in carbonates. *J. Pet. Sci. Eng.* 202, 108562. <https://doi.org/https://doi.org/10.1016/j.petrol.2021.108562>
- Morrow, N., Buckley, J., 2011. Improved oil recovery by low-salinity waterflooding. *J. Pet. Technol.* 63, 106–112.
- Mtarfi, N.H., Rais, Z., Taleb, M., Kada, K.M., 2017. Effect of fly ash and grading agent on the properties of mortar using response surface methodology. *J. Build. Eng.* 9, 109–116.
- Nadeson, G., Sayegh, S.G., Girard, M., 2001. Assessment of Dulang Field Immiscible Water-Alternating-Gas (WAG) Injection Through Composite Core Displacement Studies, in: SPE Asia Pacific Improved Oil Recovery Conference. Society of Petroleum Engineers.
- Nijjer, J.S., Hewitt, D.R., Neufeld, J.A., 2019. Stable and unstable miscible displacements in layered porous media. *J. Fluid Mech.* 869, 468–499.
- Oren, P.E., Billotte, J., Pinczewski, W. V., 1992. Mobilization of waterflood residual oil by gas injection for water-wet conditions. *SPE Form. Eval.* 7, 70–78. <https://doi.org/10.2118/20185-PA>
- Oren, P.E., Pinczewski, W. V., 1994. Effect of wettability and spreading on recovery of

- waterflood residual oil by immiscible gasflooding. *SPE Form. Eval.* 9, 149–156. <https://doi.org/10.2118/24881-PA>
- Øren, P.E., Pinczewski, W. V., 1995. Fluid distribution and pore-scale displacement mechanisms in drainage dominated three-phase flow. *Transp. Porous Media* 20, 105–133. <https://doi.org/10.1007/BF00616927>
- Patel, D. V, McGhee, C.N., 2013. Quantitative analysis of in vivo confocal microscopy images: a review. *Surv. Ophthalmol.* 58, 466–475.
- Pu, H., Xie, X., Yin, P., Morrow, N.R., 2010. Low salinity waterflooding and mineral dissolution, in: *SPE Annual Technical Conference and Exhibition*. OnePetro.
- Ramanathan, R., Shehata, A.M., Nasr-El-Din, H.A., 2015. Water Alternating CO₂ Injection Process-Does Modifying the Salinity of Injected Brine Improve Oil Recovery?, in: *OTC Brasil*. OnePetro.
- Sahu, J.N., Acharya, J., Meikap, B.C., 2009. Response surface modeling and optimization of chromium (VI) removal from aqueous solution using Tamarind wood activated carbon in batch process. *J. Hazard. Mater.* 172, 818–825.
- Sandnes, B., Knudsen, H.A., Måløy, K.J., Flekkøy, E.G., 2007. Labyrinth patterns in confined granular-fluid systems. *Phys. Rev. Lett.* 99, 38001.
- Sbragaglia, M., Benzi, R., Biferale, L., Succi, S., Sugiyama, K., Toschi, F., 2007. Generalized lattice Boltzmann method with multirange pseudopotential. *Phys. Rev. E* 75, 26702.
- Schneider, M., Osselin, F., Andrews, B., Rezgui, F., Tabeling, P., 2011. Wettability determination of core samples through visual rock and fluid imaging during fluid injection. *J. Pet. Sci. Eng.* 78, 476–485. <https://doi.org/https://doi.org/10.1016/j.petrol.2011.05.016>
- Shelton, J.T., Khuri, A.I., Cornell, J.A., 1983. Selecting check points for testing lack of fit in response surface models. *Technometrics* 25, 357–365.
- Sheng, J.J., 2014. Critical review of low-salinity waterflooding. *J. Pet. Sci. Eng.* 120, 216–224.
- Siadatifar, S.E., Fatemi, M., Masihi, M., 2021. Pore scale visualization of fluid-fluid and rock-fluid interactions during low-salinity waterflooding in carbonate and sandstone representing micromodels. *J. Pet. Sci. Eng.* 198, 108156. <https://doi.org/https://doi.org/10.1016/j.petrol.2020.108156>
- Silverio, V., de Freitas, S.C., 2018. Microfabrication techniques for microfluidic devices, in: *Complex Fluid-Flows in Microfluidics*. Springer, pp. 25–51.
- Sohrabi, M., Riazi, M., Jamiolahmady, M., Ireland, S., Brown, C., 2009. Mechanisms of oil recovery by carbonated water injection, in: *SCA Annual Meeting*. pp. 1–12.
- Sohrabi, M., Tehrani, D.H., Danesh, A., Henderson, G.D., 2004. Visualization of oil recovery

- by water-alternating-gas injection using high-pressure micromodels. *Spe J.* 9, 290–301.
- Sohrabi, M., Tehrani, D.H., Danesh, A., Henderson, G.D., 2001. Visualisation of Oil Recovery by Water Alternating Gas (WAG) Injection Using High Pressure Micromodels - Oil-Wet & Mixed-Wet Systems. *Proc. - SPE Annu. Tech. Conf. Exhib.* 1429–1435. <https://doi.org/10.2523/71494-ms>
- Subasi, A., Sahin, B., Kaymaz, I., 2016. Multi-objective optimization of a honeycomb heat sink using Response Surface Method. *Int. J. Heat Mass Transf.* 101, 295–302.
- Teklu, T.W., 2015. Experimental and numerical study of carbon dioxide injection enhanced oil recovery in low-permeability reservoirs.
- Teklu, T.W., Alameri, W., Graves, R.M., Kazemi, H., Alsumaiti, A.M., 2014. Low-salinity water-alternating-CO₂ flooding enhanced oil recovery: Theory and experiments. *Soc. Pet. Eng. - 30th Abu Dhabi Int. Pet. Exhib. Conf. ADIPEC 2014 Challenges Oppor. Next 30 Years 2*, 893–916. <https://doi.org/10.2118/171767-ms>
- Teklu, T.W., Alameri, W., Graves, R.M., Kazemi, H., AlSumaiti, A.M., 2016a. Low-salinity water-alternating-CO₂ EOR. *J. Pet. Sci. Eng.* 142, 101–118. <https://doi.org/10.1016/j.petrol.2016.01.031>
- Teklu, T.W., Alameri, W., Graves, R.M., Kazemi, H., AlSumaiti, A.M., 2016b. Low-salinity water-alternating-CO₂ EOR. *J. Pet. Sci. Eng.* 142, 101–118.
- Tsakiroglou, C.D., Avraam, D.G., 2002. Fabrication of a new class of porous media models for visualization studies of multiphase flow processes. *J. Mater. Sci.* 37, 353–363.
- Tsakiroglou, C.D., Avraam, D.G., Payatakes, A.C., 2007. Transient and steady-state relative permeabilities from two-phase flow experiments in planar pore networks. *Adv. Water Resour.* 30, 1981–1992.
- Vizika, O., Rosenberg, E., Kalaydjian, F., 1998. Study of wettability and spreading impact in three-phase gas injection by cryo-scanning electron microscopy. *J. Pet. Sci. Eng.* 20, 189–202. [https://doi.org/10.1016/S0920-4105\(98\)00020-5](https://doi.org/10.1016/S0920-4105(98)00020-5)
- Wilson, A., 2015. CO₂ low-salinity water alternating gas: a promising new approach for EOR. *J. Pet. Technol.* 67, 84–86.
- Wilson, J.L., 1994. Visualization of flow and transport at the pore level, in: *Proceedings of the Symposium on Transport and Reactive Processes in Aquifers*, Dracos TH, Stauffer F., Eds., Balkema, Rotterdam, Netherlands. pp. 19–36.
- Yu, M., Zeinijahromi, A., Bedrikovetsky, P., Genolet, L., Behr, A., Kowollik, P., Hussain, F., 2019. Effects of fines migration on oil displacement by low-salinity water. *J. Pet. Sci. Eng.* 175, 665–680.
- Zarikos, I.M., Hassanizadeh, S.M., van Oosterhout, L.M., van Oordt, W., 2018. Manufacturing a micro-model with integrated fibre optic pressure sensors. *Transp. porous media* 122,

221–234.

Zhang, N., Wei, M., Bai, B., 2018. Comprehensive review of worldwide CO₂ immiscible flooding, in: SPE Improved Oil Recovery Conference. OnePetro.

Zhang, Y., Morrow, N.R., 2006. Comparison of secondary and tertiary recovery with change in injection brine composition for crude-oil/sandstone combinations, in: SPE/DOE Symposium on Improved Oil Recovery. Society of Petroleum Engineers.